Illuminating Electron Microscopy of Photocatalysts

Cavalca, Filippo

Publication date:
2013

Document Version
Publisher's PDF, also known as Version of record

Illuminating Electron Microscopy of Photocatalysts

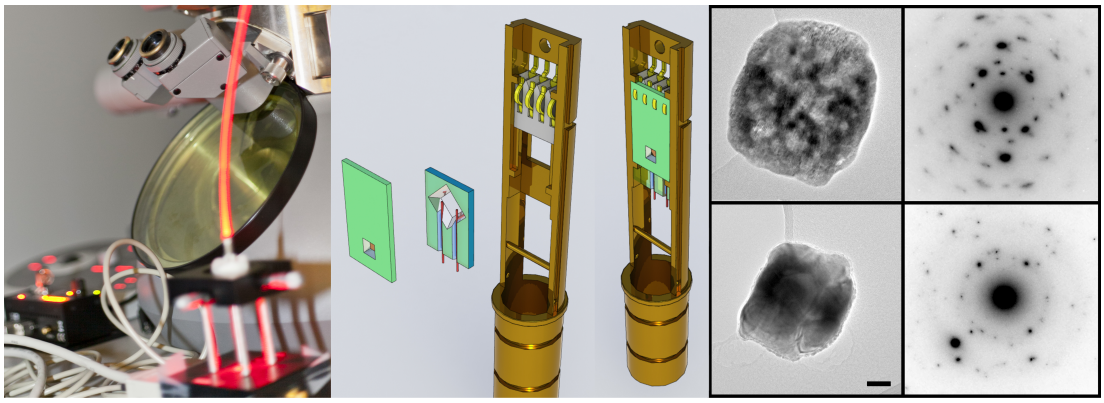

Author: Filippo Cavalca

Center for Electron Nanoscopy

Technical University of Denmark

Supervisors: Thomas W. Hansen, Jakob B. Wagner and Christian D. Damsgaard

A thesis submitted for the degree of

PhilosophiæDoctor (PhD)

January 2013

Abstract

Efficient harvesting of solar energy is the only technology that has the potential to eventually supply the entire population of the Earth with sufficient energy in a sustainable way as a stand-alone, long-term solution. The potential of harvesting is emphasized by the fact that covering 0.1% of the surface of the planet with a device that converts solar energy into a useable form at 10% efficiency would give more than the present worldwide consumption of fossil energy.

Photocatalysts are of fundamental interest for sustainable energy research because they provide a viable route for converting solar energy into chemical bonds. By means of Transmission Electron Microscopy (TEM) it is possible to gain insight in the fundamentals of their reaction mechanisms, chemical behaviour, structure and morphology before, during and after reaction using *in situ* investigations. In particular, the environmental TEM (ETEM) is the instrument of choice employed in this thesis to perform such studies. Typically, photocatalysts work in gaseous or liquid atmosphere upon light illumination. We aim at reproducing their working conditions *in situ*. The ETEM allows exposing specimens to a controlled gas atmosphere, thus implementation of *in situ* sample illumination is needed.

This Ph.D. project is divided in two phases. First, two novel specimen holders capable of shining light onto samples inside the TEM and to probe the sample using visible light spectroscopy techniques were designed and constructed. Secondly, the newly developed holders were used to characterize photocatalytic materials in a simulated working environment.

Prototype design was followed by micromechanical manufacturing, implementation and test of the holders. These were then employed in the analysis of various photoreactive materials and structures with focus on photocatalysts. Novel information on the behaviour of such materials during reaction

was acquired in a reproducible fashion and a new tool for investigation of photoactive materials was made available.
In a wider perspective, the project aims at building a versatile experimental platform inside the microscope that allows electron microscopy under nonconventional TEM conditions and new kinds of *in situ* spectroscopy.

Resumé

Effektiv høst af solenergi er den eneste teknologi, der har potentiale til at forsyne Jordens befolkning med tilstrækkeligt energi på en bæredygtig måde som en selvstændig, langsigtet løsning. Dette potentiale understreges af det faktum, at ved at dække 0,1% af planetens overflade med en anordning, der omdanner solenergi til en anvendelig form med en effektivitet på 10% kan producere mere energi end der i dag produceres fra fossilt brændsel på verdensplan. Fotokatalyse er interessant for bæredygtig energiforskning da den repræsenterer en mulig vej til binde solenergi i kemiske forbindelser. Ved hjælp af *in situ* transmissionelektronmikroskopi (TEM) er det muligt, at opnå en grundlæggende indsigt i katalysatorernes reaktionsmekanismer, kemiske egenskaber, struktur og morfologi før, under og efter reaktion.
I denne afhandling anvendes Environmental TEM (ETEM) til at udføre sådanne undersøgelser. Fotokatalysatorer virker normalt i et miljø bestående af en gas eller en væske under belysning. ETEMet tillader at man udsætter prøver for en kontrolleret gasatmosfære. For at fuldende reaktionsmiljøet skal instrumentet ydermere tilpasses så prøver kan eksponeres for lys *in situ*. Dette ph.d. projekt består af to dele. I den første del, er to nye prøveholdere tilpasset med optik til at belyse en prøve i TEMet, designet og konstrueret. I den anden del er disse holdere anvendt til at karakterisere fotokatalytiske materialer i et simuleret arbejdsmiljø. Ny forståelse af disse materialers opførsel under reaktionsbetingelser er blevet erhvervet på en reproducerbar måde, og en ny teknik til undersøgelse af fotoaktive materialer er blevet udviklet. I et bredere perspektiv, sigter projektet på opbygning af et alsidig eksperimentelt setup i mikroskopet, der tillader elektronmikroskopi under ikke- konventionelle forhold og nye former for *in situ* spektroskopi.

To my parents, who pushed me towards curiosity and knowledge
throughout my entire life.

Acknowledgements

The A. P. Møller and Chastine Mc-Kinney Møller foundation is gratefully acknowledged for the contribution towards the establishment of the Center for Electron Nanoscopy at the Technical University of Denmark.
This work was supported by the "Catalysis for Sustainable Energy" (CASE) research initiative, which is funded by the Danish Ministry of Science, Technology and Innovation. Within this project a strong collaboration among colleagues was developed, aiming at the realization of a working feedback loop among theory, synthesis, test and characterization of new catalysts and photocatalysts for sustainable energy production. In particular, this work would not have been possible without the partnership of Anders Bo Laursen (sample preparation, Sections 4 and 5), Fabio Dionigi (μ-reactor tests, Section 5), Thomas Pedersen and Ole Hansen (MEMS design and fabrication, Section 3.2), and Lars Pedersen (workshop, Section 3.1).
First of all, I would like to thank my supervisors Thomas Hansen, Jakob Wagner and Christian Damsgaard for their priceless support in the past three years. Their supervision has developed into a collaboration and a friendship that made my work stimulating, rich and fruitful. Thanks to Rafal Dunin-Borkowski for giving me the opportunity of starting this project at CEN and to Beata Kardynal for the initial startup support. Thanks to all my colleagues at CEN, it has been brilliant working together in the most familiar and pleasant working environment. I have learned a lot from all of you. Thanks to my fellows Linus, Johan, Robert, Davide and Diego, mates in the pioneering experience of being PhD students at CEN, thanks for all the good times we shared. Thanks to Andy for being the coolest director, for the concerts and chats (not only on Fridays).
I would like to thank Christoph Langhammer for giving an unexpected twist

to my project, for the great experience in Göteborg and a fantastic collaboration.
The most special thanks to Petra for being the unique person you are, these years would not have been the same without you. I feel so lucky I met you.
I really want to thank Anders and Dorte for welcoming me as part of their family, for being so kind and warm, for all your help, all the wonderful chats and times spent together. Special thanks to Pavel, who shared with me countless experiences, years of best friendship, cohabitation, laughter, anger, big nights and lots of other stuff as a brother, you're the man. Huge thanks to Fabio, who I met at the very beginning without either knowing we would become collaborators nor so close friends in music and passions. Thanks to Martin, great friend and partner in crime.
I would also like to thank my family and all my friends in Italy for their support despite the distance. Their love and visits made me extremely happy, I'm so lucky of having you.
Finally I want to thank all my friends in København, you know who you are, I had the time of my life with you in these years.

List of included papers

Appended papers

Paper 1 F. Cavalca et al., In situ transmission electron microscopy of light-induced photocatalytic reactions., Nanotechnology 23, 075705 (2012). [1]

Paper 2 J. B. Wagner, F. Cavalca, C. D. Damsgaard, L. D. L. Duchstein, T. W. Hansen, Exploring the environmental transmission electron microscope., Micron (Oxford, England : 1993) (2012). [2]

Paper 3 F. Cavalca, A. B. Laursen, J. B. Wagner, C. D. Damsgaard, I. Chorkendorff, and T. W. Hansen, Light Induced Reduction of Cuprous Oxide in the Environmental Transmission Electron Microscope, ChemCatChem (2012), submitted

Other published papers

Paper 4 M. He, B. Liu, A. I. Chernov, E. D. Obraztsova, I. Kauppi, H. Jiang, I. Anoshkin, F. Cavalca, T. W. Hansen, J. B. Wagner, et al., Chemistry of Materials 2012, 24, 17961801. [3]

Paper 5 A. Kleiman-Shwarsctein, A. B. Laursen, F. Cavalca, W. Tang, S. Dahl, I. Chorkendorff, Chemical communications (Cambridge, England) 2012, 48, 9679. [4]

Paper 6 A. B. Laursen, Y. Y. Gorbanev, F. Cavalca, P. Malacrida, A. Kleiman-Schwarsctein, S. Kegns, A. Riisager, I. Chorkendorff, S. Dahl, Applied Catalysis A: General 2012, 433-434, 243250. [5]

Contents

List of Figures

LIST OF FIGURES

List of Tables

LIST OF TABLES

1

Introduction

1.1 Project description

This project aims at the characterization of photocatalysts and photoactive materials using novel *in situ* illuminating transmission electron microscopy (TEM). The study of conventional catalysts by means of TEM and spectroscopy is also involved as complementary investigation.
Photocatalysts represent one possible solution to the growing sustainable energy needs. Therefore test, characterization and optimization of working photocatalysts for renewable energy production is of utmost importance. The environmental TEM (ETEM) is the instrument of choice for the characterization of photocatalysts in their working environment—consisting of light and gas. The development of two customized TEM specimen holders to perform *in situ* investigations on photocatalysts in a simulated working environment was a major part of the project.

1.2 Motivation

"The supply of secure, clean, sustainable energy is arguably the most important scientific and technical challenge facing humanity in the 21st century" [6]. This phrase encompasses the fundamental concept of the CAtalysis for Sustainable Energy (CASE) initiative funding this Ph.D project. CASE seeks in catalysis and solar light harvesting viable solutions to the increasing energy demand and decreasing fossil fuel reserves.

1. INTRODUCTION

Sunlight is the primary energy influx on our planet as well as the most exploitable energy source. It powers life on Earth and is naturally converted in various ways through different forms such as wind, waves and chemical bonds.

Particularly in the last decades, humans have been thoroughly exploiting fossil fuels as an inexpensive and accessible energy source. Now the worldwide energy demand is increasing and, at the same time, the supply of fossil fuels is diminishing, leading to the need for renewable energy sources in form of electricity and fuels.

One of the most efficient methods available to produce energy without using fossil fuels is harvesting sunlight and converting it into electricity or storing it in chemical bonds. This can be achieved by directly implementing the energy from the sun in photoelectrochemical processes that lead to the production of fuels, or converting it to electric power using photovoltaic cells and employing the energy produced in electrochemical systems for fuel synthesis. Finally, natural photosynthesis and cellular respiration naturally convert light into biomass that we can turn into usable chemical energy. Efficient harvesting of solar energy is the only technology that has the potential to eventually supply the entire population of the Earth with sufficient energy in a sustainable way as a stand-alone, long-term solution. The potential of harvesting is emphasized by the fact that covering 0.1% of the surface of the planet with a device that converts solar energy into a useable form at 10% efficiency would give more than the present worldwide consumption of fossil energy [7].

The key concept entailed in all these strategies is to convert radiation energy coming from the sun into chemical energy, for example by storing it in durable chemical bonds in form of fuels. This approach ensures energy on demand while boasting a high energy density. Besides, conversion into fuel is a viable solution for efficient energy storage from highly time-variable sources such as wind. The essential ingredient to transform solar energy into chemical energy or convert energy among different chemical forms is catalysis.

Catalysts (see Section 2.1) are necessary to make chemistry cheaper, faster and more secure on the large scale. The CASE initiative constitutes a research framework that aims at the theoretical calculation of novel solid catalysts based on earth-abundant and inexpensive elements, their synthesis, test and characterization. These phases are intertwined in a feedback loop converging to the optimization of newly designed catalysts.

In this thesis the focus is on photocatalysts (see Section 2.1.1). Such catalysts employ

energy in form of light to trigger specific chemical reactions at their surface, for instance fuel synthesis. Demonstrated solar-to-chemical conversion efficiencies of up to 18% in laboratory make photocatalysts interesting for large scale applications, although optimization is needed.
As with conventional catalysts [8], *in situ* studies that probe the materials behaviour in realistic simulated working environments are of utmost importance for materials performance optimization. Photocatalysts could benefit from analogous investigations if the recreation of their working environment can be obtained. This project tackles this necessity with the development of dedicated specimen holders for *in situ* light illumination and their use for characterization of photocatalysts and photocatalytically-relevant phenomena.

1.3 Dissertation overview

This thesis is structured in 6 chapters. First, the theoretical background is outlined in Chapter 2. Here, the basics of catalysis and photocatalysis are explained. This should give the starting point to understand the motivation behind this project. In Section 2.2 and 2.3 the main techniques employed in this work are described. In Chapter 3 the design, implementation and testing of the experimental setup is described. This setup is used in the following chapters. Chapters 4, 5 and 6 present the experimental results. The thesis ends with the conclusion and outlook (Chapter 7). An appendix section (Appendix A) containing supplementary information is added.

2

Theory

2.1 Catalysis

A substance that increases the rate of attainment of chemical equilibrium without itself undergoing chemical change is called a catalyst [9]. Many chemical reactions can take place in the absence of a catalyst but the presence of such a substance causes the reaction to have a higher rate at a given physical conditions. In other words, catalysts lower the activation energy of one or more steps in a chemical reaction, thus being of utmost importance for industrial and large scale applications.
The general scheme for a catalytic reaction is the following:

$$\mathrm{A} + C \longrightarrow \mathrm{A}C \tag{2.1}$$

$$\mathrm{B} + C \longrightarrow \mathrm{B}C \tag{2.2}$$

$$\mathrm{A}C + \mathrm{B}C \longrightarrow \mathrm{AB}C \tag{2.3}$$

$$\mathrm{AB}C \longrightarrow \mathrm{P}C \tag{2.4}$$

$$\mathrm{P}C \longrightarrow C + \mathrm{P} \tag{2.5}$$

$$\mathrm{A} + \mathrm{B} \xrightarrow{C} \mathrm{P} \tag{2.6}$$

Where C represents the catalyst, A and B two generic reactant chemical species and P the reaction product. These reactions are schematically described in Figure 2.1. This shows that the catalyst can be left out of the stoichiometric equation as it is regenerated during reaction. From an industrial standpoint, catalysts are the workhorses of chemical

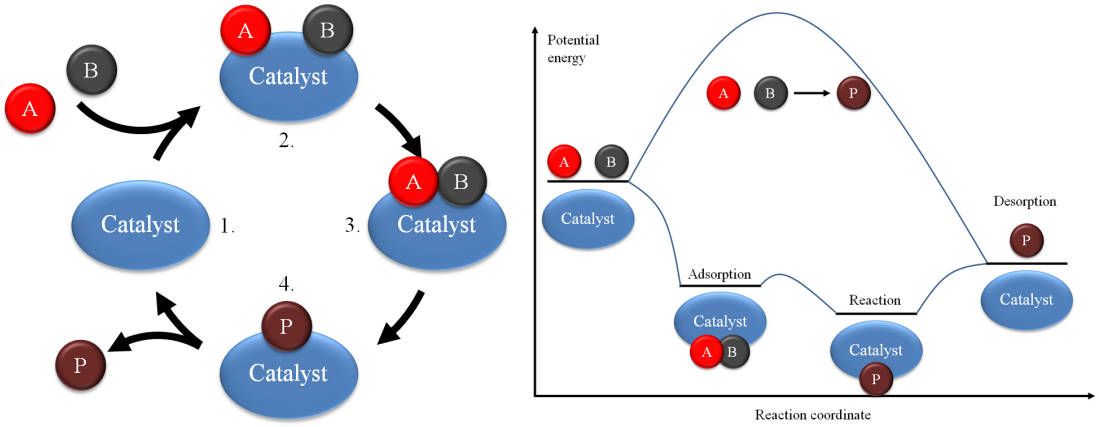

Figure 2.1: Catalysis - The elementary steps describing a catalytic process are schematically represented in the diagram. Chemical species bind to the catalyst (1), react (2-3), and detach (4), leaving the catalyst free for another cycle. The associated potential energy diagram of a heterogeneous catalytic reaction is shown.

transformations that allow approximately 85–90% of the products of chemical industry to be made [10].

Reaction pathways are modified by the addition of a catalyst into more complex but less energy-demanding step sequences. As seen in Figure 2.1, the catalytic reaction starts by bonding the reactants to the catalyst. In the next step, A and B react while they are bound to the catalyst. This critical step has a lower activation energy associated than that of the direct Arrhenius-type reaction. The net effect of a lower activation energy barrier enables more reacting species to collide with sufficient energy for the reaction to occur at specific physical conditions. Although changing the kinetics of a reaction, it is extremely important to note that catalysts do *not* influence reaction thermodynamics. This entails that the extent of a reaction is left unchanged by the addition of a catalyst, *i.e.* both forward and reverse reactions are equally affected and therefore there is no change in reaction equilibrium.

Catalysis is generally divided in two main categories: homogeneous and heterogeneous. The former deals with reactions where reactants and catalyst are in the same phase, in most cases either liquid or gaseous. In the latter the catalyst is present in a different phase than that of reactants and products, typically in the solid state. Heterogeneous catalysis constitutes a field of primary importance in environmental sciences as it is used in the production of the mostly distributed chemicals in the world as well as in the automotive industry and in the major processes for solar fuels generation [10].

For this reason, this thesis will treat uniquely with heterogeneous catalysts and their characterization. Table 2.1 shows some of the most important industrial processes based on heterogeneous catalysis

The chemical nature of heterogeneous catalysts is extremely varied (see Table 2.1),

Reaction	**Catalyst**
Catalytic cracking of crude oil	Zeolites
Hydrotreating of crude oil	Co-Mo, Ni-Mo, Ni-W (sulfidic form)
Reforming of naphta (to gasoline)	Pt, Pt-Re, Pt-Ir
Ethylene epoxidation to ethylene oxide	Ag
Steam reforming of methane ($CO+H_2$)	Ni
Ammonia synthesis	Fe
Sulfuric acid	V(oxide)
Oxidation of CO and hydrocarbons (car exhaust)	Pt, Pd
Reduction of NOx (in exhaust)	Rh, vanadium oxide

Table 2.1: Catalytic processes - Catalysts enable reactions to take place at practically attainable conditions, therefore being largely used in chemical industry [10]. This table shows some of the largest processes based on catalysis.

but some main categories can be outlined. Transition metals such as Ni, Cu, Au, Pt or Ag, are of particular interest. Metal oxides, oxinitrides and functional materials such as zeolites are also commonly used.

Three key attributes for determining the goodness of a catalyst are selectivity, activity and stability. A catalyst can be thought of as a collection of active sites located at a surface. The total number of sites is constant and the adsorption of a reactant is formally a reaction with an empty site to give an intermediate. All sites are equivalent and each can be occupied by a single species only. The rate of any reaction can be described as the product of the rate coefficient k and a term depending on the pressure or concentration of a given reactant

$$r = kf(p_i) \tag{2.7}$$

where p_i is the partial pressure of the reactant i and k is expressed by the Arrhenius equation

$$k = A' \exp\left(\frac{E'}{RT}\right) \tag{2.8}$$

where A' is a temperature-dependent factor and E' is the apparent activation energy for the reaction. E' is not the true activation energy because the catalyst coverage will be temperature-dependent in any condition, which is also the reason why it is not convenient to express activity in terms of activation energy. A rather useful definition of catalytic activity is the *turnover frequency* (TOF). It is defined as the number of times n that the given catalytic reaction takes place at an active site per unit time for a fixed set of reaction conditions (temperature, pressure or concentration, reactant ratio, extent of reaction), i.e.

$$TOF = \frac{1}{S}\frac{dn}{dt} \tag{2.9}$$

where S is the number of active sites.

Selectivity can be described as the conversion of reactants to the desired product divided by the overall conversion of reactants (i.e. the rate of their disappearance). It is defined for each product and can be written as

$$S = \frac{P_x}{\sum P_i} \tag{2.10}$$

where P_x is the concentration of the chosen product x and $\sum P_i$ is the sum of the concentration of all products. A key concept in heterogeneous catalysis is the role of solid surfaces in the reaction environment, therefore investigation of surface interaction between solid and gases is of utmost importance in the understanding of catalysts [11]. Heterogeneous catalytic reactions happen at the catalyst surface upon adsorption, diffusion, reaction and desorption of chemical species. This general mechanism has a number of intermediate steps that is strongly reaction- and catalyst-dependent. Given that reactions happen at the catalyst surface, it is intuitive to understand how a high surface-to-volume ratio catalyst is advantageous in order to obtain a higher activity with a smaller amount of active material. This result is either obtained by using highly porous bulk materials or by structuring the catalyst into particles and supporting them on a substrate. It is clear how the second approach guarantees minimal material consumption. Furthermore, many compounds exhibit enhanced catalytic activity or different selectivity when their particle dimensions decrease below certain thresholds (typically on the order of some tens of nanometers). Emblematic is the case of gold, considered a poorly active catalyst in bulk form but extremely active as soon as particle dimensions get below ∼5nm [12]. The supported-nanoparticle configuration is

the most widely used for industrial and civil purposes (e.g. in automotive catalytic converter) [9].
In most cases, catalysts are subject to extreme temperature and pressure conditions during operation. In these extreme conditions unwanted effects such as catalyst deactivation are not uncommon, e.g. poisoning, coking, sintering or solid-state transformation [13]. Since catalysts can be very expensive, understanding degradation mechanisms and optimizing catalytic systems is of great interest. *In situ* ETEM analysis has proven a unique way to investigate these phenomena 2.3.

2.1.1 Photocatalysis and solar water splitting

Whereas the energy necessary to activate a chemical reaction is lowered by the presence of a catalyst, a photoreaction is similarly enabled or accelerated by the presence of a photocatalyst. As for catalysts, homogeneous and heterogeneous photocatalysts can be distinguished depending on their phase relative to the surrounding reaction environment. Water photolysis (breakdown of water by light) is the mechanism by which water molecules are split into their constituent elements by the action of light. Hydrogen and oxygen production by water splitting using solar energy in the presence of a photocatalyst is a viable route for clean solar fuel production, as seen in Section 1. The photocatalytic solar energy conversion mechanisms are classified according to the photosensitizer type employed. This reaction has been realized over several different catalytic systems, e.g. salts [14], semiconductors [15, 16] and photosynthetic dyes [17]. Hydrogen is likely to play a key role in solving environmental issues such as replacement of fossil fuels. Hydrogen is indispensable in the chemical industry as well, for example in the ammonia synthesis process. As of now, hydrogen is mainly produced by natural gas steam reforming.

$$\mathrm{CH_4 + H_2O \longrightarrow CO + 3\,H_2} \tag{2.11}$$

$$\mathrm{CO + H_2O \longrightarrow CO_2 + H_2} \tag{2.12}$$

In this process, fossil fuels are consumed and CO_2 is released. In order to spare our scarce fossil fuel reserves and cut CO_2 emissions, other ways of producing hydrogen are necessary. Solar hydrogen production can be obtained in several ways

- Electrolysis of water using power generated with e.g. a photovoltaic cell [18, 19].
- Biomass reforming [20].
- Photocatalytic water splitting [21, 22].

The relative simplicity of the latter method is a major advantage over the others for large scale application. Many photocatalysts for water splitting have semiconducting properties. The bandgap —defined as the energy difference between the top of the valence band (VB) and the bottom of the conduction band (CB)— is the primary parameter in the description of a semiconductor. Water splitting for hydrogen production is an uphill reaction, with a positive and large change in Gibbs free energy $\Delta G^\circ = 238$ kJ/mol. The working principle of such materials (shown in Figure 2.2) and the main considerations behind their optimization can be described as follows.
The semiconductor photocatalyst absorbs one photon matching the semiconductor bandgap. Whereas the energy of the incoming photons with respect to the bandgap is relevant for absorption, the position of CB and VB with respect to the redox potentials is an essential parameter too. In order for the photogenerated carriers to cause redox reactions in water, the bottom of the CB must be more negative than the H^+/H_2 redox potential (0V vs SHE) and the top of the VB must be more positive than the H_2O/O_2 redox potential (+1.23V vs SHE). The standard hydrogen electrode (abbreviated SHE), is a redox electrode which forms the basis of the thermodynamic scale of oxidation-reduction potentials [23]. This way electrons can perform the water splitting half reaction

$$2\,H^+ + 2\,e^- \longrightarrow H_2 \tag{2.13}$$

And holes can perform the other half reaction

$$2\,H_2O + 4\,h^+ \longrightarrow 4\,H^+ + O_2 \tag{2.14}$$

This consideration entails that the bandgap must be at least 1.23eV for water splitting to occur. However, electrons and holes must also overcome the kinetic hindrance of charge transfer [24]. In reality, the difference between electron and hole quasi-Fermi levels must be greater than the redox levels by a sufficient amount to account for band bending, overpotential and interfacial recombination. The open circuit potential obtainable with the best photovoltaic device is $\sim$0.6V, which makes the minimum

bandgap for a desired catalyst equal to ∼1.8eV. Furthermore, if the best reported overpotentials required to drive the HER and OER reactions —∼0.1V and ∼0.2V/∼0.4V, respectively— are taken into account we have that the minimum realistic bandgap required is ∼2eV.

If these conditions are fulfilled, electron and hole pairs are generated within the bulk, thereafter migrating until they meet at a recombination center or until they are transferred to e.g. a surface active site. Recombination is of course unwanted as it hinders the amount of carriers performing the desired reaction. Since defective structures offer more recombination sites, a highly crystalline material is desirable [25]. Furthermore, reduction of the particle size to dimensions comparable to the free mean path of photogenerated carriers helps in reducing the distance carriers have to travel to reach the surface, decreasing chances of recombination.

A common technique for further increasing the electron-hole lifetime is the loading of a suitable large-workfunction metal on the semiconductor surface (see Figure 2.2). Since a Schottky barrier is formed at the metal-semiconductor interface [26] electrons fall in the metallic particles and cannot get back, thus effectively reducing the electron-hole wavefunction overlap. These co-catalysts act as carrier traps and provide excellent active sites for redox reactions given their small dimensions. The modification with suitable co-catalysts is often necessary for a photocatalyst to perform.

In some cases, even if a photocatalyst bandgap and band position are suited to those necessary for water splitting, the band gap also straddles the redox potentials for the reduction and oxidation of the material itself. This is the case for CdS, ZnO and other semiconductor photocatalysts. Photocorrosion must be avoided in order to have stable working photocatalysts, hence it is important to understand the mechanisms of such reactions. A study of Cu_2O photocorrosion is presented in Section 4.1.

Eventually, photogenerated carriers generate surface chemical reactions. This step is strongly dependent on the abundance and activity of surface active sites. Electrons and holes must recombine if surface sites for redox reactions do not exist on the surface. As mentioned above, co-catalysts such as Pt, NiO and Rh/Cr_2O_3 are usually loaded on semiconductor photocatalysts to provide active sites for the H_2 evolution reaction. The addition of co-catalysts for the OER is often unnecessary for oxide semiconductors since their valence band is mostly composed by oxygen-2p orbitals, resulting in a highly

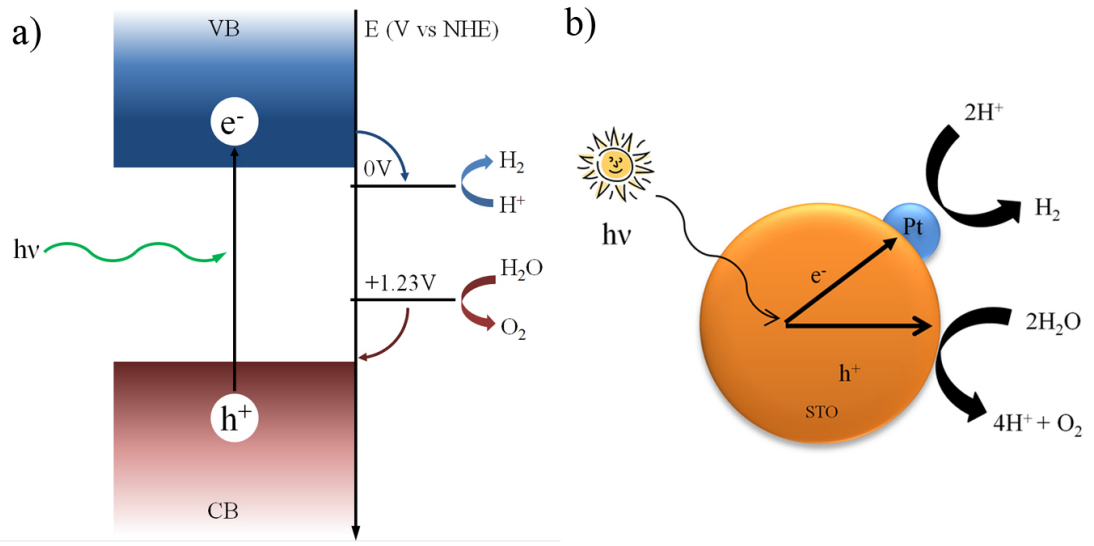

Figure 2.2: Water splitting - a) Principle of water splitting on semiconductor photocatalysts. Electrons are promoted in the conduction band leaving holes behind. These carriers migrate to the surface if they do not undergo recombination and cause redox reactions similarly to electrolysis. The band diagram illustrates how charges generated by a photon of energy greater or equal than the semiconductor bandgap migrate until they reach the surface and react with the surrounding species. b) Photocatalytic water splitting process on a semiconductor photocatalyst ($SrTiO_3$, or STO) loaded with a co-catalyst for hydrogen evolution (Pt).

positive band position (∼3eV [27]). Therefore, photogenerated holes have enough overpotential to run water oxidation on the photocatalyst surface itself.

If the requirements described above are met, water splitting can occur. Using an inexpensive, earth abundant, stable and non-toxic photocatalyst for hydrogen production with a 10 years particle lifetime, a 10% solar-to-hydrogen efficiency production plant producing H_2 at a price of 1.63\$/kg can be achieved [28, 29]. However, separation of a highly flammable stoichiometric mixture of H_2 and O_2 remains a huge risk and an open challenge for the realization of such a plant.

Even considering the numerous challenges in material and plant optimization, photocatalytic hydrogen production remains a viable route for future large scale production. Effort in new photocatalyst discovery, production, testing and characterization is therefore well invested.

2.2 TEM

In this Section the basics of transmission electron microscopy (TEM) are described. The scope of this chapter is to briefly introduce the most important instrument employed in this thesis and some of the principal techniques that have been used during the experiments.

Since "nanotechnology involves imaging, measuring, modeling, and manipulating matter at a length scale between 1 and 100nm" [30], it becomes immediately clear how TEM proves indispensable in solving many problems related to nanoscience. As we will see in Section 2.1, catalysts are often in the form of small particles with diameter sizes of approximately 1-10nm supported on relatively larger support materials consisting typically of high surface area metal oxides with particle size of approximately 20-500nm. If we define the resolution of the TEM by the Rayleigh criterion used in optics, we have that

$$\delta = \frac{0.61\lambda}{\mu \sin \beta} \tag{2.15}$$

where δ is the minimum resolvable distance by the optic system, λ the wavelength of the radiation propagated in the system, μ the refractive index of the viewing medium, and β the semi-angle of collection of the objective lens. If we take a visible light microscope using green light (λ = 550nm), a lens with $\beta \approx$5mrad and operating in air (μ)=1 we have that $\delta \approx$ 300nm. In TEM, λ is typically of the order of few picometers and thus δ can be below 1Å.

2.2.1 Electron optics

In Louis-Victor Pierre Raymond de Broglie's (1892 - 1987) doctoral thesis (1924) the application of the idea of particle-wave dualism (only known for photons up to then) was established for any kind of particle—electrons included. The basic ideas behind this duality are of great importance for physics in general and TEM in particular.

Each particle's momentum p can be related to its wavelength λ via Planck's constant h, as follows

$$\lambda = \frac{h}{p} \tag{2.16}$$

If an electron is accelerated through a potential drop V, it gains a kinetic energy that equals the potential, thus

$$eV = \frac{m_0\nu^2}{2} \tag{2.17}$$

where ν is the electron velocity and m_0 is the electron rest mass. Now if we define the particle's momentum as $p = m_0\nu$ and extract ν from 2.17 we obtain

$$p = m_0\nu = (2m_0eV)^{1/2} \tag{2.18}$$

Which gives finally what defines the electron wavelength as a function of accelerating voltage

$$\lambda = \frac{h}{(2m_0eV)^{1/2}} \tag{2.19}$$

The inverse proportionality between λ and V shows how we can vary the electron wavelength according to our needs, just by changing the accelerating voltage. For typical TEM acceleration voltages we have that electrons travel at speeds comparable to that of light, thus a rigorous treatment would need to include relativistic effects on the electron wavelength at these speeds, yielding

$$\lambda_{rel} = \frac{h}{[2m_0eV(1 + \frac{eV}{2m_0c^2})]^{1/2}} \tag{2.20}$$

We can obtain the typical electron wavelength by substituting the values of most common accelerating values, as shown in table 2.2.

The uniform electron intensity in the incident beam is transformed into a non-uniform

Accelerating voltage (kV)	**Non-relativistic wavelength (nm)**	**Relativistic wavelength (nm)**	**Velocity (x 10^8 m/s)**
120	0.00352	0.00335	1.759
200	0.00273	0.00251	2.086
300	0.00223	0.00197	2.330

Table 2.2: Electron properties - Wavelength and speed as a function of accelerating voltage.

intensity after scattering by the specimen. So a variable electron intensity hits the viewing screen or the electron detector, which translates into contrast on the screen. We can define contrast in terms of the difference in intensity between two adjacent

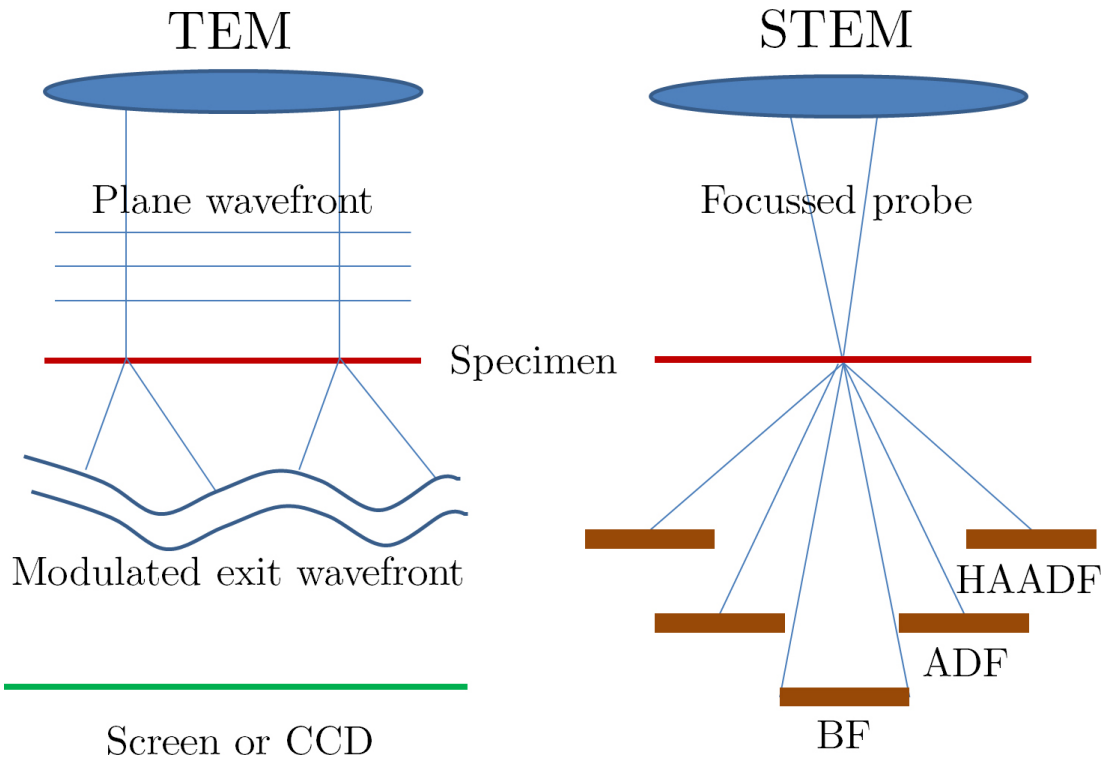

Figure 2.3: TEM and STEM working principle - Schematic illustration of the working principle of TEM and STEM. In TEM, a coherent parallel beam (plane wave) enters the specimen, interacts with it and escapes with a modulated wavefront. The modulation depends on the type of scattering the electrons suffered. In STEM, a focussed electron probe is rastered on the specimen, the scattered intensity is collected on sensors that can be placed at various angles. Different contrast is achieved at different collection angles.

areas. In TEM, different contrast mechanisms can be identified (see Figure 2.3).
Amplitude contrast results from variations in mass or thickness or a combination of the two: the thickness variation can produce contrast because the electron interacts with more material (hence, more mass). Alternatively, diffraction can vary locally because the specimen is not a perfect, uniformly thin sheet.
Mass-thickness contrast arises from incoherent elastic scattering (Rutherford scattering) of electrons. The cross section for Rutherford scatter is a strong function of the atomic number Z (hence the mass or the density, r) and the thickness, t, of the specimen. Rutherford scattering in thin specimens is strongly forward peaked. Therefore, if we form an image with electrons scattered at low angles ($<\sim 5°$), mass-thickness contrast dominates. Z-contrast is the name given to a high-resolution (atomic), mass-thickness (Z), imaging technique.

In a scanning TEM (STEM), Z-contrast is particularly enhanced. The electrons are focussed in the microscope to form a small probe which is rastered across the sample. Typically, annular detectors are used to collect the scattered signal at different angles (see Figure 2.3). A high angle annular dark field (HAADF) is used to collect the signal scattered at angles >50mrad off-axis, which come almost exclusively from incoherent scattering. The intensity of such scattering is proportional to the atomic mass (Z) of the specimen.
Bragg diffraction is controlled by the crystal structure and orientation of the specimen. We can use this diffraction to create contrast in TEM images. Diffraction contrast is simply a special form of amplitude contrast where the scattering occurs at special (Bragg) angles.
Finally, phase contrast arises from interference of more diffracted beams in the specimen. The phase modulation of the electron wave exiting the specimen is translated in intensity contrast, generally in the form of "fringes". This contrast mechanism can be difficult to interpret because it is very sensitive to many factors: the appearance of the image varies with small changes in the thickness, orientation, or scattering factor of the specimen, and variations in the focus or astigmatism of the objective lens. However, its sensitivity is the reason phase contrast can be exploited to image the atomic structure of thin specimens. Of course this also requires a TEM with sufficient resolution to detect contrast variations at atomic dimensions and the proper control of instrument parameters that affect the phases of the electrons passing through the specimen and the lenses.

2.2.2 Electron energy-loss spectroscopy (EELS)

EELS is the analysis of the energy distribution of initially monoenergetic electrons that have come through the specimen. These electrons may have lost no energy or may have suffered inelastic collisions [31, 32].
When electrons are accelerated and sent through a material, they interact with the constituent atoms via electrostatic forces (Coulomb interaction). Such interaction can cause some electrons to be scattered from their original trajectory. Scattering mechanisms can be classified into two broad categories, elastic and inelastic. Elastic scattering occurs when incoming electrons interact with an atomic nucleus via Coulomb attraction. The large electrostatic field of nuclei can cause high angle deflections in the

trajectory of electrons travelling in its vicinity. Such high angle scattering is called Rutherford scattering, and can be so severe that electrons may be deflected more than 90° (backscattering) and escape the specimen from the same surface which they entered (see Figure 2.4a). Inelastic scattering is the result of Coulomb repulsion between the incoming electrons and atomic electrons around each nucleus. This interaction causes the excitation of an atomic electron to a higher energy level (Figure 2.4b). Electrons from an atomic shell can be excited only to unoccupied levels, i.e. above the Fermi level. Inner shell electrons can undergo a transition to a higher unoccupied state upon absorption of an energy amount greater or equal than their original binding energy. Since total energy is conserved during every interaction, the electron will lose an equal amount of energy. Outer shell electrons can also undergo transitions to a higher energy state. If the final state of these electrons is above the vacuum level and the electron has enough energy to reach the surface, it might be emitted as secondary electron.

The beam of transmitted electrons is sent to a spectrometer that separates and analyzes electrons according to their kinetic energy. Electrons go through a magnetic prism where they experience a magnetic field orthogonal to their trajectory. The electron paths are bent as a result of Lorentz force proportional to their kinetic energy and an energy-loss spectrum is thus formed in the dispersion plane, consisting of a distribution of electron intensity versus energy-loss.

EELS spectra can be divided into three main regions. The zero-loss peak, which primarily contains elastic, forward-scattered electrons, but also includes electrons that have suffered small energy losses (below the instrument resolution). The low-loss portion of the spectrum, somewhat arbitrarily defined as the range <50eV, contains electrons which have interacted with the weakly bound, outer-shell electrons of the atoms. Thus, this part of the spectrum reflects the dielectric response of the specimen to high-energy electrons. Finally, the high-loss (or core-loss) portion of the spectrum contains information from inelastic interactions with inner or core shells. These interactions provide direct elemental identification such as bonding energies and atomic position. Quantitative elemental analysis and mapping can be performed using the signal from this region of the EELS spectrum.

When an incoming electron transfers sufficient energy to a core-shell electron causing its transfer to a higher energy state, the atom becomes ionized. The energy-loss signal arising from ionization events is defined an “edge”. The ionization edge shape and

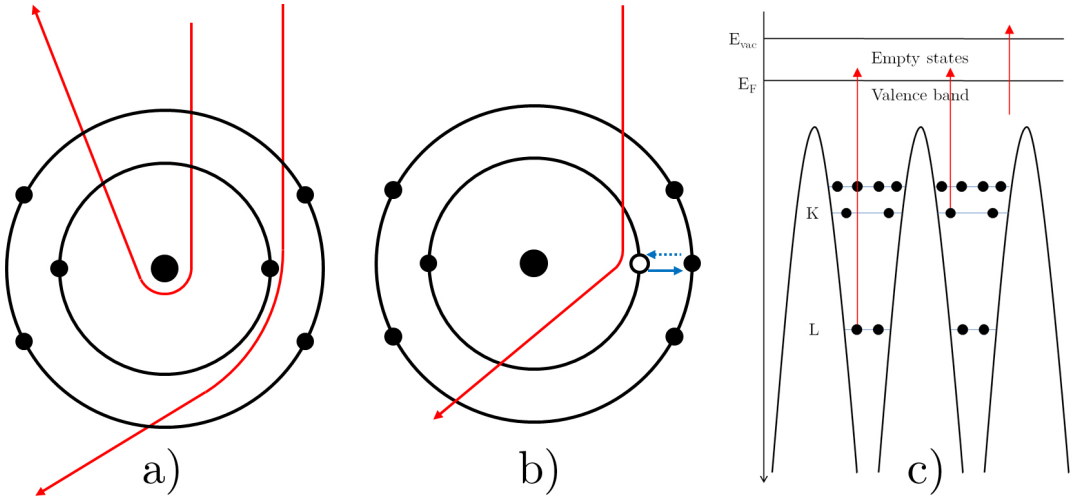

Figure 2.4: Scattering - A classical view of electron scattering by a single atom. a) Elastic scattering is caused by Coulomb attraction by the nucleus. b) Inelastic scattering results from Coulomb repulsion by inner or outer shell atomic electrons, which are excited to higher electronic states. c) Band diagram with some inter-band transitions indicated.

position is dependent on the electronic structure of the atom and it changes depending on whether or not certain energy states are filled or unfilled. For example, in Figure 4.2e the presence of two sharp peaks in the Cu_2O spectrum arise because the ejected L shell electrons do not entirely escape from the atom and have a very high probability of ending up in unfilled d-band states. In contrast, in Cu where the d band is full, the $L_{2,3}$ edge does not show these intense lines. However, the relative energy levels of the ionized shell control the position of the ionization edge in the spectrum. The closer to the nucleus, the deeper the potential well and the more the energy required to eject the electron (see Figure 2.4). In case the excited electron absorbs enough energy to be transferred into empty states above the Fermi level, the edge shows a fine structure modulation, called energy-loss near-edge structure (ELNES) and extended energy-loss fine structure (EXELFS), that can be correlated to the bonding of the ionized atom, its coordination and its density of states. Perhaps the most evident example of ELNES is the appearance of "white lines", as those shown in Figure 4.2e. ELNES in the Ti edge is described in Chapter 5. These sharp peaks arise because in certain elements the core electrons are excited into well-defined empty states, not a broad continuum. The $L_{2,3}$ edges of the transition metals and the $M_{4,5}$ edges of rare earths show such features, as shown by Zaluzec [33].

If the specimen is very thin (i.e. of dimensions comparable to the mean free path of incoming electrons), the probability of scattering is low and the probability of more than one scattering event within the specimen is negligible. For relatively thick specimens, individual peaks may not be visible in the loss spectrum. Multiple outer- and inner-shell processes combine to produce a broad distribution peaked around an energy loss of some hundreds of eV. Moreover, each ionization edge in the energy-loss spectrum is superimposed on a downward-sloping background which arises from other energy-loss processes. Since the background intensity is often comparable to or larger than the core-loss intensity, accurate subtraction of the background is essential. For quantitative elemental analysis, the core-loss intensity of interest must be isolated by subtracting the background intensity, which can be approximated by a power-law energy dependence as AE^{-r}. In thicker samples, a broad double-scattering peak appears at an energy-loss of approximately $E_k + E_p$, where E_k is the energy-loss of a core shell and E_p is the energy of the plasmon peak observed in the low-loss region. This causes the presence of a broad hump beyond the edge, as shown in Figure 4.2e. Within limits, however, such plural scattering can be removed from the spectrum by deconvolution. Several deconvolution techniques are available to deconvolute both low-loss and core-loss signals [34]. Since core-loss spectroscopy is used extensively in this work, the deconvolution techniques for this portion of the spectrum will be treated.

Fourier-ratio deconvolution considers the energy-loss spectrum as divided into two regions: the low loss, containing the zero-loss peak and energy losses up to typically 100eV, is used as a deconvolution function for the second region, which contains the core-loss intensity. Deconvolution is carried out by dividing the Fourier transform of the second region by that of the first. If an ideal core-loss single scattering distribution is defined $K^1(E)$, the probability of a transmitted electron suffering an energy loss between E and $E + dE$ due to core ionization and no other process is $K^1(E)dE/I$, where I is the total intensity entering the spectrometer. The probability of no inelastic scattering of any kind is I_0/I, where I_0 is the zero-loss intensity, so the total probability of a core loss between E and $E + dE$ is $[K^1(E)dE/I]/(I_0/I) = K^1(E)dE/I_0$. The probability that the total energy loss falls in the range E to $E+dE$, of which an amount $E - E'$ is due to inner-shell ionization, is $[K^1(E - E')dE/I_0][P(E')dE/I]$, where $P(E)$ is the ideal plural scattering intensity. The total probability of a mixed scattering,

involving one or more low-loss events in addition to an inner-shell excitation, is

$$\frac{M(E)dE}{I} = \int_{E=0}^{E_{max}} \frac{K^1(E)dE}{I_0} \frac{P(E')dE'}{I} = K^1(E) * P(E) \frac{dE}{II_0} \tag{2.21}$$

where E_{max} is any energy loss exceeding $E - E_k$, E_k being the core-edge threshold energy. The total intensity within the core-loss spectrum is equal to

$$K(E) = K^1(E) + M(E) = K^1(E) * []\delta(E) + P(E)\frac{dE}{I_0} \tag{2.22}$$

where $M(E)$ is the intensity due to mixed scattering. As recorded by a spectrometer with a resolution function $R(E)$, the core-loss intensity will be

$$J_k(E) = K(E) * R(E) = K^1(E) * \{[I_0\delta(E) + P(E)] * \frac{R(E)}{I_0}\} = K^1(E) * \frac{J_l(E)}{I_0} \tag{2.23}$$

where $J_l(E)$ is the measured low-loss spectrum, including the zero-loss peak. Taking Fourier transforms of both sides of Equation 2.23 and rearranging,

$$k^1(\nu) = \frac{I_0 j_k(\nu)}{j_l(\nu)} \tag{2.24}$$

Equation 2.24 shows that, in principle, the measured core-loss intensity $J_k(E)$ can be corrected for both plural scattering and instrumental broadening by multiplying by I_0 and deconvoluting with respect to the measured low-loss intensity $J_l(E)$.

Even though the scattering mechanisms of transmitted electrons are complicated, by making approximations simple formulae for routine quantitative analysis can be obtained. These assumptions are valid within certain limits of specimen thickness. The integrated intensity of single scattering from shell K of a selected element, characterized by a mean free path L_K and a scattering cross section σ_K, would be given by

$$I_K = I(\frac{t}{L_K}) = NI_0\sigma_K \tag{2.25}$$

where I_0 represents the unscattered (zero-loss) intensity and N is the areal density (atoms per unit area) of the element, equal to the product of its concentration and the specimen thickness. If we record the scattering only up to an angle β and integrate its

intensity over a limited energy range Δ, the core-loss integral is

$$I_K(\beta, \Delta) = I(\frac{t}{L_K}) = NI_0\sigma_K(\beta, \Delta) \tag{2.26}$$

where $\sigma_K(\beta, \Delta)$ is a partial cross section for energy losses within a range Δ of the ionization threshold and for scattering angles up to β, obtainable from experiment or calculation.

The effect of elastic scattering is to cause a certain fraction of the electrons to be intercepted by the angle-limiting aperture. To a first approximation, this fraction is the same for electrons that cause inner-shell excitation and those that do not, in which case $I_K(\beta, \Delta)$ and I_0 are reduced by the same factor. Therefore the core-loss integral becomes

$$I_K(\beta, \Delta) \approx I(\frac{t}{L_K}) = NI_0(\beta)\sigma_K(\beta, \Delta) \tag{2.27}$$

where $I_0(\beta)$ is the actual (observed) zero-loss intensity. Equation 2.27 applies to a core-loss edge from which plural (core-loss + plasmon) scattering has been removed by deconvolution.

If we now include valence electron (plasmon) excitation as a contribution to the spectrum, its effect is to redistribute intensity toward higher energy loss, away from the zero-loss peak and away from the ionization threshold. Not all of this scattering falls within the core-loss integration window, but to a first approximation the fraction that is included will be the same as the fraction that falls within an energy window of equal width in the low-loss region. If so, the core-loss integral (including plural scattering) is given by

$$I_K(\beta, \Delta) \approx I(\frac{t}{L_K}) = NI_0(\beta, \Delta)\sigma_K(\beta, \Delta) \tag{2.28}$$

where $I_0(\beta, \Delta)$ is the low-loss intensity integrated up to an energy-loss Δ.

Although Equations 2.27 and 2.28 allow measurement of the absolute areal density N of a given element, an atomic ratio of two elements (a and b) is more commonly required. If plural scattering is removed from the spectrum by deconvolution, Equation 2.28 leads to

$$\frac{N_a}{N_b} = \frac{I_{Ka}(\beta, \Delta_a)\sigma_{Jb}(\beta, \Delta_b)}{I_{Jb}(\beta, \Delta_b)\sigma_{Ka}(\beta, \Delta_a)} \tag{2.29}$$

The shell index can be different for the two edges ($J \neq K$) and a different energy window ($\Delta_a \neq \Delta_b$) can now be used for each edge, larger values being more suitable

at higher energy loss where the spectrum is noisier and the edges representing different elements are spaced further apart.
An energy-loss spectrum contains contributions from various types of inelastic scattering, and it is often necessary to separate these components for subsequent study. Multiple linear least squares (MLLS) methods fit the total spectral intensity $F(E)$ to an expression typically of the form

$$F(E) = AE^{-r} + \sum B_n S_n(E) \tag{2.30}$$

Where AE^{-r} represents a pre-edge background interpolating function of the negative power low type, n is the number of spectra used in the linear combination, S_n represent the core-loss reference spectra for the element of interest and B_n are the weight coefficients for each component. The coefficients can be found by minimizing

$$\sum (J_i - S_i)^2 \tag{2.31}$$

for data channels i covering the entire region. Spectra formed by mixed-phase specimen can be decomposed into their individual components, while the contribution of each component to the final spectrum can be extrapolated.

2.3 *In situ* TEM and ETEM

Often, materials characterization is carried out on samples out of their "natural" environment, in other words, a specimen is prepared by extraction of a portion of material from a real system, preparation for analysis, fixation onto a support and insertion in the designed instrument. This set of interactions unavoidably affects the specimen in a more or less dramatic fashion depending on the sample we are looking at. Often this effect is affordable in the sense that the specimen does not suffer a change that, e.g., destroys its structure or morphology. However, time must always be spent in proving or speculating whether the specimen analysed is representative of the original system and, in such case, why the specimen interaction with the environment does not compromise the investigation. If a system such as a catalyst — routinely subject to chemical reactions in its working conditions — is studied, interruption of the catalyst working cycle is needed in order to produce a sample that serves as a "snapshot" of

the catalyst state at a given time. If several samples are taken at different times from e.g. a catalytic reactor, what has happened during these time intervals can be inferred and the catalyst history could thereby be postulated —if the sample does not change when it is removed from the reactor. Unfortunately, catalysts can be very sensitive to interaction with temperatures, pressures and atmosphere compositions other than those found in the reactor. Therefore, it can be difficult to assess whether the analysed samples are representative of the actual system, especially if the exact catalyst condition in the reactor is the aim of the analysis.

Another approach to studying reacting systems is to investigate them during reaction. This implies either putting a probe in the reactor or reproducing the reaction inside the analyzing instrument. If the structure of a catalyst has to be determined at the atomic scale, TEM can be an ideal instrument of choice [2,8,35–37] because of the high magnification achievable, the variety of specimens it can accommodate and the facile sample preparation. Using an Environmental TEM (ETEM), an instrument capable of exposing samples to a controlled gas environment while performing TEM (see Figure 2.5), it is possible to reproduce simulated working conditions for the catalyst as it is analyzed.

The basic concept behind ETEM technology is to enable conventional TEM operation while the sample is maintained in a controlled atmosphere. A variety of technical implementations are available for producing such a controlled pressure drop and confinement, generally based on two basic approaches: the closed cell [38] and the differential pumping system [8]. Each approach has its own advantages and disadvantages that can be listed as follows.

- **Differential pumping:** Additional pumping channels near the sample area in the microscope column allow the entire pole piece gap volume to be filled with a controlled gas atmosphere (see Figure 2.5) at pressures generally below 3000 Pa. The gas volume is confined by pressure limiting apertures located in the pole piece bore, while extra dedicated pumps are used to evacuate the gas in the column sections immediately adjacent to the high pressure area. This is a modification to the microscope itself, therefore the environmental capacity is confined to the modified instrument, as opposed to the closed cell which can be used in various microscopes. On the other hand, there is no restriction to the holder type used.

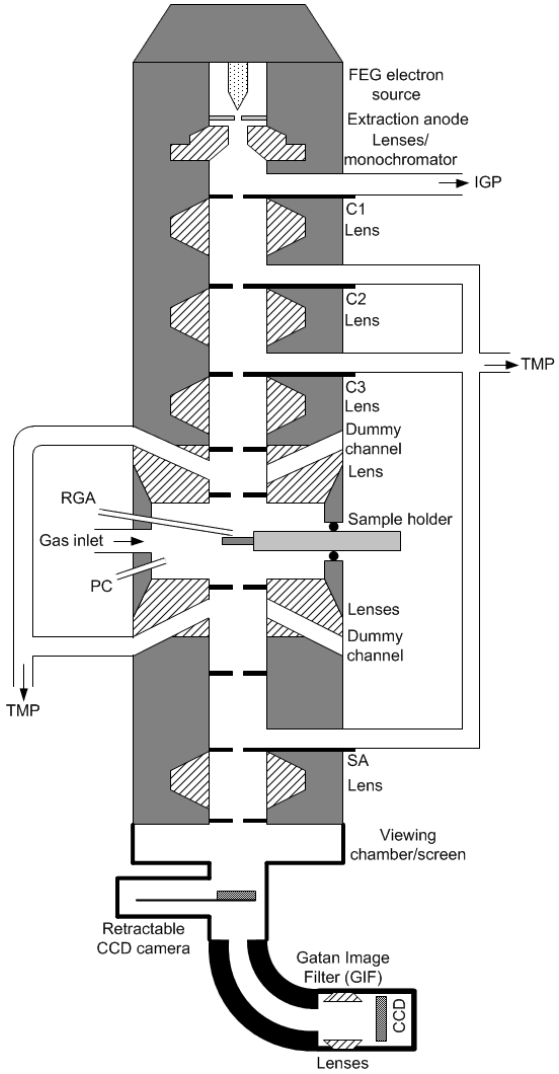

Figure 2.5: Environmental transmission electron microscope (ETEM) - Schematic cross-sectional drawing of an FEI Titan 80-300 equipped with e-cell. The ability of allowing a controlled gas atmosphere is provided by some modifications to the basic intrument. The space around the specimen is provided with extra pumping apertures, a gas inlet and a capillary for residual gas analysis connected to a mass spectrometer.

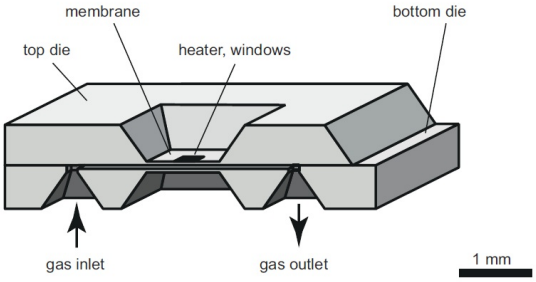

Figure 2.6: Closed environmental cell - Schematic representation of a "wet cell" in the design presented by Creemer et al. [38]. Two silicon chips supporting suspended silicon nitride membranes are placed into contact towards the membrane area. Micro channels are produced in the bottom chip and connected to the sealed area within the two facing membranes.

This allows to exploit the features of commercially available or custom holders in combination with a gas atmosphere.

- **Closed cell approach:** Here the specimen holder is implemented with the gas handling as well as the heating system. The sample is contained and sealed between two microfabricated, electron-transparent membranes that enclose the volume where the gas atmosphere is confined. One of the major advantages of such system is that it allows higher-than-atmospheric pressures around the sample [38–40]. Furthermore, the gas is confined to the sample area, thus is microscope-independent. The pathway through the gas that electrons have to traverse is inherently limited but, on the other hand, electrons interact strongly with the membranes constituting the windows. This interaction degrades both spatial resolution and signal-to-noise ratio of imaging in TEM and STEM mode, EELS and EDX spectroscopy.

Many dedicated specimen holders designed for ETEM as well as conventional TEM application exist commercially, besides a number of custom-built holders from pioneering scientists [39, 41–45]. In the most common scenario, a heating element is used to control the temperature of the sample as it is inserted in the microscope, thereby enabling the opportunity of driving thermally-induced reactions, annealing or phase transformations.

Typically, an *in situ* ETEM experiment is conducted in gas at a pressure of 10^{-3}—10mbar. The sample behaviour is observed and analyzed at different temperatures, studying the effects of chemical reactions taking place. TEM observation, however, entails irradiation of the sample with a beam of accelerated electrons having a kinetic energy depending on the accelerating voltage. Thus besides providing useful information the electron beam can cause temporary or permanent damage to the specimen [46, 47]. Damage can occur via radiolysis or atomic displacement, depending on the electron-matter interaction mechanism. The first mechanism is associated with the degradation of chemical bonds caused by fast moving electrons and by radiation emitted by the sample itself upon interaction with the electron beam. The latter arises from momentum transfer between high energy electrons and atoms in the specimen. Whereas what is described is valid for electron microscopy under vacuum, the presence of gas species near the sample further complicates the situation [2, 35].

High energy electrons can ionize gas molecules upon impact, in the same way they break chemical bonds in radiolytic interactions with the sample, as described above. Ionization of gases generates very reactive radicals that interact with the specimen. Neutral and otherwise unreactive atoms such as noble gases can therefore become powerful chemical agents and modify the observed sample. This adds up to the direct beam effect present even in vacuum described above. It is clear from these considerations how ETEM experiments must be performed very carefully, especially if specimen modifications upon desired chemical reactions are to be followed. Interpretation of results is strongly dependent on beam effect, which should be minimized if possible during the experiment and always be addressed in the analysis.

There are different ways to minimize and quantify beam effects. Momentum transfer can be reduced significantly by decreasing acceleration voltage, thereby minimizing knock-on damage. On the other hand, slower electrons have a larger interaction cross section and have therefore a greater probability of modifying the chemical structure of the sample via radiolysis. Reduction of beam intensity is beneficial in this respect, effectively reducing the energy density impinging on the specimen. Observing sample behaviour under different beam intensity conditions is a good benchmark for assessing beam effects. In general, reactions should be performed *ex situ* prior to any ETEM experiment and their effects verified. If the desired chemical reaction occurs on a sufficiently short time scale with respect to the beam-induced sample modifications, a true

in situ observation is possible.
Therefore, gas pressure and composition as well as electron beam intensity have to be optimized for ETEM experiments. Sometimes, *ad hoc* strategies for observing samples have to be adopted (see Section 4) in order to account for beam effects in the data interpretation. Furthermore, a set of control experiments where the reaction is performed in absence of the electron beam is a good practice for assessing the effect of the beam alone on the specimen.

2.4 Local surface plasmon resonance (LSPR)

In metallic nanoparticles, the outer shell electrons can be considered as free to move, and can be excited by electromagnetic radiation into coherent collective oscillations [48]. This phenomenon is called Localized Surface Plasmon Resonance (LSPR) [49]. If an electromagnetic radiation such as visible light is directed towards a metal structure, the "free" electron cloud of the nanoparticle is displaced by the external radiation's electric field as sketched in Figure 2.7. The displaced cloud generates an electric field on its own, which acts as a restoring force driving the electrons back towards the equilibrium position. If the frequency of the external field matches the natural oscillation frequency of the electrons, a resonance is obtained. The term "localized" is used since these excitations are confined within the volume of the nanoparticle and they are non-propagating.
The resonance frequency depends on the metal, on the size and shape of the nanoparticle, as well as on the dielectric constant of the surrounding medium [50–52]. These facts have led to the use of LSPR for a vast number of applications in several fields, ranging from Raman spectroscopy [53, 54] to biosensing [55] and solar cells [56], etc. When the resonance condition is satisfied, the total electric field around the nanoparticle is enhanced owing to the contribution of the field generated by the oscillating electrons. If an array of plasmonic structures patterned on a transparent substrate is exposed to broadband light, the LSPR-induced field enhancement causes a minimum in the transmitted light efficiency in the resonance condition, corresponding to a maximum in the absorbed and scattered light efficiency. That is, radiation at the frequency matching the plasmonic resonance is highly absorbed and scattered. As a result, one can detect the presence and identify the frequency of a plasmonic resonance either by analyzing

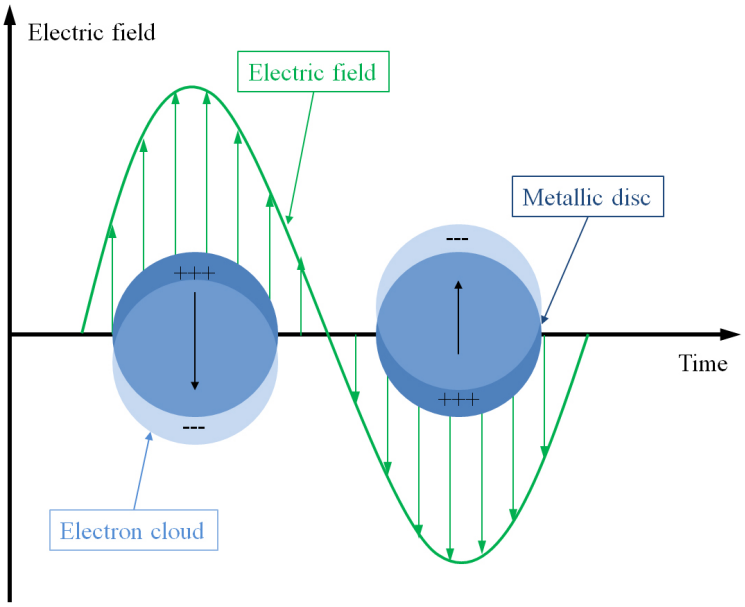

Figure 2.7: LSPR - Schematic of the displacement of free electrons in a metallic nanoparticle caused by the electric field of incoming electromagnetic radiation. A LSPR is thus excited in the nanoparticle.

the scattered light (for example with a dark field microscope), or by measuring the "extinction" of transmitted light. Extinction is defined as the amount of light that is not transmitted as a function of frequency. At the LSPR frequency, plasmonic particles exhibit an optical cross section which is much larger than the physical one [57], which means that the interception area that the spherical particle presents to the incident radiation is much larger than its actual size. This enlargement of the effective cross section of metal NPs caused by LSPRs allows us to consider and use them as optical antennas (or nanoantennas), due to their strong interaction with incoming light.

The shape of the nanoparticle extinction and scattering spectra, and in particular the peak wavelength λ_{max}, depends on nanoparticle composition, size, shape, orientation and local dielectric environment [58]. Given the latter dependence, the LSPR is sensitive to changes in the surrounding chemical environment, which result in changes of the resonance peak position, shape and intensity. Therefore, plasmonic nanoparticles can be used "directly" as nanoplasmonic transducers that convert small changes in the local refractive index into measurable shifts in the extinction and scattering spectra [55].

We can model the refractive index-induced plasmonic shift as

$$\Delta\lambda \approx m(n_{adsorbate} - n_{medium})(1 - \exp(-2d/l_d)) \tag{2.32}$$

where m is the sensitivity factor expressed in nm per refractive index unit (RIU), $n_{adsorbate}$ and n_{medium} are the refractive indices of the adsorbate and medium surrounding the particle, respectively, d is the effective thickness of the adsorbate layer, and l_d is the electromagnetic field decay length [51]. LSPR shifts can be maximized and tuned by varying parameters such as m and l_d during nanosensor fabrication [59]. In the case of direct nanoplasmonic sensing, a sensor is typically composed of an arrangement of plasmonic metallic structures (spheres, particles, discs, or more complicated shapes) arranged in arrays on a support or in a liquid suspension, which is put in contact with the studied system [55, 60]. Any changes in the sensor dielectric environment as well as changes of the sensor particles themselves will result in a change in the extinction spectrum, which can be detected with high sensitivity with an appropriate optical spectrometer [61].

Whereas direct nanoplasmonic sensing applications are dominating in the biomedical area, they present some major drawbacks and limitations in materials science. The first and likely most relevant limitation is that the sensor itself is exposed to the analyzed system. This means that if a thermally activated chemical reaction is under investigation, the sensor itself could undergo irreversible changes or even take part in the reaction, which can be undesirable and can bias the results. Such condition is clearly unaffordable in the field of catalysis, especially if sensors are made of metallic nanoparticles, which can be very catalytically active. However, the working principle of nanoplasmonic sensing remains of utmost interest for the study of catalysis, provided that a system for decoupling the sensors and the studied system is implemented. Such decoupled sensing setup is called Indirect NanoPlasmonic Sensing (INPS), and is realized by placing an array of randomly distributed identical gold nanodisks on a substrate (typically a glass slide) and adding a thin protective dielectric film on top of the structure [61] (see Figure 2.8). The spacer layer has a twofold beneficial effect in that it protects the plasmonic sensor from the surrounding environment and it can be functionalized. The protective function can be achieved by SiN_x layers as thin as 5nm, and makes the INPS platform much more versatile towards the study of reactions that

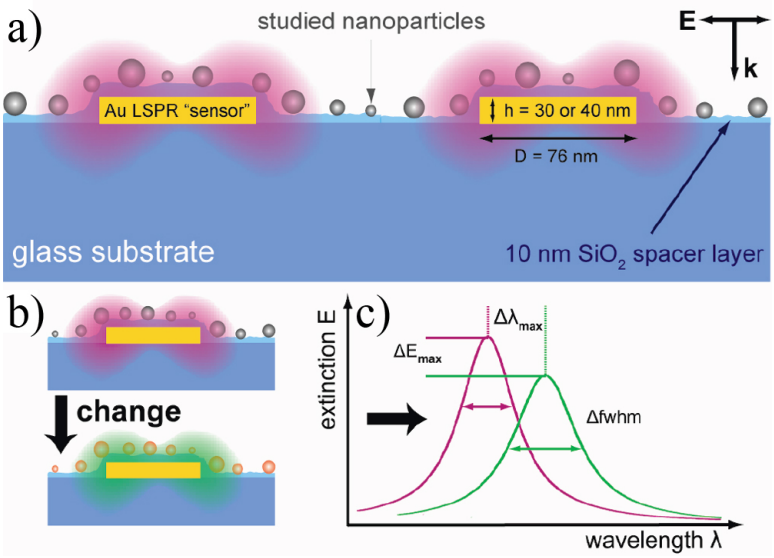

Figure 2.8: INPS - Schematic of the indirect nanoplasmonic sensing principle. a) The architecture of the sensor is shown in cross section. Au nanodisks are embedded in a 10nm thick SiO_2 spacer layer and covered with nanoparticles. b) If these particles undergo chemical change —due to e.g. adsorption of molecules or phase transformation—, the sensor responds (c) exhibiting a shift of the resonance peak. [61]

involve chemicals and processes that could alter the sensor itself (e.g. acids able to dissolve metals). Furthermore, a functionalized spacer layer can be used to provide a desired surface chemistry as a substrate or even as an active participant in the reaction. Owing to the large optical cross section, the volume occupied by the enhanced electromagnetic field extends beyond the spacer layer and the LSPR sensing can be used.

Acquisition of LSPR spectra and their processing can be performed with an array spectrometer and extinction signals can be calculated using a simple procedure. First, a blank substrate without any sensor is placed in the INPS unit and a transmission spectrum is recorded. This spectrum is used as the reference for the extinction calculation. Another spectrum is acquired from the sample in darkness, and recorded as the dark reference. The blank is substituted with an INPS sensor and a sequential timed spectrum acquisition can be set up. For each spectrum, the extinction is calculated as follows

$$E = \frac{(b - v)}{(b - d)} \tag{2.33}$$

Where E is the extinction, b is the acquired spectrum, v and d are the bright and dark references acquired at the beginning of the experiment, respectively (see Figure 2.9).

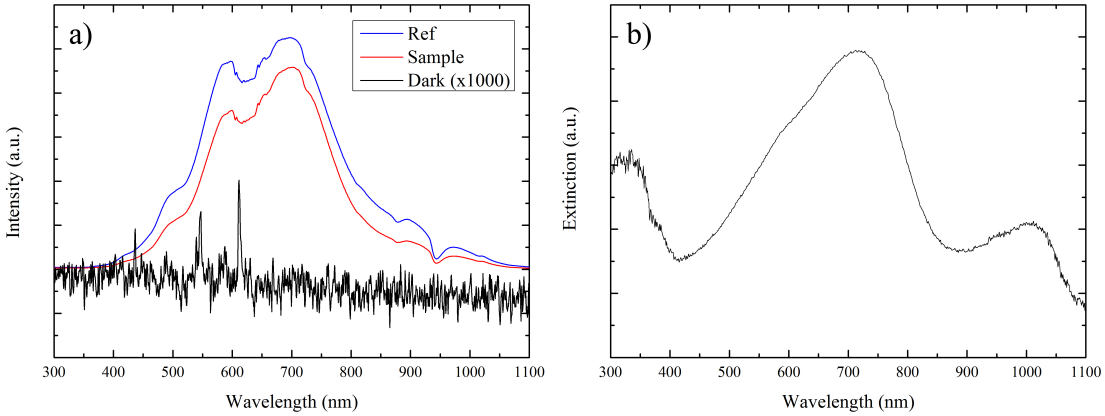

Figure 2.9: Acquisition of INPS spectra - a) Each acquisition in an INPS experiment contains 3 spectra, shown in the plot. b) The extinction is calculated from these as explained in the text. The red curve in (a) and its relative extinction spectrum in (b) was acquired on a bare 0.5nm Au-sputtered glass slide, thus representing a case of direct nanoplasmonic sensing.

The LSPR in the extinction signal is identified, fitted with a 20^{th} grade polinomial and thereby analyzed. The plasmonic peak maximum, its center of mass, FWHM, skewness and intensity at given wavelengths are extracted from the polinomial fit and followed over time as other spectra are recorded. A plot of these parameters can be traced as a function of time, with a temporal resolution ultimately dependent on the spectrometer integration time.

This platform has raised a lot of interest in the scientific community as it provides a viable route for qualitative and quantitative analysis of catalytic reactions [62, 63], solar cell manufacturing [64], hydrogen storage [65] etc. The great potential of this technology motivates the implementation of INPS in various experimental setups and in combination with other investigation techniques. In Section 6, a system for combined TEM and INPS is presented.

3

Experimental

As mentioned in Section 1.1, the growing interest in photoacatalysis entails the development of instruments for their characterization with broader capabilities. ETEM is now an instrument routinely used for heterogeneous catalysts characterization for its unique ability of offering high resolution images in a reactive environment (see Section 2.3). In this work new tools with the goal of expanding ETEM features in order to enable experiments under light illumination on photocatalysts are developed. Such technical development is necessary if a reaction environment appropriate for photocatalysts has to be recreated inside the microscope. The basic concept in this respect is to enable light activation inside the microscope column.

In the following sections, different approaches to accomplish this aim will be presented. Furthermore, the concept of light in the microscope is taken to a different level in Section 3.2 where TEM and light optical spectroscopy are brought together in a joint effort to give deeper insight in catalyst investigation.

Many components, connections and procedures described in this chapter are not meant to be optimized for production on any scale larger than prototype-level as this would be outside the scope of this project. In particular, the amount of hand-assembled parts, maintenance and *ad hoc* adaptation required is relevant for prototypes described in this Section. Requirements for commercialization is discussed in Section 7. However, working prototypes were built following relatively accessible solutions, leaving much space for refinement and further development.

3.1 First holder: light in

To begin *in situ* ETEM experiments with simulated working conditions on photocatalysts, a system for illuminating samples inside the microscope has been designed, implemented, tested and used.
The desired condition for *in situ* light activation is to have a means of controlling illumination of the specimen once in the microscope. As provided by the manufacturer the microscope column is dark, therefore a suitable illumination system has to be designed and implemented. In the pursuit of putting light inside the microscope several options have been considered, basing considerations upon practical limitations.

3.1.1 Concept

One possible solution of incorporating a light source in the microscope could be through ports in the microscope column. The advantage of this option is that it does not limit the use of the microscope with customized holders. Besides, this solution is desirable from a mechanical standpoint since it arguably requires little implementation effort, given the relatively large space available for manoeuvring. Indeed, a similar approach was successfully followed by [66–69].
Accessing the specimen through the specimen holder itself, is another viable solution. Although it may seem a constriction, this solution is advantageous in many ways. First of all, a dedicated sample holder for *in situ* illumination can be used in all microscopes having the same holder standards and specifications (typically, every manufacturer has its own standard). Moreover, given the substantial similarity among the most common standards, once the basic design is established it can be relatively easily adapted to different holder types (e.g. Jeol, FEI, etc.). Interchangeability of the light source and optics is a major advantage of this solution. The Titan 80-300 used in this work has eight ports accessing the pole piece gap (which is therefore labelled "octagon"), each occupied by the following accessories: Specimen holder entry ("Compustage"), cold gas trap ("cold finger"), energy dispersive X-ray (EDX) detector, gas inlet, two gas outlets, bypass to turbo pump, and the objective aperture. The holder option is therefore an ideal solution for implementing a light source.

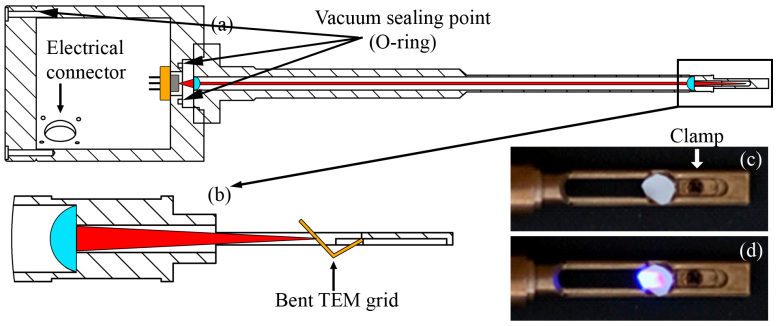

Figure 3.1: Lens-based holder (LB-TEM) - Schematic cross-sectional view of the lens-based specimen holder. (a) The feedthrough on the left hosts a laser diode, connected through a mini-DIN connector installed in the lateral port. Two interchangeable lenses (shown in blue), selected for the chosen laser wavelength, collimate and focus the light onto the sample. (b) Close-up cross-sectional side view of the tip. The sample (shown in yellow) is bent in order to allow it to be exposed to both light and electron beam. (c) and (d), photographs of the tip with the illumination off and on, respectively. The vacuum sealing points —where O-rings are located— are indicated by black arrows.

3.1.2 Design

The lens-based holder design (LD-TEM), which is shown in Figure 3.1, comprises a standard TEM specimen holder with a customized tip and bottom feedthrough.

During design phase, the holder was divided into three principal sections: bottom feedthrough, barrel, and tip. To maximize flexibility, the barrel is kept fixed and the two extremities were designed for a quick and easy connection to it. Tip and feedthrough are the most important parts in the custom design of a TEM specimen holder as they host the major modifications from a "standard" model. The feedthrough (see Figure 3.2) is the interface between the microscope interior and the outer atmosphere, being the entrance and exit gate for cables, tubes, actuators, etc. The tip hosts the sample and therefore is necessarily the end point for any feedthrough component and the acquisition point for signals. It is also the smallest and, often, most delicate part of the whole assembly, thus requiring special care during design.

The holder used as a working base was drilled along its axis (see Figure 3.1). A spare Fishione® 2020 single tilt holder tip —drilled axially up to the specimen recess location— was provided separately, requiring minor mechanical adaptation to fit in the barrel. The tip was made interchangeable with an adaptor design that was subsequently adopted for all custom tips described in this chapter (see Figure 3.3). The 2020 model provides a double clamp to anchor the sample to the specimen holder. A

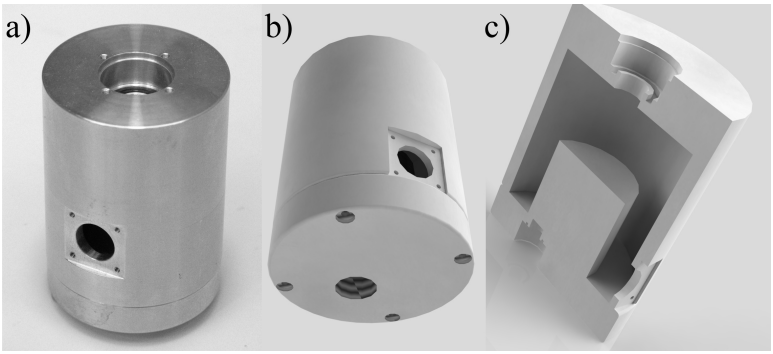

Figure 3.2: Bottom feedthrough - a) Manufactured feedthrough in aluminium, equipped with nitrile O-ring in the top recess used to connect the holder barrel. b) 3D rendering of the feedthrough and c) cross sectional view, showing the position of the lead plug.

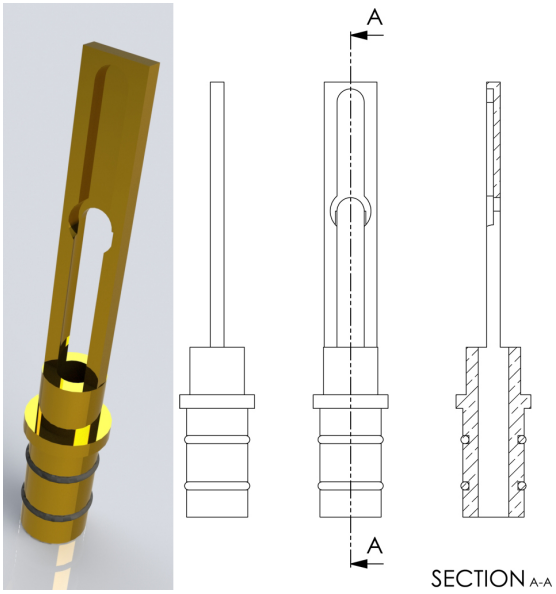

Figure 3.3: Tomography tip - 3D rendering and schematics of the Fishione® 2020 single tilt holder tip. The custom insertion system consists in two O-rings located at the insertion side, ensuring mechanical stability as well as interchangeability.

single clamp is left after the drilling, but is sufficient for retaining the sample firmly in place. The feedthrough contains a host structure for the laser diode, a mini-DIN vacuum-proof interconnect, cables connecting the mini-DIN connector to the diode, and a cast lead cylinder for X-ray shielding. The latter element is crucial for protection of the user against X-rays emitted upon electron-matter interaction near the specimen region. Shielding reduces the intensity of radiation exponentially depending on the shield material thickness and density. Lead has a so-called halving thickness of about 1cm, which means that radiation intensity is halved after traversing 1cm lead. Given the very limited solid angle for X-ray propagation through the specimen holder, typically a thickness of 2cm would be more than sufficient to reduce X-ray radiation below safety levels (3mSv/year). The lead plug was designed as thick as the surrounding features allowed. However, given the high density of lead ($\sim$11.3g/cm^3), the total volume employed for the X-ray shield has to be limited in order to prevent excessive unbalance in the mounted holder. An odd-balanced holder could cause malfunctioning in the micrometers in the CompuStage dedicated to specimen holder movement inside the microscope.

A laser diode casing is positioned on-axis and is equipped with an adaptor to host Thorlabs® mounted lenses. Various 3-pin 5.6mm-packed laser diodes and appropriate lenses can be interchanged while the holder is not in operation. The diode is connected to the external power supply via a connector contained in the feedthrough, connected itself with the mini-DIN plug. The 5 contacts can be used for other purposes, e.g. specimen biasing. Electrical leads can be passed through the holder barrel via openings in the laser diode casing. Vacuum is held by O-rings, positioned as shown in Figure 3.1.

In a second version of the holder (labelled FB-TEM) the laser diode casing and the lenses are substituted with a single or multiple optical fiber, passing through the entire barrel length up to the specimen. Large core multimode fibers from Thorlabs® were chosen (see table 3.1.2), passed through holes drilled in the bottom feedthrough and sealed with Crystal Bond® resin.

As the fibers are made from silica and in close proximity to the sample, coating with a suitable conducting layer (e.g., silver paint) and connection to the holder is necessary in order to avoid charging effects in the electron beam. To minimize charging problems, fibers were sputter-coated at the bare end with a thin carbon layer, which does not hinder light transmission but renders the fiber end facing the sample more conductive.

Wavelength range	Number of fibers	Outer diameter (µm)	Core diameter (µm)	Cladding diameter (µm)	Numerical aperture (NA)
UV-VIS (180 to 1150 nm)	2	750	550	600	0.22
UV-VIS (180 to 1150 nm)	1	1000	600	630	0.39
IR-VIS (400 to 2400 nm)	1	900	600	660	0.22

Table 3.1: Fiber optics - Description of fiber optics features as per manufacturer specifications.

The cleaved end is in fact the most exposed to the secondary electrons emitted by the sample and therefore the most critically affected by charging. The illumination cone is defined by the fibers. The illuminated region, 1.5 mm in diameter, is determined by the distance between fiber and sample and can be observed in the light optical microscope prior to TEM examination.

Thorlabs® components were used to construct a laser system for use as a light source. A TCLDM9 thermoelectric-cooled (TEC) mount for 5.6 and 9mm laser diodes was connected to a TTC001 T-Cube TEC Controller for controlling the laser temperature and a TLD001 T-Cube laser diode controller as diode driving unit. λ=405 nm, P=120mW, single mode Mitsubishi ML320G2-11 laser diodes were mostly used (see sections 4.1,4.2,4.3 and 4.4). Since UV laser diodes are expensive to purchase and not very powerful, an incoherent UV (λ=365 nm) fiber-coupled high-power LED light source (M365F1) was used in experiments requiring UV radiation (see Section 4.5).

The LB-TEM offers the advantages of greater power transmission, no need for auxiliary equipment, light focusing capability and the possibility of producing a small laser probe of very high intensity, while the versatility of the FB-TEM design is preferable for some applications. As the laser casing in the LB-TEM, once evacuated, does not dissipate the heat produced by the laser diode during operation, the laser efficiency is not constant over time. Furthermore, the choice of wavelength is limited to that of commercially available laser diodes and there is a limited possibility of using broadband sources. Finally, as the entire cavity is connected directly to the microscope vacuum system, light sources cannot be exchanged while the holder is in operation. All of these aspects are relevant for the experimental design but do not significantly limit the appli-

cability of the LB-TEM, which remains effective and easy to operate. The two models in combination offer complementary options for *in situ* experiments.
Technical drawings (see Appendix A) were sent to a mechanical workshop where the holder tip and bottom feedthrough were manufactured using MS 58 (58% Cu, 42% Zn) brass and aluminium, respectively. Nitrile (NBR 70) o-rings from M-Seals® were used for the sealing surfaces and for the tip interconnect.

3.1.3 Testing

Once assembled, the LB-TEM had to withstand two critical basic tests: vacuum leaking and X-ray safety. The vacuum-ability was tested using a custom built test chamber (see Section 3.3) that allows pumping specimen holders down to high vacuum conditions (about 10^{-5}mbar).
Typically, handling of components during machining and assembly causes dirt (hand grease, glue or solvent residuals, etc) to be deposited. Whereas device cleanliness is maintained to a maximum by handling components with gloves, some level of dirt is tolerated. Vacuum testing is sensitive to excessive handling in that pumping time is increased by the presence of dirt and volatile residuals, and the ultimate vacuum pressure is worse. However, if a vacuum leak is not present and a base pressure of $\sim 10^{-5}$mbar is achieved, the test is considered passed and the holder is subsequently tested for X-ray leakage.
X-ray testing is performed in the microscope. The specimen holder is loaded with a TEM copper grid, inserted in the column, the electron beam intensity is maximized by reducing the spot size, and a portion of the copper mesh is positioned under the beam. Under these conditions the X-ray production is maximum and therefore a worst case scenario for X-ray leakage. A Geiger meter is positioned in proximity of the holder feedthrough and used for X-ray emission monitoring while the copper grid is irradiated with the electron beam.

3.2 Second holder: light in and out

ETEM is a powerful technique for materials analysis and *in situ* studies of catalysts, as described in Section 2.3. One important aspect to consider in every *in situ* TEM investigation is the electron beam effect, which unavoidably affects the sample in a

more or less predictable way depending on the atmosphere present in the microscope, the specimen and mode of operation. For a more detailed treatment of beam-sample interaction refer back to Section 2.3. Furthermore, TEM is by nature a very local technique, in that the sample area analyzed is typically in the order of 10^2—10^6nm^2 over an entire sample area of about 7mm^2. For demanding high resolution ETEM studies the observed area is on the low end of this range. Whereas the advantage of such high magnifications allows for detailed study of matter at the atomic scale under reaction, simultaneous assessment of the large-scale sample behavior is challenging. Besides, the behaviour of the sample on the local scale could be influenced by the beam effect (see Section 2.3).

These considerations generated interest in the implementation of a technique capable of probing the entire TEM specimen area during conventional TEM/ETEM operation, at the same time and providing complementary information. INPS (see Section 2.4) was chosen for this purpose as it proved a sensitive tool for heterogeneous catalytic processes [61, 62, 65, 70, 71]. TEM and INPS work in a synergistic way since TEM is able to probe matter on a local scale and INPS is a spectroscopic technique that collects and integrates the LSPR signal coming from the whole specimen, providing information complementary to the TEM analysis. Moreover, TEM provides the local-scale information which is missing in independent INPS studies and gives detailed insight essential for strengthening of INPS result assessment. Complementary information achievable with the two combined techniques is of utmost relevance for the study of catalysis (see Section 6).

In this Section, the design and implementation of a dedicated TEM specimen holder which provides a platform for *in situ* LSPR sensing experiments is described.

3.2.1 Concept

The concept of light handling in the microscope has been approached by several groups, as shown in Section 3.1. A single light guide has been implemented successfully for light illumination [1, 43, 66, 67, 69, 72, 73] or for light output [42, 74, 75] individually. However, the simultaneous implementation of a light source and an optical readout system was only recently proposed [41], and yet no results are reported in the literature.

A dedicated TEM specimen holder that includes a miniaturized optical system was designed to perform INPS measurements on samples in the ETEM. Collaboration with

Chalmers University of Technology and Insplorion® AB (Sweden) was established in order to accomplish this goal. Insplorion® provided the INPS system consisting of a combined light source and optical spectrometer.
An optical guide leads light from the source onto the sample, another guide picks up the signal ref lected by the sample and leads it to the spectrometer where it is read. A miniaturized optical system allows for geometrically reproducible light redirection in the sample area (see Figure 3.9).

3.2.2 Design

A combined LSPR system was designed for implementation within a dedicated TEM specimen holder (INPS-TEM), exploiting the template developed in Section 3.1. It consists of a mechanism that includes an electrical connector, a micro-heater system, a light-handling system and a sample support. Mechanical constraints dictated by the microscope pole piece gap (∼5mm) and a design easing fabrication of components were the major challenges to take on. The ability of manoeuvring samples within the microscope in the x,y and z axes as well as tilting along the α axis entail that an effective maximum device thickness of ∼2mm has to be considered in the proximity of the holder tip. Packing all the desired features in such a restricted space is a demanding challenge if all components had to be manufactured with conventional machining methods, therefore microfabrication was chosen for the development of key components in the system.
The setup shown in Figure 3.4 consists of a bottom feedthrough, a hollow barrel and a customized tip. The bottom feedthrough has been upgraded from the first model for accommodating two fibers. The fibers are introduced via a hollow sealed 3/4" national pipe thread (NPT) vacuum connector, which enables safer extraction and replacement of fibers in case of failure. The NPT connector can be filled with Crystalbond® 590 or M-Bond® 610 for fixing a new pair of fibers. The use of a thermoplastic glue like Crystalbond® allows replacement of fibers upon heating of the NPT feedthrough.
A more rudimentary system used at early implementation stages consists in a simpler feedthrough without NPT connector. Here, fibers are inserted directly via two holes in the bottom sealing lid and fixed with epoxy glue.
All the fibers are buffer jacketed, terminated with SMA 905 connectors on the air side, stripped (3-5 mm) and flat cleaved on the vacuum side. Stripping and cleaving was

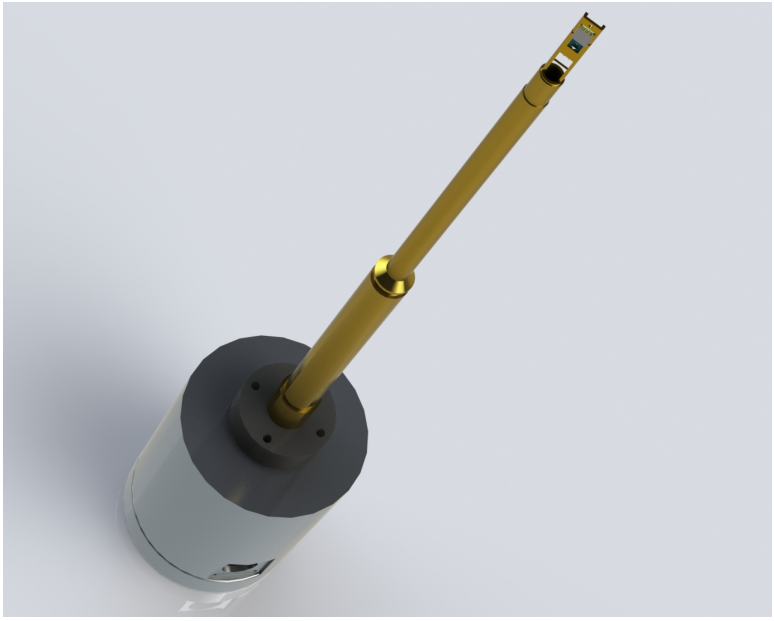

Figure 3.4: LSPR-TEM holder - 3D rendering of the full holder equipped with tip and bottom feedthrough (shown in detail in figure 3.2)

made by hand using a scalpel once the fibers were positioned near their final location inside the holder. The illumination cone escaping from each fiber is limited by its numerical aperture (NA), which is defined as

$$NA = \sqrt{n_{core} - n_{cladding}} = n \sin\theta \tag{3.1}$$

where θ is the half-angle of acceptance/radiation and n, n_{core} and $n_{cladding}$ are the refractive indices of the medium where the radiation propagates out of the fiber, the fiber core and the fiber cladding, respectively. θ is approximately 5.8° and 12.7° for the chosen fibers, corresponding to a total divergence angle of 11.5° and 25.4°, respectively. The chosen fibers are listed in Table 3.2.2. The 0.1NA fiber is chosen for light input, as the maximum escape cone is limited to 11.5°. The other fiber is chosen for signal pickup, given the larger acceptance angle. A calculation of light transmission efficiency, carried out in the hypothesis of perfectly planar and reflective surfaces and zero insertion losses, gives a maximum of ∼35% light transmitted in the system.
A rectangular mirror chip is the core system for light handling within the holder tip (see Figure 3.5). It contains two reflecting surfaces at 45° to the chip surface and 90° with respect to one another. Two trenches lead to the reflection chamber parallel to

	HPSC25	SFS105/125Y
Fiber type	Multimode	Multimode
Numerical Aperture (NA)	0.1	0.22
Equivalent acceptance angle	11.5°	25.4°
Core diameter	25 ± 3µm	105 ± 2µm
Cladding diameter	245± 10µm	125µm
Operating wavelength	280 to 750nm	400 to 2400nm

Table 3.2: Fiber optics - Description of fiber optics features as per manufacturer specifications.

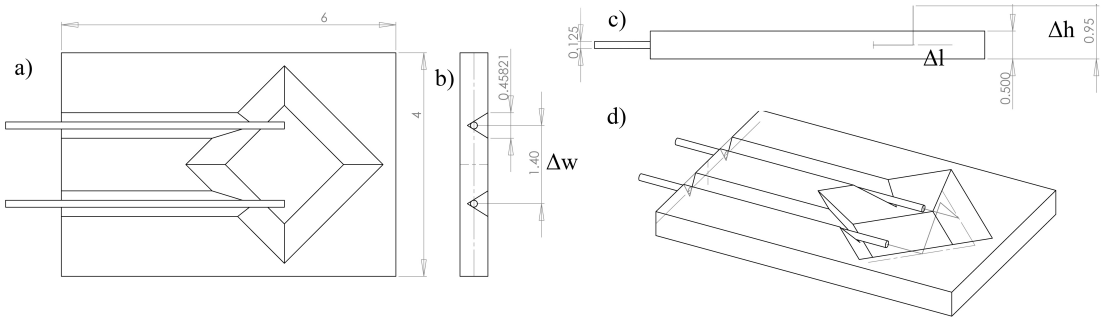

Figure 3.5: Mirror chip schematics - Technical drawing illustrating the mirror chip layout. Dimensions are shown for the adopted model. a) Side view, with indicated thickness of the fiber and height of the light path. b) Top view, with indicated total lateral dimensions. c) Bottom view, with indicated distance between fibers and positioning within the recess. d) Isometric view.

the long side of the chip and hold the two optical fibers in place. This geometry allows light coming from one fiber (labelled A) to be reflected out of plane at an angle of 45° with respect to the wafer surface and 90° with respect to the incoming light beam. If a reflective surface is positioned parallel to the mirror chip, light would bounce off it and follow a path symmetric to the one described until it is captured in the second fiber (labelled B). Conventionally, anisotropic KOH chemical etching is used to obtain crystallographically-defined planes at 54.7° with respect to the chip surface, which is evidently not suitable for the desired reflection geometry. Therefore, the chip was fabricated from a 500µm thick silicon wafer via non-conventional wet etching methods in order to achieve 45° planes in silicon.

The mirror chip design and the choice of fibers were strongly entangled. A trade-off between maximization of the mirror surfaces and the total chip thickness had to

be faced. Since the mirror surfaces are tilted 45° with respect to the wafer surface, their width is calculated as $\sqrt{2}t$, where t is the wafer thickness. A larger reflecting surface would mean a thicker wafer, which would add up to the total device thickness, limited to the pole piece gap constraints mentioned above. Grooves were designed to accommodate the largest fibers available from Thorlabs®. Fibers with 125µm cladding diameter were chosen in order to sit in the etched chip recesses at half chip thickness (see Figure 3.5). The light path of an axial light beam can be traced in the design software as a function of other dimensions. If symmetry is maintained across the longitudinal centerline, the position of the reflection vertex in the y and z axes depends on the spacing between the grooves. If Δw is short, Δh and Δl get shorter too, and viceversa (see Figure 3.5). An inter-fiber distance of 1.40mm was chosen, which corresponds to a 0.45mm elevation of the reflection apex from the upper chip surface and a 0.70mm displacement from the window center.

A custom MEMS heater hosting the INPS sensor was designed to enable *in situ* heating and hold the sample on an electron transparent yet optically reflective surface for reflection LSPR measurements (labelled S-MH). The chip (see Figure 3.6) is fabricated from a 350µm-thick silicon-on-oxide (SOI) wafer and consists of a silicon membrane suspended on a squared opening in the silicon wafer. The membrane is connected via 4 arms to the chip, each leading to one electrical pad. 30nm-thick silicon nitride (Si_3N_4) electron transparent viewing windows are etched in the membrane to allow for TEM investigation. The INP sensors are patterned on top of this structure via shadow mask lithography and embedded in an extra layer of nitride (an S-MH with INP sensors is labelled LP-MH). This extra dielectric layer is indispensable for insulation of the INP sensor fom the surrounding environment (see Section 2.4) but adds to the total thickness within the viewing windows. Heaters can be produced without INP sensor for conventional heating experiments, maintaining electron transparency at a maximum.

Whereas a similar device was developed by Creemer and colleagues [38], the INPS device was substantially redesigned to take into account various issues. To begin with, heat is generated by the Joule effect in the silicon arms suspending the membrane itself. Heat is then transferred to the membrane via thermal conduction. Heating is current-driven (see Figure 3.7). Forcing a current I_0 in two arms and sinking the same current in a third ensures current symmetry and therefore a symmetric temperature distribution. Simulations were performed to optimize the structure geometry with

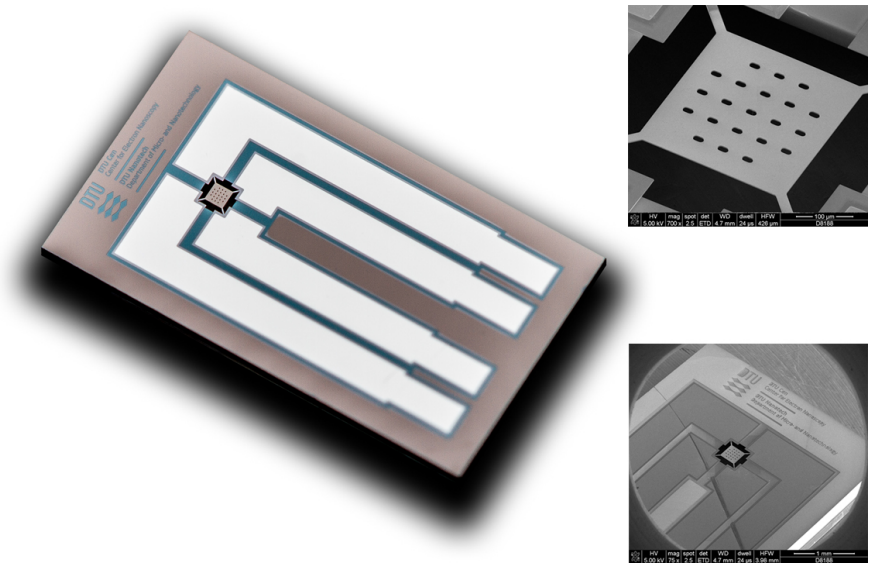

Figure 3.6: Heater chip - Photograph of the chip and SEM images of the membrane area in detail. In the large photo, the overall geometry and the position of the contact pads is shown. The suspended membrane hosts 21 viewing windows. See Figure 3.8 for simulations of this structure.

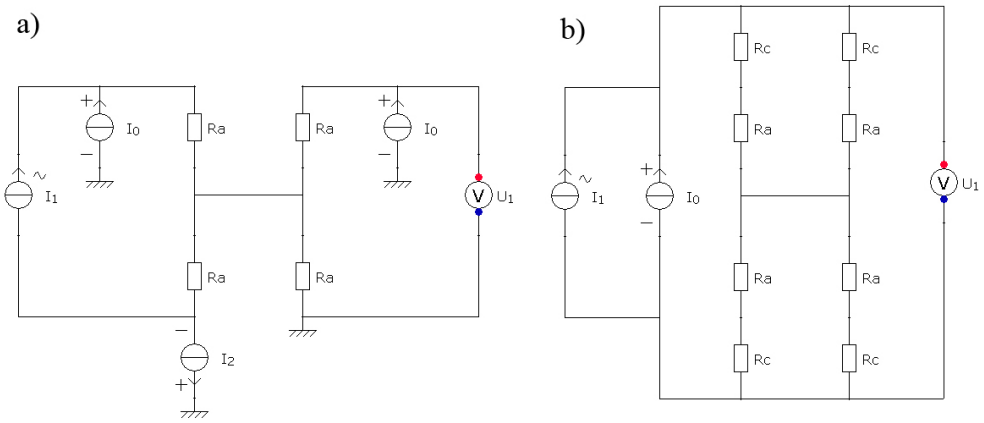

Figure 3.7: Heater circuit - a) Optimal electrical circuit representing the heater system. 3 independent and synchronous DC current sources and one AC current source are connected to the membrane terminals (R_a). A small AC current (A_1) is forced between two terminals while the resulting AC voltage (U_1) is read by the AC Voltmeter across the other two, allowing simple sheet resistance measurements in Van der Pauw geometry. 3 distinct current sources allow for high control over the current flowing in each arm. b) A simpler version of the same circuit, with just one current source. Here, R_c=R=1kΩ $\gg R_a$. Under this condition the circuit is effectively current-driven, current irregularities are taken up by the biggest load and the arms do not suffer from current runaways, therefore attaining a more homogeneous heating.

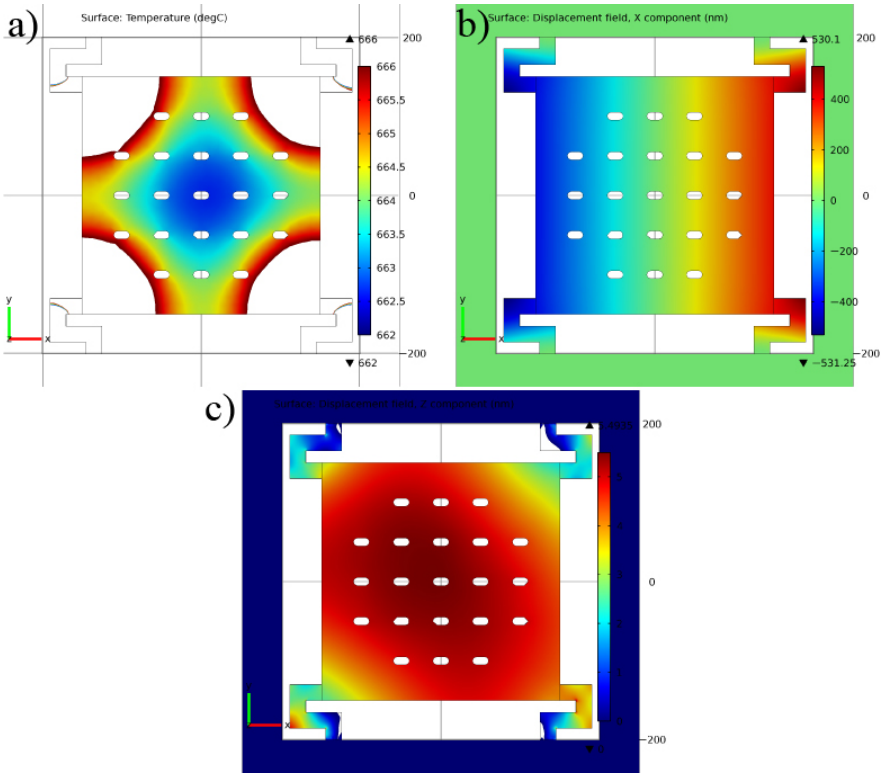

Figure 3.8: Heater simulations - Comsol simulations of thermal and mechanical behaviour of the heater in operation. a) Surface temperature of the device, showing a finite but minimal thermal gradient across the structure. The highest gradient is present near the corners, therefore viewing windows are not patterned in this area. b) X-axis component of the horizontal displacement due to thermal expansion. This expansion is challenging to avoid since it is purely related to the material properties. In an ideal structure, though, at the center of the membrane the displacement is zero. The suspending arms are zig-zag shaped in order to take up some of the vertical displacement shown in c).

respect to temperature distribution and mechanical deformation. Two membrane types were designed and manufactured, one with straight arms and one with zigzag-shaped arms. The second design is meant to accommodate for the buckling effects arising from thermal expansion in the chip upon heating, so that some of the expansion stress is taken up by the arms.

The major difference with Creemer's design is thus the absence of a metallic coil that accounts for the heating. Here, some of the major considerations in merit are presented. A heated metallic coil is catalytically active itself. Therefore, a small imperfection in the coating layer could be detrimental if a catalyst system is under investigation. Embedding such a metallic feature in a dielectric layer would be more challenging

from a manufacturing standpoint. Si_3N_4 is deposited in a CVD furnace where metals exposed to the high deposition temperatures can become volatile and contaminate the entire chamber. The metallic coil could potentially interfere with the INP sensor layer above, or it could behave as a buried reflective surface and generate unwanted internal reflection paths within the upper device layers.

Aluminium contact pads have $\sim 1\Omega$ resistance. A $\sim$100nm-thick oxide layer is typically formed on top but this does not affect contact quality as the spring contacts cut through the oxide when pressed against it. Contact branches are $\sim 100\Omega$ each, depending on the doping variations. The plasmonic structure is excluded from the viewing windows by accurate design of the shadow mask.

A brass fixture hosts the two chips in place—the mirror chip being fixed with epoxy and the interchangeable heater being fixed with a screw-in lid (see Figure 3.9). Fibers are located and glued in position on the mirror chip, resin-coated electrical wires are driven to the tip end through the side recesses and embedded in epoxy. A Samtec® SEI-112-02-G-S-AB interconnect was cut with the help of a diamond saw and glued in position within the tip, serving as electrical connector for the heater chip. Arc-shaped gold-plated phosphor bronze spring contacts stick out of the top surface, allowing for easy contact when the heater is pressed against it by the lid. The connector body is insulating, made in liquid crystal polymer. All polymers and glues used in the assembly are low degassing and high vacuum-proof.

Van der Pauw measurements (see Figure 3.7) can be carried out on the structure by forcing a small AC current between two terminals ($I_1 \leq 1$mA AC$\ll I_0$). The resulting sheet resistance can be calculated reading the AC voltage drop across the opposite two terminals (U_1), as follows:

$$R_{\square} = \frac{\ln 2}{\pi} R \tag{3.2}$$

Where $R_{\square}$ and R are the sheet resistance and the measured resistance, respectively. This simplified version of Van der Pauw measurement works in the assumption that the system is symmetric. In this case symmetry is broken by the oval shape of the viewing windows, therefore the measured voltage depends on the choice of contacts points. Comsol® simulations show that the resulting asymmetry can be compensated by applying a numerical correction factor.

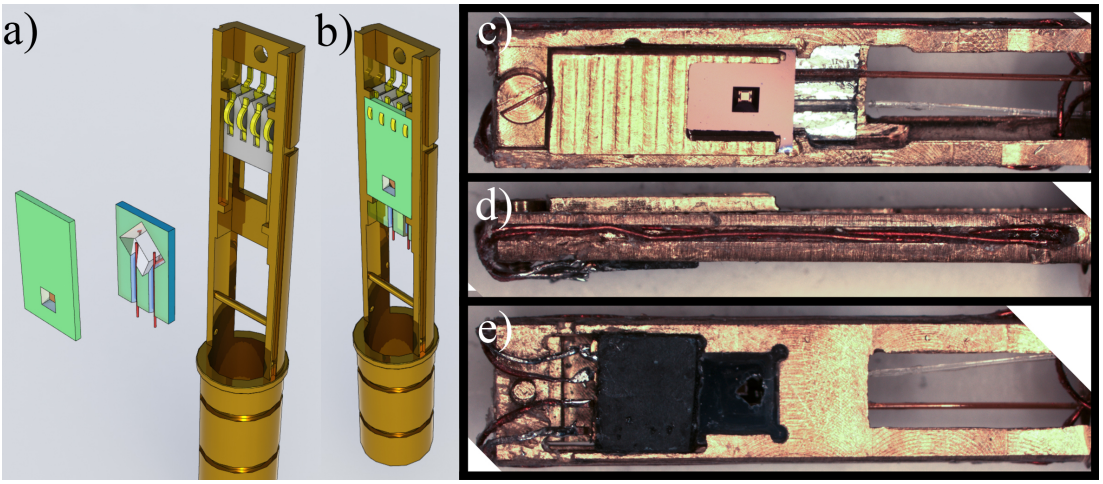

Figure 3.9: INPS-dedicated tip - a-b) 3D rendering and b-d) light optical microscopy images of the custom tip. In a) an exploded view showing each individual component is depicted. b) is the 3D rendering of the packed structure, 1.75mm-thick. c) Top view of the tip, loaded with all chips, fibers and contacts in place and fixing lid screwed in. d) Side view, showing the side recess with embedded wires. e) Bottom view, showing the interconnect with soldered contacts.

3.2.3 Testing

The INPS-TEM was subject to the same tests described in Section 3.1.3 for vacuum compatibility and X-ray leakage. Vacuum was more difficult to achieve in this case, given the higher complexity level and the abundance of glued components, which likely embed air bubbles and can potentially crack.

Electric connections and heating tests were the most challenging in this case. The thin resin-coated wires have a tendency to peel off when bent around sharp fixture edges. Epoxy serves as an excellent remedy for this and has the additional advantage of fixing wires in place at critical points such as corners and passing holes (see Figure 3.9d). Soldering must be done at the lowest temperature possible not to alter the interconnect and burn any neighbouring glued component. However, non-thermoplastic glues were used in the vicinity of the heater in order to avoid melting during heater operation.

First proof-of-concept tests were performed in the *ex situ* chamber (see Section 3.3) for heating performance, initially without a readout system (AC current source and associated voltmeter, see circuit in Figure 3.7). The advantage of batch-produced heaters is efficient trial-and-error testing of different driving circuit configurations and settings. Current was forced in the circuit at fixed steps of 5mA until red heat (i.e.

the threshold for visible black body radiation emission) was reached. One thing to be noted is that red heat corresponds to a temperature of ∼700°C, which is already above the needed reaction temperature for many catalytic processes. The system was kept at that current value for 30 minutes before increasing the current in further 1mA steps. Threshold for first visible glowing was ∼30mA for the circuit configuration shown in Figure 3.7b, without control resistors R_c. Failure usually occurs at ∼40mA. Inspection of the membrane after failure with an optical microscope shows buckling effects which are likely the cause of arms rupture. By the time the membrane breaks, the heater is glowing almost white, which corresponds to a temperature well above 1000°C [76]. This means that we can safely run the heater without visible light contribution of black body radiation within the temperature range relevant for many ETEM experiments, typically below 700°C for studies of catalysts.

In vacuum, all other components in the assembly remain unaltered upon membrane failure, which means that heat is efficiently confined to the membrane area. In H_2 atmosphere at a pressure of 3mbar the behaviour is different. Greater currents can be forced in the circuit, up to ∼60mA before membrane failure, which is expected since gas convection becomes a dominant means of heat dissipation. Some of the glued parts degraded, even those glued with non-thermoplastic glues, resulting in component detachment, and the interconnect was partly molten. This behaviour can be explained considering kinetic theory of diffusion. In kinetic theory, the mean free path ℓ of identical gas molecules with Maxwell distribution of velocities can be described as

$$\ell = (\sqrt{2} n \sigma)^{-1} \tag{3.3}$$

Where n is the number of target particles per unit volume, and σ is the effective cross sectional area for collision. By rearranging the equation, it can be shown that the mean free path is

$$\ell = \frac{k_B T}{\sqrt{2} \pi d^2 p} \tag{3.4}$$

where k_B is the Boltzmann constant in J/K, T is the temperature in K, p is pressure in Pascals, and d is the diameter of the gas particles in meters. For a pressure range of $\sim 10^{-3}$—1mbar and at room temperature, values for ℓ correspond to ∼0.1—100mm. These values compare with the size of the volume enclosing the sample in the tip. This means that gas transports heat efficiently from the membrane to the surrounding

components, possibly even reacting given the high gas temperature. Unfortunately, the limited volume is unavoidable in the present design, but the temperature achieved at the time of rupture is well above relevant temperatures for most ETEM reactions, as mentioned above. This failure test was therefore made in order to assess tolerance limits of operation for the device under realistic atmosphere conditions.

3.3 *Ex situ* chamber

A system that simulates the interior of the ETEM was designed and developed to facilitate prototype testing, proof-of-concept experiments as well as first *ex situ* results. The system consists of a spherical cube vacuum chamber (MCF275-SphCube-C4A8 from Kimball® physics) with 9 ports for connecting various instrumentation (4 CF 133 flanges and 5 CF 275). Various vacuum flanges were applied to the ports to connect the spherical cube with the rest of the equipment.

A TEM specimen holder can be inserted in the vacuum chamber via a custom insertion port which was constructed using a spare entry port from a Fishione® 1020 Plasma Cleaner and a standard KF 275 pipe. The entry port was welded into a KF 25 blank flange which in turn was connected to the pipe. The welding position is critical for the correct placement of the holder tip within the spherical cube and was calculated from technical drawings of the assembly (see Figure 3.10).

Optical feedthroughs were equipped with custom-built fiber collimators. Lenses were taken from commercially available COL-UV/VIS from Avantes® and adapted to the designed aluminium casing. Two opposite CF 133 ports were used for the optical feedthroughs in order to allow for light reflection experiments on the inserted sample, with an incidence semiangle of 30° from the normal to the specimen surface (see Figure 3.10). The optical ports provide the ability of accessing the specimen in the chamber with a collimated light beam and pick up the reflected light maximizing collection efficiency. Such an optical implementation can provide a solution for optical calorimetry using a pyrometer or emission spectroscopy using any holder that does not contain an optical source and/or probe.

To pump the system, the chamber is connected to a Pfeiffer® Turbo molecular pump (TMP) backed by a roughing pump via port number 5 (see Table 3.3).

The system can achieve a base pressure of about 10^{-5}mbar, dependent on the holder

Port number	Flange type	Model	Manufacturer	Connection to
1	Blank, non-rotatable	CFB034	Scanwel®	Nothing
2	Blank, non-rotatable	CFB034	Scanwel®	Nothing
3	Fiber optic feedthrough (100 micron fiber core UV/VIS)	FO1UV-133	Accuglass®	Light source
4	Fiber optic feedthrough (100 micron fiber core UV/VIS)	FO1UV-133	Accuglass®	Light spectrometer
5	CF to KF adapter	CFRK070-16	Scanwel®	Turbo pump
6	CF to KF adapter	CFRK070-25	Scanwel®	TEM specimen holder
7	Viewing port	VP-UV-C40	Cayburn®	Observer
8	Viewing port	VP-UV-C40	Cayburn®	Observer
9	Pressure sensor feedthrough	WRG-S-NW25	Edwards®	Wide range pressure gauge

Table 3.3: Vacuum chamber - List of components attached to the *ex situ* vacuum chamber.

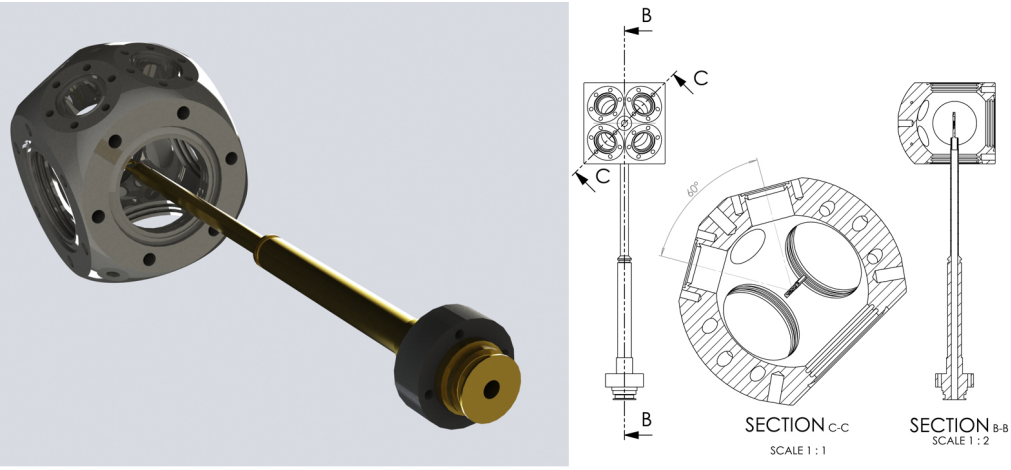

Figure 3.10: Vacuum chamber—cross section - Three dimensional rendering and cross sectional view of the *ex situ* testing equipment. The device is represented with a holder inserted for ease of visualization. Measurements were performed on the relative technical drawings for ensuring appropriate positioning of the holder tip with respect to the center of the vacuum chamber. Section C-C highlights the angle between the two optical feedthrough ports.

inserted. This is comparable to the pressures attainable in the ETEM. Ports 1 and 2 are left to the application of a gas handling system, ideally for a gas inlet and outlet, respectively. The chamber is anchored to an *in situ* X-Ray Diffraction (XRD) system in order to exploit its gas handling system, which has the advantage of being able to reach atmospheric pressure. The use of a specialized TEM holder for sample transfer under controlled atmosphere in combination with the vacuum chamber allows sample exposure to higher pressures during ETEM experiments, maintaining the ability of doing optical spectroscopy on the specimen. Further development of this device and its potential use will be discussed in Section 7.

In conclusion, design and construction of three working prototype specimen holders (LB-TEM, FB-TEM and INPS-TEM) was successfully accomplished. The holders respond to the need for introducing a light source and an optical readout system in the TEM. This achievement allows study and development of light sensitive materials and photocatalysts in particular.

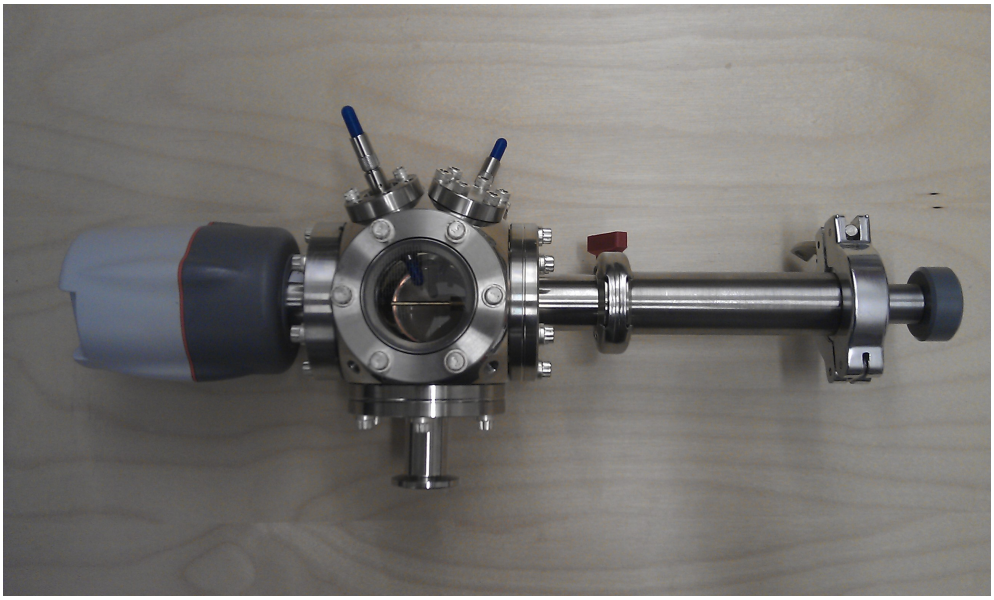

Figure 3.11: Vacuum chamber—photo - Photograph of the assembled system. The assembly comprises a pressure gauge (left), two fiber optical vacuum ports with collimator on the vacuum side, and insertion feedthrough for the specimen holder.

4

Light induced reactions

When light is absorbed by atoms or molecules, it can produce photochemical reactions such as photosynthesis. Photocatalysis is a branch of photochemistry that deals with light-induced catalytic reactions (see section 2.1.1). Often, photocatalysts undergo transformations during synthesis or use. In either case, atomic scale studies of the effects of such transformations are vitally important for understanding the activity principles or deactivation mechanisms of a specific photocatalyst. In this section, some effects of light-induced chemical reactions on photocatalysts are shown using TEM in combination with light activation (see section 3.1).
Some of the experiments described in this section are treated in detail with focus on the material science aspects (4.1,6,5). Other experiments are only briefly discussed as they primarily served as proof of concept experiments in a first experimental setup assessment phase (4.2,4.3,4.4,4.5).

4.1 Cu_2O photoreduction

Cuprous oxide (Cu_2O) nanoparticles are reported as an active photocatalyst for HER and can be synthesized in a cheap and reproducible way [77]. Even though the bandgap (2.0-2.2eV) is sufficient for performing overall water splitting (see Section 2.1.1), the valence band (VB) is too positive with respect to the water oxidation potential (see Figure 4.1). Besides, the bandgap straddles the redox potentials for Cu reduction and oxidation. Therefore, the sample undergoes self-degradation upon light irradiation in

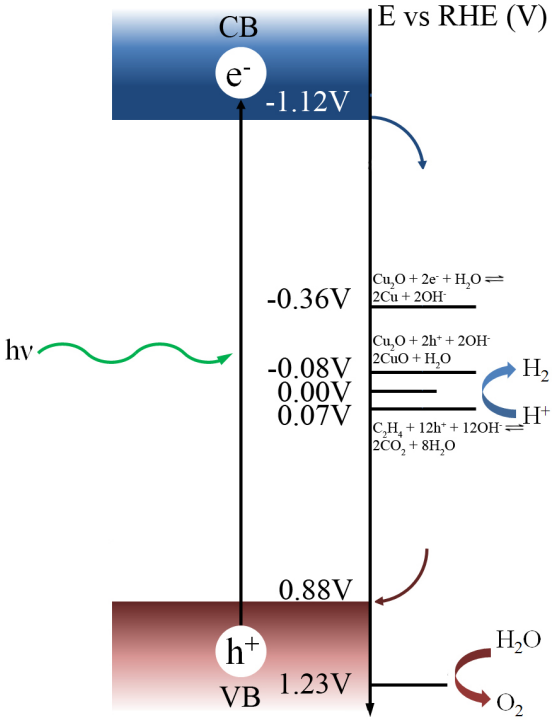

Figure 4.1: Cu_2O band diagram - The position of the Cu_2O band positions and relevant redox potentials for the water splitting reaction are shown vs. RHE [78, 79].

the presence of water, according to the following reaction scheme

$$Cu_2O + h\nu \longrightarrow Cu_2O + h^+ + e^- \tag{4.1}$$

$$Cu_2O + 2\,e^- + H_2O \longrightarrow Cu + 2\,OH^- \tag{4.2}$$

$$Cu_2O + 2\,h^+ + 2\,OH^- \longrightarrow 2\,CuO + H_2O \tag{4.3}$$

Whereas the position of the VB and the quasi-Fermi levels in Cu_2O has been debated [80, 81], Figure 4.1 shows that water oxidation cannot be driven by holes. However, a sacrificial reagent (exemplified by ethene in Figure 4.1) can be used to let water reduction happen on Cu_2O as the sacrificial agent is oxidized. It should be emphasized that semi-empirical calculation studies report a lower lying VB and thus the possibility of the kinetically slow photoelectrocatalytic water oxidation occurring directly on Cu_2O [82]. In either case, carbon contamination acting as a carbon source on the surface helps the photoreaction to occur. In the present case the sacrificial agent is supposed to be a residual surfactant used during the synthesis which is not removed

during the washing procedure. Small amounts of surfactant are very difficult to remove except by combustion. The combustion would change both the particle morphology and most likely also oxidize the Cu_2O to CuO and was therefore deemed unfeasible. Even in the presence of the sacrificial agent the photo-oxidation of Cu_2O to CuO should be thermodynamically favourable.

Unfortunately, cuprous oxide's tendency to photocorrode results in a loss of photocatalytic activity, as reported independently by Nagasubramanian [83] and Fleisch and Mains [84]. The photodegradation of Cu_2O was investigated by direct observation of the transformation process using imaging, diffraction and spectroscopy (see Figure 4.2). The combined use of these techniques allows for comprehensive characterization of the transformation process. To be able to follow the degradation over time, a "stop-and-go"-type experiment has to be performed. This means that the gas has to be pumped out of the microscope column before exposing the sample to the electron beam for acquisition of images. This type of quasi-*in situ* experiments is necessary to avoid the modification of the sample by the electron beam (see Section 2.3). Even though the structural information is not retrieved during exposure to light, the sample has been kept under controlled gas conditions and in the same setup and position making it straightforward to track the same area and particles during the extended series of exposures.

The microscope used was a Titan 80-300, operated at 300kV in TEM and scanning TEM (STEM) mode. EELS spectra were recorded in diffraction mode with exposure times between 0.5-4 seconds and dispersions of 0.1 or 0.5 eV/channel. Cu_2O nanocubes were prepared via solution phase synthesis [77]. The TEM sample was prepared by casting a drop of water-dispersed Cu_2O nanocubes onto a lacey carbon coated Au TEM grid. The grid was then cut with a scalpel, fixed to the specimen holder and bent to face the light beam as described in [1]. The sample was exposed to 5mbar water vapour and 6W/cm^2 light stimulation at λ=405nm for 15min, then the chamber was evacuated to a pressure $<10^{-5}$ mbar and light was turned off before recording new images. Water vapour was introduced in the microscope by evaporation of Millipore water (resistivity 18.2 MΩ) stored in a vial directly attached to the gas inlet system. A set of control experiments to assess the role of water, light and electron beam independently was performed (see Table 4.1).

A time-resolved ETEM analysis of the photodegradation process was carried out by

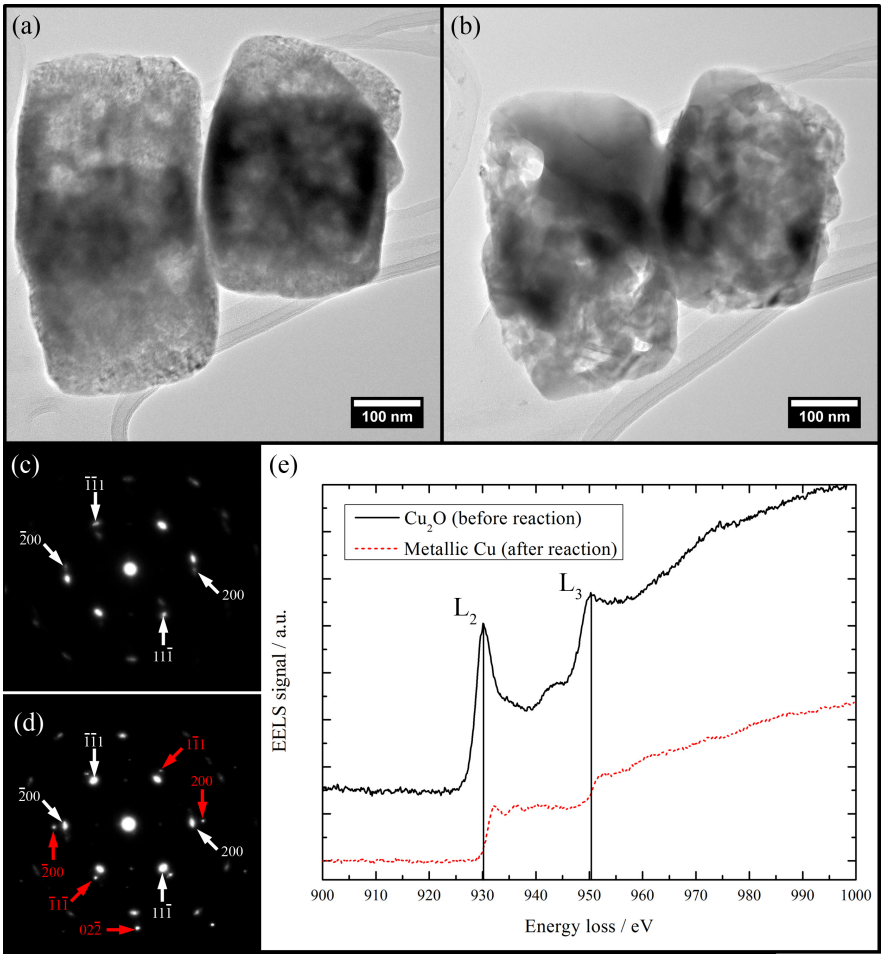

Figure 4.2: Cu_2O photocorrosion - (a), (b) Bright-field TEM images of Cu_2O nanocubes before and after reaction, respectively, showing changes in particle shape and morphology. No significant damage to the supporting carbon film was observed. The growth of large single crystals of Cu is observed. (c), (d) Selected area diffraction patterns in the [011] zone axis, indexed for Cu_2O (c) and for both Cu_2O and Cu (d). The area sampled by the selected area aperture is 400 nm in diameter and encompasses at least two of the particles shown in (a), (b). After the reaction, (d) contains spots representative of metallic copper, labeled in red. Spots from Cu_2O are still present as some portions of the particles are not completely reduced. (e) Electron energy-loss spectra of the same nanocubes. The upper curve is offset vertically for ease of comparison. The positions of the peaks of the L2 and L3 EELS edges are indicated by the vertical black lines.

Exp.	Gas	Pressure (mbar)	Electron beam	Light intensity and wavelength	Duration	Observed changes
1	H_2O vapour	3	Absent	Absent	5 hours	None
2	Vacuum	(10^{-6})	Absent	λ=405 nm, 6 Wcm^{-2}	5 hours	None
3	Vacuum	(10^{-6})	~100 $MWcm^{-2}$	Absent	20 minutes	None

Table 4.1: Control experiments - The sample was imaged, then exposed to the listed sets of conditions. After the indicated duration, the column was evacuated to a pressure of 10^{-5}mbar before new images were taken.

iterating water and light exposure, evacuation and analysis at regular intervals until the reaction was complete. A bright field (BF) image sequence of the photodegradation process at different reaction times, i.e. after 15, 30, 45, 60 and 75 minutes respectively, is shown in Figure 4.3 with the associated electron diffraction patterns. Every frame represents the sample condition at the time indicated in the figure. The frames were labelled from (a) to (f) for ease of reference throughout this Section.

At each time the reaction is paused as described above, nanocubes are characterized by means of BF imaging, electron diffraction as well as electron energy-loss spectroscopy (EELS). BF images of the samples provide a first evidence of a morphology change in the particles, which can be followed in time by monitoring the change in overall contrast, size and appearance of the sample. In Figure 4.3, a change in morphology is evident across frames and especially among frames a), d) and e). The imaged nanocube undergoes a general shape change from an irregular shape with porous structure to a more cubic shape. More importantly, the diffraction contrast of the particle helps identifying individual crystals forming within the cube. These crystals appear dark and homogeneous in BF images, pointing to their crystalline nature as confirmed by diffraction pattern analysis. Electron diffraction patterns indicate the co-existence of both metallic copper and cuprous oxide phases at intermediate steps. The distinct diffraction spots belonging to the oxidic and metallic structure respectively are highlighted in the figure. The reduced phase nucleates forming metallic crystalline grains within the oxide matrix that expand with further reduction. The metallic grains take up copper from the Cu_2O matrix and grow following its orientation, as shown by electron diffraction in Figure

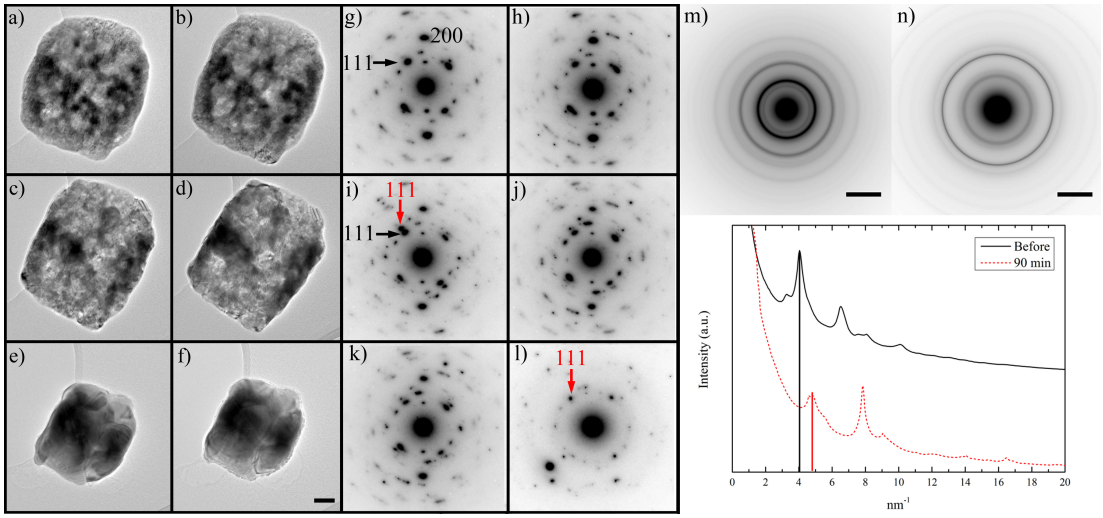

Figure 4.3: Photocorrosion - *In situ* ETEM image sequence of time-resolved Cu_2O nanocube photodegradation. The images are taken in absence of both water vapour and light illumination. The 111 reflection relative to Cu_2O and Cu are marked by the black and red arrows, respectively. The Cu_2O-111 reflection is shifted to higher reciprocal distances, consistently with what is expected for metallic copper. Scale bar: 50nm. Rotational average of the first and last diffraction patterns in Fig.4.3, and their relative radial intensity profile. The vertical lines in the intensity plot highlight the position of the (111) reflection in Cu_2O (solid black line) and Cu (dashed red line), corresponding to a spacing of 2.09$\mathring{A}$ and 2.46$\mathring{A}$, respectively. A shift towards larger spatial frequencies is noticeable. Scale bar is 5nm-1.

4.3. Diffraction spots from differently oriented grains present in the nanocube are observed in the patterns. The major contributions to the ED pattern come from crystals oriented in the [110] orientation, the {111} reflections being highlighted and followed over time as the reaction proceeds across frames g-n). ED shows that individual Cu grains in the reduced phase are single crystals, which suggests atom-by-atom growth over particle coalescence.

Careful analysis of BF and DF images allows the monitoring of individual grain growth within the nanocube (Figure 4.4). Given the difference in morphology among different frames a particle-tracking algorithm is not feasible; therefore, manual measurements were used to analyse the grain size. Measurement of all grains is impractical and often very challenging since they overlap in the projected TEM images. Rather, measurements on more clearly defined grains near the nanocube edges were carried out. Plotting the measured projected grain areas over reaction time and interpolating the resulting data points allows extraction of nucleation rates for Cu grains [85, 86]. The growth of the nanoparticles is expected to be dependent on 1) the generation rate of the Cu atoms and 2) the diffusion of the generated Cu atoms to larger particles. The former is linear in time as the generation is dependent on photons being absorbed in the limit of low light intensity and low Cu_2O conversion, i.e. when there is still sufficient amount of Cu_2O not to decrease the overall light absorption. As the amount of light absorbed could not be determined by this experiment it was not possible to determine if the particle growth was limited by generation or diffusion. However, the linear growth of the individual grains suggests an atom-by-atom grain growth mechanism.

In addition to a first qualitative reaction assessment by BF and diffraction, EELS spectroscopy was used to characterize the transformation quantitatively to determine reaction sub-steps and trends. The cuprous oxide nanocubes used in this study had dimensions of approx. 300±50nm as measured from BF images. At an acceleration voltage of 300kV, the electron inelastic mean free path (IMFP) for this sample is about 165nm [87]. Therefore the t/L ratio (where t is the sample thickness and L is the IMFP) is equal to about 1.5-2. A similar t/L ratio was also estimated using the Fourier-ratio and Kramers-Kronig sum rule [31]. When such high t/L ratios occur, plural scattering events cannot be neglected [31, 88, 89] and, as a result, the signal-to-background (S/B) ratio of core-loss EELS spectra is severely diminished. The Fourier-ratio deconvolution technique was applied to the core-loss spectra to remove the effects of plural scattering

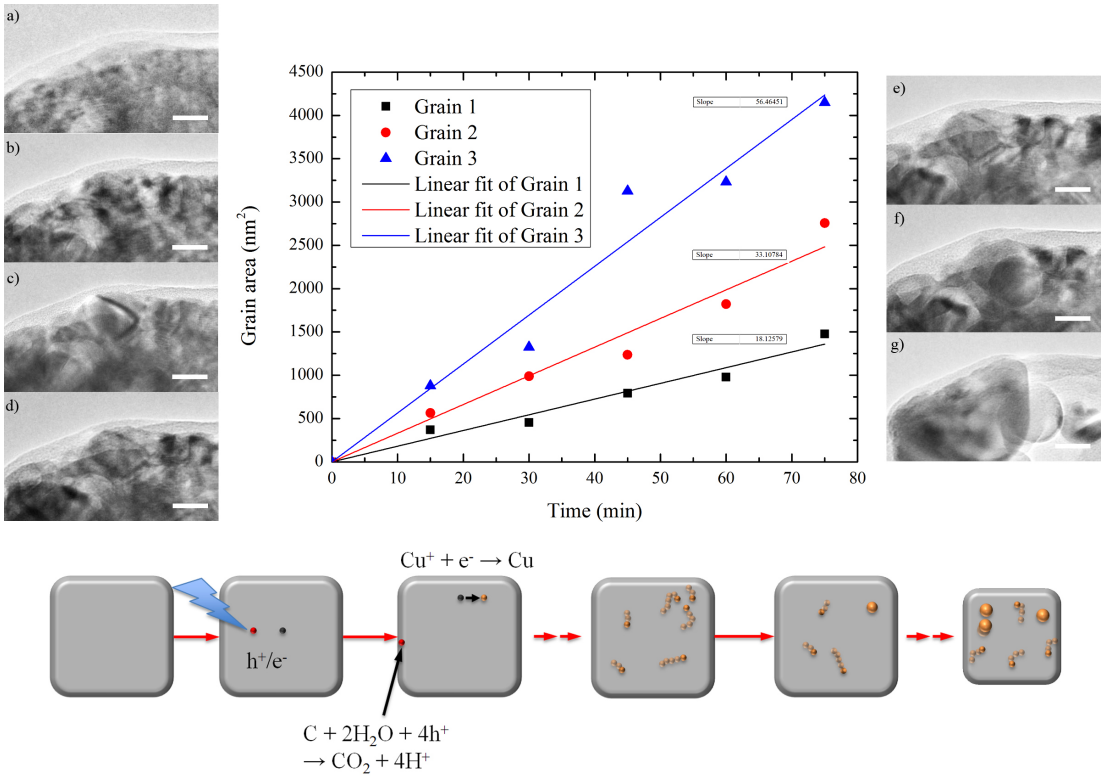

Figure 4.4: Grain growth - a-g) BF images of a selected area near the nanocube edge show a grain growth (scale bar 25nm). The plot shows measured area values relative to three distinct grains in different areas of the sample for each reaction step. A linear growth rate can be extrapolated from the grain size plot. A possible schematic model for the process is depicted in the diagram.

before performing further quantitative analysis (see Section 2.2.2). A negative power law function (AE^{-r}) was fitted to the pre-edge energy-loss signal and the background was subtracted to the core-loss spectrum. Low-loss spectra were acquired for the same region each time a core-loss spectrum was recorded. The low-loss signal was used to deconvolute the core-loss using the Fourier-ratio technique. Figure 4.5 shows two raw spectra acquired from the nanocube at reactions steps a) and f) in Figure 4.3. Comparison of the two spectra with reference data [90] allows identification of the chemical composition.

The oxidation state of copper is reflected in the Cu $L_{2,3}$ edge resulting in dramatic changes of its characteristic features [91, 92]. Energy-loss spectra from copper oxides show strong L_2 and L_3 ionization edges at 951 eV and 931 eV, respectively, known as "white lines" resulting from transitions from the 2p core level to the 3d states. In metallic copper, the 3d state is full. In the oxide form, electrons from Cu are donated to O resulting in vacancies in the 3d level giving rise to the sharp transitions [92, 93]. For metallic Cu (Cu^0) this effect is reflected in the spectra as a step-like abrupt onset with weak features in the energy-loss near edge structure (ELNES) region whereas the Cu edge in Cu_2O (Cu^+) and CuO (Cu^{2+}) appears as two peak-like white lines at the energy-losses mentioned above. The ELNES region of the copper edge is characteristic and can be used to distinguish the two most common oxide forms, Cu_2O and CuO, by the relative intensity of white lines [90]. No CuO phase was detected at any phase of reaction, indicating that a sacrificial agent was indeed present.

While direct observation of the Cu L-edge shape allows a qualitative assessment of the overall oxidation state of the sample, the co-existence of different phases at intermediate reaction steps evidenced by BF and diffraction data in Figure 4.3, indicates that the EELS signal from the entire nanocube consists of a superposition of both Cu and Cu_2O spectra. Multiple linear least square (MLLS) curve fitting and STEM-EELS techniques were used in order to achieve quantitative data on intermediate phases (see Section 2.2.2).

Two spectra were recorded from the sample at the beginning and at the end of the experiment (Figure 4.5A). These spectra were zero-loss deconvolved as described above and saved to serve as reference spectra for Cu_2O and Cu respectively after positive match with reference data [90]. Individual experimental spectra recorded at each time

frame during the reaction (Figure 4.5B) were fitted using an MLLS algorithm of the following type:

$$F(E) = AE^{-r} \sum B_n S_n(E) \tag{4.4}$$

Where AE^{-r} represents a pre-edge background interpolating function of the negative power low type, n is the number of spectra used in the linear combination, S_n represent the core-loss reference spectra for the element of interest and B_n are the weight coefficients for each component. The coefficients can be found by minimizing

$$S = \sum (S_n - y_n)^2 \tag{4.5}$$

The reference spectra as well as each individual spectrum recorded during reaction were normalized by setting the maximum intensity of each spectrum to 1. Thus the B_n coefficients fall in the range from 0 to 1 allowing for straight forward interpretation of the fitting results. In Figure 4.5C the results of this analysis are shown and the spectral composition determined from EELS for each time frame is given. Spectra can be described accurately as Cu_2O-like and Cu-like at the beginning and end of the reaction, respectively, while during reaction the spectral structure monotonically shifts from oxidic to metallic.

Acquisition of EELS spectra with a lower-dispersion allows for direct quantification of the Cu/O ratio in the sample using integration methods [31] (see Section 2.2.2). In Figure4.5B, EELS spectra including both the O and the Cu edge are shown for 3 representative reaction steps, i.e. after 15, 45 and 75 min. Besides a qualitative assessment of the relative intensity of the two edges, quantitative results are shown in Figure 4.5D in the form of an atomic-% plot as a function of time. The elemental concentration of Cu and O is calculated using integration methods for EELS spectrum quantification [82], showing a monotonic growth from Cu:O $\approx$ 60:40 to Cu:O $\approx$ 100:0 consistent with what is shown by diffraction and MLLS fitting results. The superfluous oxygen content in the first reaction steps from the theoretical Cu/O ratio for stoichiometric Cu_2O is explained by the presence of oxygen-rich contamination on the specimen.

The phenomenon of photodegradation can be followed in further detail by use of HAADF-STEM imaging and EELS. Although metallic nuclei are visible in diffraction contrast images as dark regions in Figure 4.3, HAADF-STEM and STEM-EELS provide an ideal means of local chemical characterization and can be used to investigate

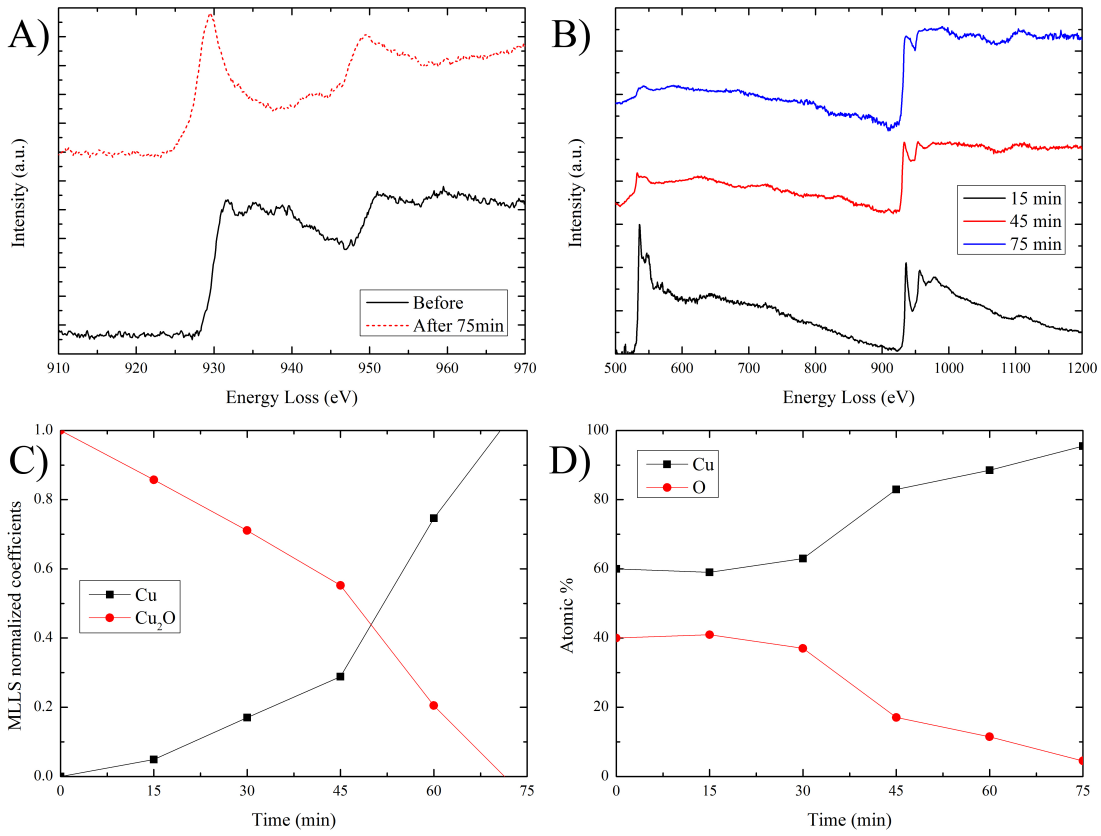

Figure 4.5: EELS quantification - MLLS EELS fitting results and EELS quantification of each step in the photocorrosion experiment. A) Cu-EELS spectra before and after reaction. B) Low dispersion EELS spectra including O and Cu edge, used for quantification. Only 3 representative spectra are shown for ease of visualization. C) MLLS normalized coefficients plotted over reaction time. D) Relative concentration of Cu and O as calculated by EELS quantification. All spectra are recorded in diffraction mode. Spectra in A-B) are background-subtracted and zero-loss deconvolved.

the phase of individual crystal grains. Due to their difference in density, Cu_2O and Cu are readily distinguishable by HAADF-STEM: Cu has a density of 8.96 g/cm^3 while Cu_2O has a density of 6.0 g/cm^3 which is sufficient to distinguish the two compounds using Z-contrast in HAADF imaging.
STEM-EELS was used to characterize individual crystal grains in the sample. In Figure 4.6, STEM-EELS spectra are shown for two separate areas of the same nanocube, indicating the presence of segregated Cu portions in the Cu_2O nanocube bulk. This analysis further confirms the nucleation mechanism proposed.
Bright-field imaging, electron diffraction and electron energy-loss spectroscopy were used to elucidate the photoreduction of cuprous oxide in aqueous environment under light illumination. A time-resolved systematic analysis of the light-activated reaction shows the progressive reduction of Cu_2O into Cu, giving insight into the reaction mechanisms. Polycrystalline cuprous oxide particles are suggested to be reduced via an atom-by-atom mechanism. The presence of a sacrificial carbon source allows the reaction to take place at a high rate. A reaction rate was assessed for the nucleation reaction based on ETEM observations, and the photocatalyst degradation trend was followed using EELS analysis.
The use of a TEM specimen holder for light activation was crucial for achieving a time resolved study of photocatalyst deactivation. These types of experiments will have a great impact on the study and development of light sensitive materials and photocatalysts in particular.

4.2 Pt photodeposition

GaN:ZnO is one of the most promising photocatalysts for overall water splitting [94,95]. Its activity is strongly dependent on the type of co-catalyst loaded (see section 2.1.1). Pt is one common co-catalysts for the hydrogen evolution reaction (HER) on the semiconductor surface, provided that a protective layer such as Cr_2O_3 is present to prevent back reactions [96]. Photodeposition is a desirable preparation method as it gives homogeneous and reliable particle distribution, it is simple and inexpensive. The procedure to photodeposit Pt described by Silva et al. [97] was modified in order to perform it in the TEM. Commonly, the semiconductor used as a deposition substrate is stirred in acqueous ethanol or methanol solution containing the Pt precursor —in this case

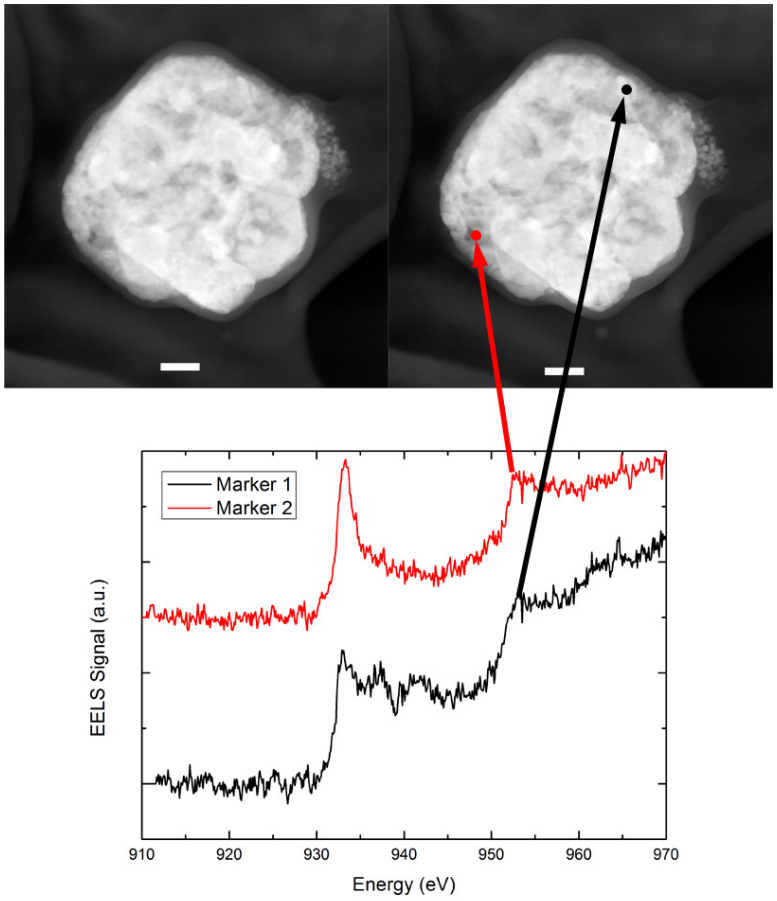

Figure 4.6: STEM-EELS - STEM-HAADF images of the same Cu_2O nanocube shown in Figure 1, at different times. The images show how reduced crystals nucleate and grow within the particle body. STEM-EELS on the marked positions is used to investigate the chemical phase of individual grains. The plot shows that a predominantly reduced phase at position 1 and an oxidized phase at position 2 coexist in the particle after 45 min exposure.

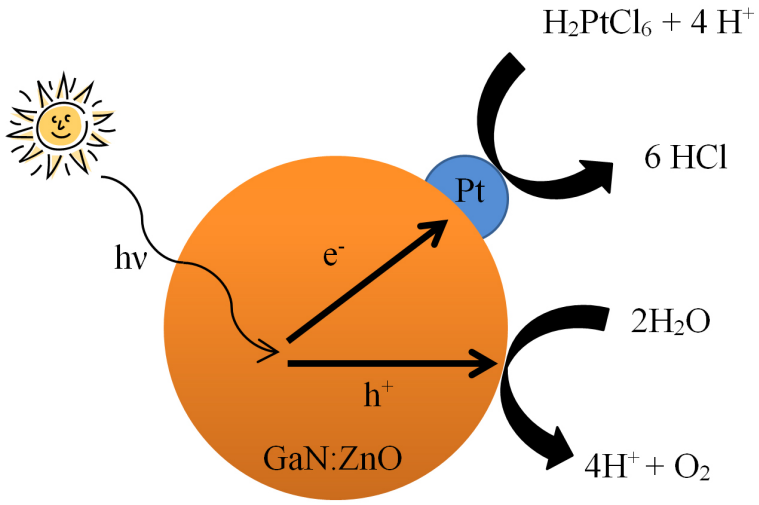

Figure 4.7: Co-catalyst photodeposition - Schematic sketch of the Pt photodeposition process. Light generates an electron-hole pair in the GaN:ZnO photocatalyst. Electrons and holes migrate to the surface and activate reactions with the surrounding chemical species. The electrons are responsible for the Pt precursor decomposition, while the holes drive the water oxidation reaction.

H_2PtCl_6— and illuminated for several hours with a UV lamp (see Figure 4.7). Unfortunately, liquid phase reactions in the TEM require special conditions and equipment such as dedicated liquid-enabled specimen holders [39] (see Section 2.3) which were not available. However, the deposition method was modified so that the H_2PtCl_6 precursor was evaporated gently onto the GaN:ZnO surface (to avoid thermal decomposition). The as-prepared powder was deposited onto a gold TEM grid covered with an amorphous carbon film and inserted into the microscope. TEM investigations were carried out using the fiber-based holder (see Section 3.1). Preliminary control experiments were carried out to distinguish effects other than that of light (see Table 4.1). None of the experiments resulted in changes to the sample, while the Pt deposited rapidly in the electron beam in the presence of water vapour. These tests allow designing experiments in which the role of electrons can be neglected.

After a preliminary inspection of the sample, the electron beam was blanked (column valves closed), water vapour was leaked into the specimen chamber at a pressure of 5mbar and the sample was exposed to light at λ=405 nm with an intensity of 6 W/cm^{-2} over the entire grid for 4 hours. The light was then turned off and the specimen chamber was evacuated for 5 hours before analysis. The results are shown in

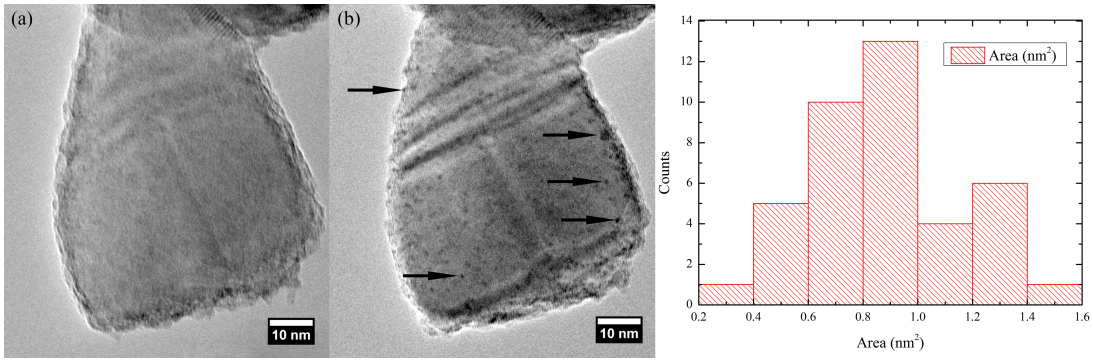

Figure 4.8: Pt photodeposition - Bright-field TEM images of a GaN:ZnO particle (a) before and (b) after reaction in 5 mbar H_2O and with 6 W/cm2 light at 405 nm wavelength. The two images were acquired in vacuum and the reaction was carried out in the absence of the electron beam. The arrows in (b) show some of the deposited Pt nanoparticles. The histogram shows the particle size distribution upon photodeposition. Particles with a diameter size of approximately 1nm are predominant in the sample.

Figure 4.8.

The amorphous precursor disappears after irradiation, while ∼1nm nanoparticles are formed on the surface of the photocatalyst. Particles are identified as Pt by means of EDX analysis. The size distribution shown in Figure 4.8 indicates that particles are relatively small, which together with the high homogeneity makes for an excellent photocatalytic system due to the high surface area. Activity of this system was reported by Maeda et al. [96], showing that Pt works as a co-catalyst only as long as a Cr_2O_3 shell is deposited onto it to reduce the back reactions. The encapsulation of Pt is treated in more detail in Chapter 5

4.3 MoS_2 photodeposition

The importance of bandgap engineering by the application of appropriate co-catalysts for photocatalyst optimization was shown in Section 2.1.1, and more specifically GaN:ZnO modification with Pt was studied in Section 4.2. Although platinum is the archetypical catalyst for HER, it is scarce and expensive, which stresses the need for cheap and earth abundant materials taking its place [98]. MoS_2 is developing growing interest in the photocatalysis community being an inexpensive and working co-catalyst for HER [99]. MoS_2 in the form of incomplete cubane-type electrocatalyst [100] and

Si-supported MoS_2 systems [101] were reported stable working systems for this reaction. Modification of GaN:ZnO with MoS_2 was considered as a novel viable option and was first attempted *ex situ*. GaN:ZnO loaded with photodeposited MoS_2 was tested in micro reactors [102] and found inactive. The photodeposition procedure was therefore investigated *in situ* in order to elucidate the causes of failure and optimize the process where possible.

An $(NH_4)_2(MoS_4)$ precursor was added to an acqueous suspension of GaN:ZnO and kept in darkness under inert Ar atmosphere in order to avoid decomposition in air. A drop of suspension was deposited on a lacey carbon-coated Au grid and left to dry in darkness on filter paper. Once dry, the grid was cut with a scalpel and inserted in the holder. The sample was investigated under vacuum, then the column valves were closed and the sample was exposed to water vapour at a pressure of 4mbar, λ=405nm light irradiation at 6W/cm^2 for 1 hour, in absence of the electron beam. The column was evacuated to a pressure of $\sim 10^{-5}$mbar and light was turned off prior to inspection. Figure 4.9 shows the experimental results.

The precursor salt can be distinguished by its brighter contrast and amorphous structure. In Figure 4.9b the amorphous layer appears reduced in volume and exhibits a slightly smoother amorphous contrast. This layer is thought to be an oxidic Mo form (MoO_x) produced by decomposition of the precursor by the photogenerated holes. The precursor is expected to oxidize rapidly in air, so the exposure during TEM grid preparation could cause part of the precursor to oxidize. During earlier experiments when the sample was not protected in Ar atmosphere during transfer, no deposition was observed after exposures as long as 5 hours under the same light and vapour conditions. Moreover, $\sim$0.58nm-spaced black-white fringes can be noticed within the precursor matrix, generally parallel to the GaN:ZnO particle surface. These fringes are characteristic of lamellar MoS_2 viewed along a folding edge, where the (002) planes are parallel to the electron beam. Comparison between experimental data and simulation is shown in Figure 4.9c-d. Construction of the MoS_2 supercell was carried out using the Rhodius platform (©2005 University of Cádiz), while JEMS software was used for multislice image simulation. Comparison of experimental and simulated data allows identification of the MoS_2 phase from the amorphous matrix. Fringes in Figure 4.9c are more wiggly than those simulated, due to local bending perpendicular to the viewing direction ([010] zone axis). An amorphous layer above and below the MoS_2 stack was simulated

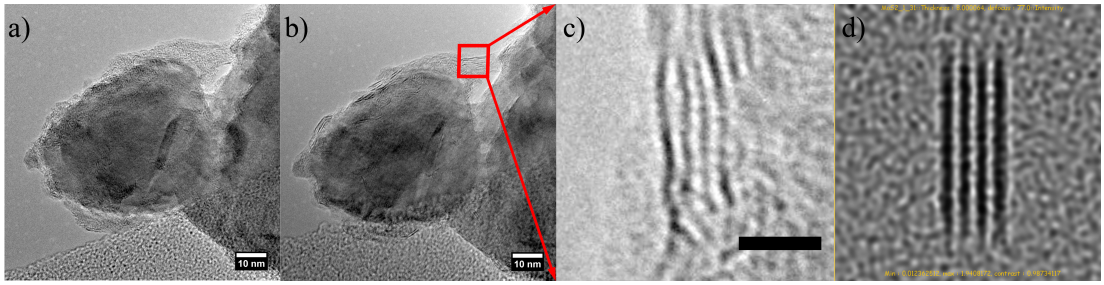

Figure 4.9: MoS_2 photodeposition - TEM bright field images of a GaN:ZnO particle before a) and after b) *in situ* photodeposition of MoS_2. The Mo precursor is visible on the left as an amorphous matrix surrounding the GaN:ZnO particle. b) The crystallized MoS_2 phase separates from the amorphous matrix and becomes visible, exhibiting the characteristic black-white fringe contrast with a lattice spacing of about 0.58nm, corresponding to the (002) spacing. c) Extracted 10x10nm^2 area from frame b) where a stack of MoS_2 platelets is clearly visible embedded in the remaining precursor (scale bar 3nm). d) Simulated BF image of a 4-layered MoS_2 stack on amorphous carbon substrate. The intra-planar spacings and contrast appear matching with those shown in c).

to account for the oxide matrix.

This *in situ* investigation suggests that a large fraction of the precursor decomposes into an amorphous oxide on the semiconductor surface after photodeposition, actively shielding the photocatalyst surface and MoS_2 platelets from the reaction environment. This explains the poor performance of the material. The deposition protocol could be modified to account for the oxidized precursor, however this TEM study cannot determine whether washing the oxide would remove the MoS_2 phase too. Attempts in this direction are currently under investigation.

4.4 Ru photodeposition

Ru is considered a novel co-catalyst for enhancing performance of GaN:ZnO. Although Ru and RuO_2 are known co-catalysts for water splitting [103,104], no attempt has been made so far for its application on this semiconductor photocatalyst, therefore characterization of this novel system is of interest for material optimization. Ru in the metallic form is active for the HER [103], while RuO_2 is a catalyst for the OER [105]. $RuCl_3$, used as Ru precursor on GaN:ZnO, is supposed to be reduced to metallic Ru by the photogenerated electrons and oxidized to RuO_2 by the holes upon light irradiation of the system, thus resulting in mixed photodeposited Ru phases. The challenge is how to selectively deposit only one phase (Ru or RuO_2). The use of organic charge scavengers

for altering photodeposition results is known in literature [106]. Benzaldehyde should act as an electron scavenger in the photodeposition process, therefore the addition of this compound to the precursor before photodeposition is thought to cause preferential oxidic RuO_2 deposition over metallic Ru. In other words, the presence of benzaldehyde should favor $RuCl_3$ to decompose in the oxide form (RuO_2) while the absence of it should lead to an uncontrolled mixed metallic and oxidic Ru deposition. Following the photodeposition process *in situ* and comparing the two systems —with and without benzaldehyde— allows the verification of the hole scavenging effect and the preferential deposition.

GaN:ZnO powder was suspended in acqueous solution with 1% $RuCl_3$. A first sample was kept in this condition, while benzaldehyde was added to a second sample. A drop of suspension was dispersed on a lacey carbon-coated Au grid and left to dry in darkness on filter paper. Preliminary TEM inspection was performed in vacuum prior to photodeposition. Afterwards, the samples were exposed to water vapour at a pressure of $\sim$3mbar and light stimulation at λ=405nm and 6W/cm^2 for 1 hour. The microscope was evacuated to a pressure of $<10^{-5}$mbar and light was turned off before new data were acquired.

BF imaging was used to assess morphology changes in the sample. Figure 4.10 shows the comparison of the photodeposition effects on the sample with and without benzaldehyde. No visible particle formation occurs in either case. On the contrary, the few darker globe-like features present in the loaded sample in frames (a-c) disappear in (b-d), leaving the place to a more homogeneous amorphous layer.

STEM-EELS was used to identify the composition of the outer layer (see Figure 4.11), allowing distinction of the oxygen signal coming from either the deposited layer or the bulk, which contains oxygen too. Simultaneous acquisition of EDX spectra confirms the presence of Ru in the sample. The EELS Ru-$M_{2,3}$ and the O-K edges were analyzed for each deposition condition. The relative intensity of the O-K and Ru-M_3 edges indicates a higher O content in the sample with benzaldehyde, as opposed to the sample without benzaldehyde which exhibits a higher Ru-$M_{2,3}$ intensity versus that of the O-K edge. The Ru-$M_{2,3}$ signal was more challenging to acquire in the case shown in Figure 4.11b, resulting in a considerably lower S/N ratio, making analysis more complicated, therefore further experiments should be planned to give full insight in the deposits composition. However, a first assessment of the deposition can be made on the basis of

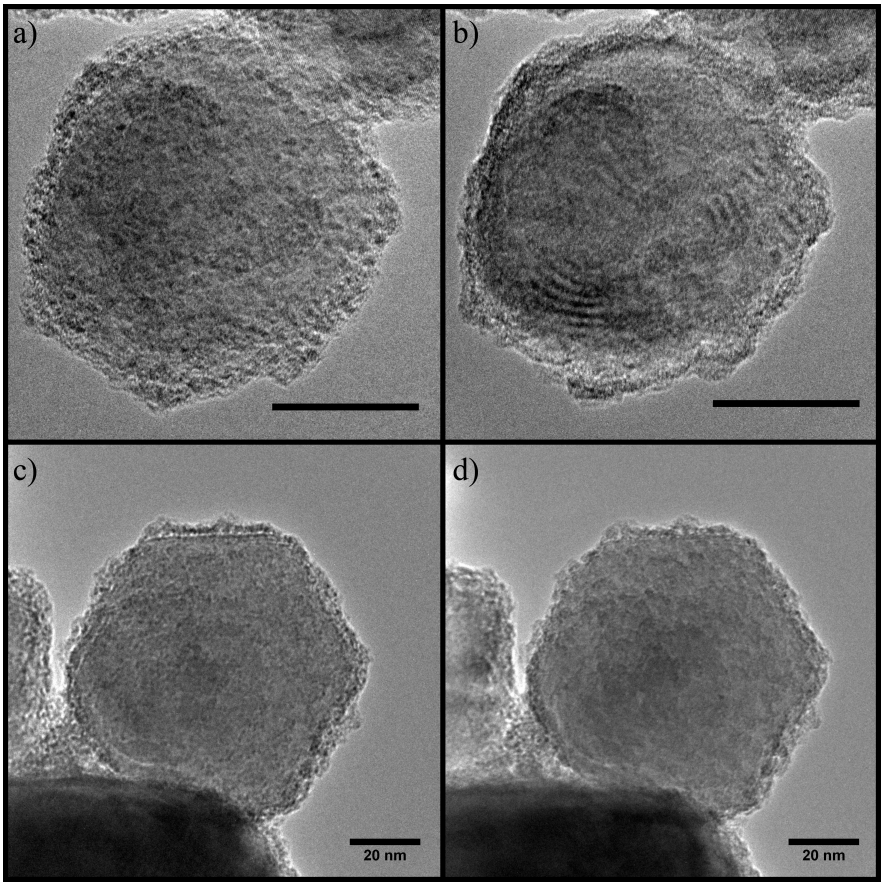

Figure 4.10: Ru photodeposition - Ru-covered GaN:ZnO photocatalyst. Before (a) and after photodeposition (b) with benzaldehyde. Before (c) and after photodeposition (d) without benzaldehyde. Scale bars are all 20nm.

this data. In presence of benzaldehyde Ru is deposited in an oxidic form (RuO_x), while a more metallic deposit is present in the sample without scavenger. This result gives an optimistic feedback for the selective deposition of Ru phases on a semiconductor substrate, and in particular for the selective oxidic deposition on GaN:ZnO in presence of benzaldehyde. Further experiments with other scavenger types (such as ethanol as a hole scavenger) should be carried out. Batch production of samples is underway for *ex situ* catalytic testing in µ-reactors.

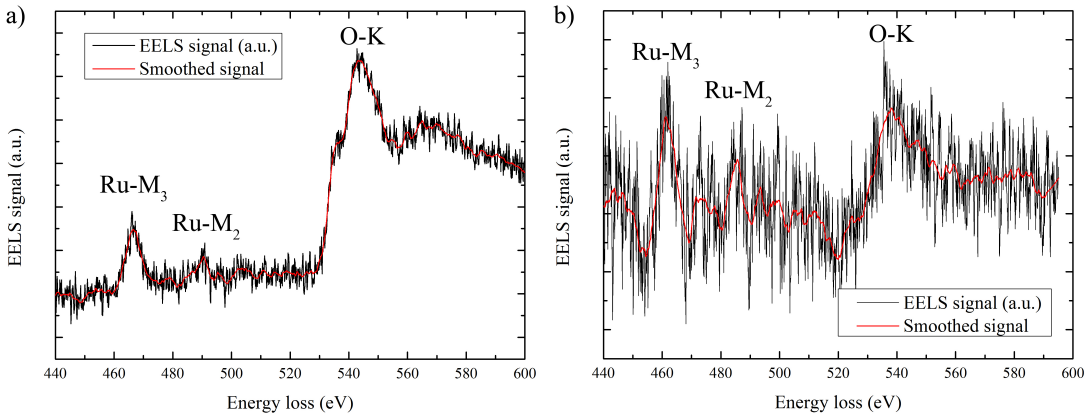

Figure 4.11: EELS on Ru edge - STEM-EELS spectra of the outer layer covering GaN:ZnO after photodeposition. a) With benzaldehyde b) without benzaldehyde. The Ru-$M_{2,3}$ and the O-K edge are marked. The relative intensity of the Ru and O edges suggests that a higher O content is present in a), consistently with what expected.

4.5 TiO_2 photocatalytic self-cleaning from hydrocarbons

Titania is one of the most widely used photoactive materials on earth, employed in a variety of fields from composite materials to varnishes, from sunscreen to solar cells. TiO_2 is an inexpensive material with remarkable photocatalytic properties, as suggested for the first time by Fujishima and Honda [15, 16]. Titania is commonly found in the rutile and anatase phases, with a bandgap of 3.0eV and 3.2eV, respectively [107, 108]. Brookite phase is stable only at low temperatures and is therefore considered less useful practically. Unfortunately, the solar irradiance spectrum on earth overlaps poorly with this bandgap due to the strong ultraviolet (UV) absorption in the ozone layer of the atmosphere (see [109] for reference spectra). As a consequence, it is difficult to use titania for high-yield photocatalytic processes but the abundance of this material maintains it a good choice for, e.g., photocatalytic self-cleaning of surfaces [110]. This phenomenon can be investigated by means of HRTEM, as shown previously by Yoshida and coworkers [72, 73] using a modified TEM which allows light irradiation through an optical port in the column. Here, an analogous study using the dedicated light illumination holder shown in Section 3.1 is shown. TiO_2 self-cleaning is in fact known to be primarily due to the formation of highly reactive hydroxyl groups [110] that in turn etch the hydrocarbons away. A TiO_2 anatase powder coated with a thin layer of carbonaceous materials was prepared and dispersed on a gold TEM grid with lacey

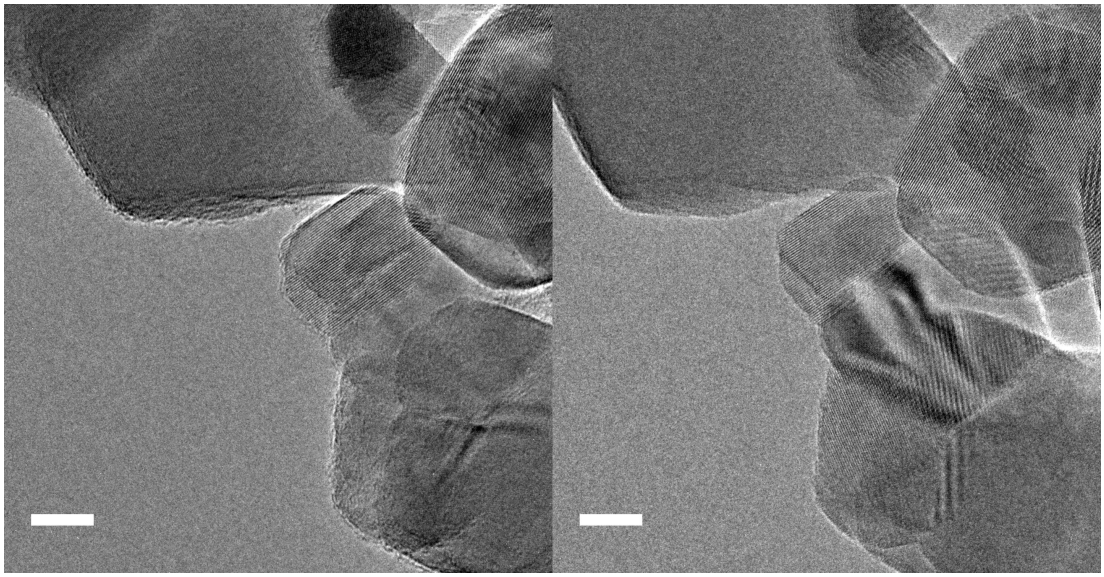

Figure 4.12: TiO_2 photocatalytic self-cleaning - TEM bright field images of TiO_2 particles before and after *in situ* illumination with λ=365nm light for 1h in presence of 3mbar water vapour. An amorphous layer is visible in (a), while after 1 hour exposure the substrate appears clean (b). Scale bar 10nm.

carbon film. The sample was exposed to 3mbar water vapour and λ=365nm light at 100mW/cm^2 for 1 hour, in absence of the electron beam. After the microscope was evacuated to a pressure of $<10^{-5}$mbar, the sample was investigated and the changes on the surface were observed. In Figure 4.12 the effect of light irradiation is visible in the reduction of the carbonaceous amorphous layer covering the titania particles.
The advantage of using the holder system in an ETEM is that the sample can be exposed to water vapour and thus monitored under simulated working conditions.

5

Pt nanoparticle encapsulation on $SrTiO_3$

$SrTiO_3$ (STO) is often used as a model photocatalyst for hydrogen evolution from photocatalytic water splitting when doped [111] or loaded with a suitable co-catalyst [112,113]. Although STO matches the bandgap position requirement (see section 2.1.1), the wide bandgap (3.3eV) [114] of this catalyst results in a less than 5% of sunlight absorption and low evolution efficiency. A number of attempts has been made for predicting and optimizing the performance of such systems using appropriate co-catalysts and preparation methods [115]. Even though platinum is one of the most common co-catalysts for hydrogen evolution on many semiconductor photocatalysts [22], the overall photocatalytic activity of systems loaded with Pt is hindered by the fact that Pt also efficiently catalyzes the water recombination reaction, which is also referred to as the "back reaction". The equilibrium of the overall reaction is thus to the left hand side of the equation, if we represent it as follows

$$2\,H_2O \rightleftharpoons 2\,H_2 + O_2 \tag{5.1}$$

Strong metal-support interaction (SMSI) causes drastic changes in chemisorption properties of supported active metallic components in catalytic systems [36]. Encapsulation is a form of SMSI that has been reported to improve selectivity of catalysts [116, 117] and photocatalysts [118]. With regards to photocatalytic water splitting, Maeda and co-workers prepared a GaN:ZnO photocatalyst loaded with a transition metal (Rh, Pd, Pt) or metal oxide core and a Cr_2O_3 shell which enhanced the overall water splitting

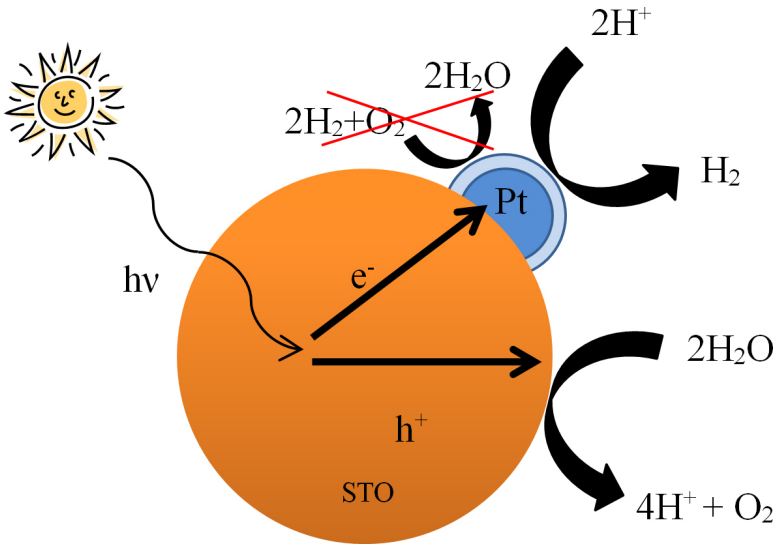

Figure 5.1: Core-shell - Schematic representation of the working principle of the core-shell system for photocatalytic water splitting performance enhancement. The shell is semi-permeable, allowing diffusion of H_2 and H^+ species but impeding diffusion of O_2. Therefore the core particle cab perform the direct hydrogen reduction but is prevented from doing the back reaction.

efficiency of the material [96]. The working principle of such system is the formation of a semi-permeable shell over the co-catalyst, which reduces the reverse reaction by forming an oxygen barrier (see Figure 5.1). If oxygen cannot reach the co-catalyst, no water recombination can occur and the net photocatalytic water splitting activity is increased.

The encapsulation method is of interest for the development of more efficient photocatalysts, and its application to other semiconductor photocatalysts deserves investigation. Encapsulation and decoration of metallic nanoparticles on oxide substrates upon high-temperature reduction has been extensively investigated [36,119–122] and, in particular, the decoration of supported nanoparticles with species coming from the substrate has been reported on TiO_2 [123, 124].

Here, the encapsulation of STO-supported Pt particles is studied in order to enhance the water splitting performance of this material, with the particular goal of reducing the back reaction. *In situ* ETEM studies provided insight in the decoration mechanisms and thereby allowed optimization of the procedure.

Initially, Sigma-Aldrich® STO was mixed with H_2PtCl_6 in water and dried on a water bath at 100°C under gentle stirring. The dried product was collected and reduced at

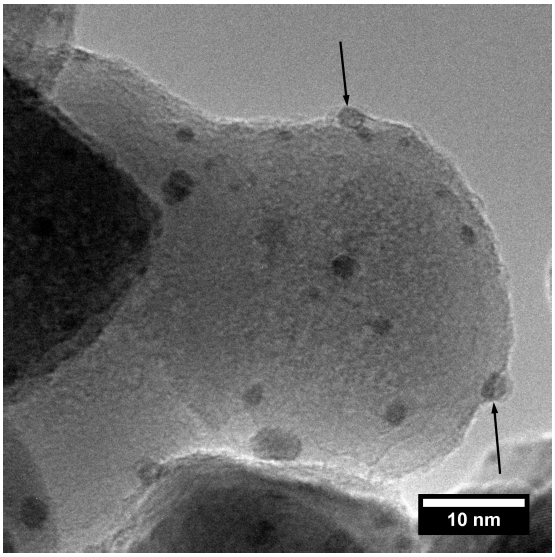

Figure 5.2: $SrTiO_3$ after reduction at 500°C in H_2 - Bright field image of the treated sample, showing partial decoration.

500°C in H_2. Testing of the photocatalytic water splitting performance of the treated material was performed in µ-reactors. Results indicated that the back reaction activity decreased after treatment with respect to the activity of the as-made sample. TEM investigation of the reduced sample (Figure 5.2) showed that Pt particles were only partly covered by an amorphous phase, the decoration being inconsistent on different particles. Assuming that the decoration is actually impermeable to O_2 (this data does not allow this to be verified), the uncovered portion of Pt provides enough active sites to achieve full conversion. This suggests that the reaction is still limited by diffusion. Therefore, Pt must be entirely unexposed to the reaction environment in order for the back reaction to be efficiently reduced. If the shell is permeable to O_2 the system performs exactly as well as prior to treatment. The partial decoration is in agreement with what is shown in literature [123–125]. The encapsulation procedure was performed *in situ* in the ETEM in order to elucidate the decoration mechanisms and suggest options for optimization.

Pt-loaded STO powder was dispersed on a Au TEM grid without carbon film and inserted in an Inconel® double tilt heating holder (Model 652 from Gatan®). The ETEM was operated at 300kV accelerating voltage in TEM mode. The sample was inspected in high vacuum ($\sim 10^{-7}$mbar) prior to reaction. A 1.3mbar H_2 gas atmosphere

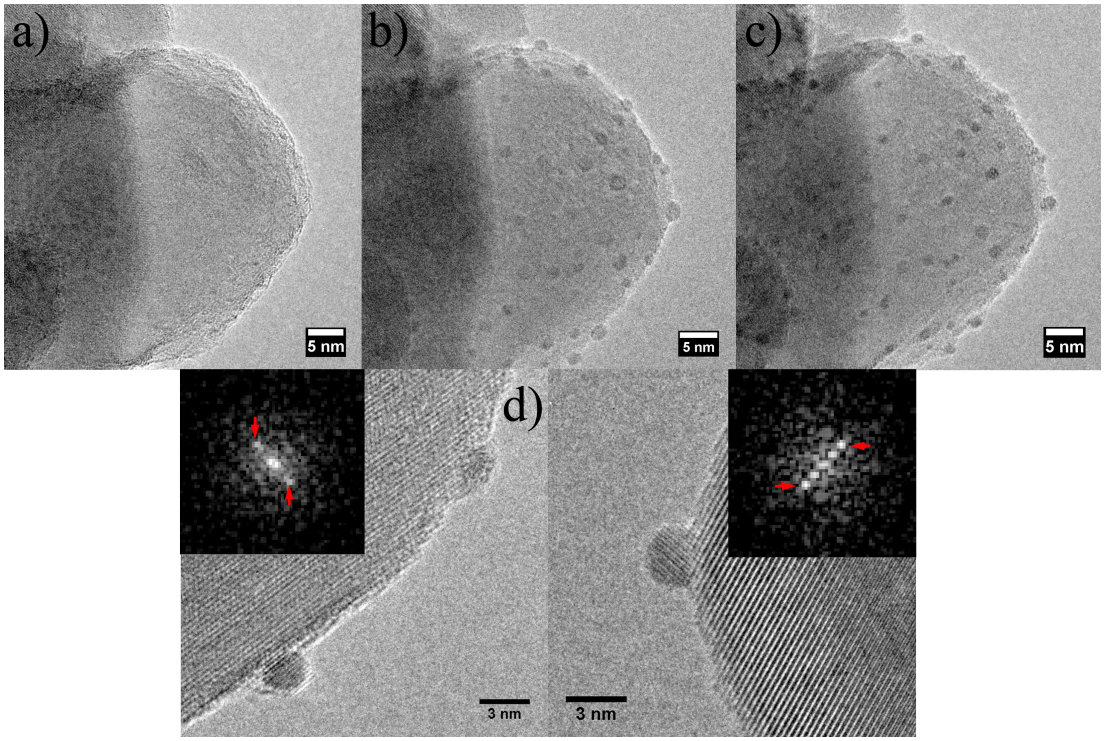

Figure 5.3: *In situ* encapsulation - TEM bright field images of $SrTiO_3$-supported Pt nanoparticles before (a), during (b) and after (c) *in situ* treatment with H_2 at 500C. a) The substrate surface is almost featureless and shows few small supported dark clusters. b) During heating at 500°C in 1.3mbar H_2 dark particles form c) Sample after cooldown to room temperature. d) Supported Pt nanoparticles after treatment and respective digital diffractograms highlighting the 200 reflection, corresponding to the 1.98Å spacing in Pt.

was introduced around the specimen, and the sample was gradually heated to 500°C and left stabilizing until the thermal drift ceased before acquiring images. Results are shown in Figure 5.3.

Before heating, the STO substrate is nearly featureless, showing almost no supported Pt particles and a corrugated surface (Figure 5.3a). At 500°C in 1.3mbar H_2, dark particles are clearly visible on the STO surface (see Figure 5.3b) while the surface itself appears smoother. Such particles are identified as Pt by analysis of the associated fast Fourier transformations (FFTs) (see Figure 5.3d). This suggests that Pt is present from the beginning probably in solid solution within the substrate, while at high temperature in H_2 Pt particle formation becomes favourable. No shell formation is observed at this temperature, but particles are extremely mobile under the beam and move around quickly reconstructing the STO surface. The sample was left at high temperature for 1

hour while imaging, then it was cooled down to room temperature maintaining the H_2 atmosphere at an average rate of ∼50°C/min. Imaging was performed during cooldown while compensating for the thermal drift of the sample. During the cooling phase, part of the substrate appears to migrate onto the particles, as confirmed by the images taken after temperature stabilization (Figure 5.3c). An amorphous phase decoration is noticeable only on some particles, while others appear clean or partly covered. The amorphous phase often assumes the shape of a "volcano", on top of which a Pt particle is located —uncovered on the opposite side. This morphology suggests surface diffusion and rearrangement of species coming from the substrate around the Pt crystallites during the cooling phase. Metallic particles can locally rearrange the substrate at high temperatures in reducing environments, in particular facilitating the reduction of titania [126], so the accumulation of amorphous phase next to Pt clusters could be the result of a preferential local reduction in their vicinity. A hydrogen spillover mechanism over Pt into the substrate is therefore suggested. The particle activity observed during cooldown may eventually be quenched at room temperature. The beam effect makes assessment of the quenching temperature range challenging. After formation at high temperature, Pt particles are stable at RT, suggesting that the slight increase in overall activity accompanied by an increase in the back reactions shown in Figure 5.2a, could be an effect of the increased Pt surface area. However, particle encapsulation and subsequent overlayer stabilization was observed exclusively during the cooldown phase. A comparison of different cooling ramps was attempted both *in situ* and *ex situ*, leading to comparable results. Slower cooling ramps (∼10°C/min) led to more consistently decorated Pt particles, but still showing incomplete and uneven encapsulation.

In the attempt of investigating the reduction effects at different temperatures, another thermal treatment in H_2 was done at 700°C. *In situ* investigation of the particle state at high temperature shows no evidence of stable particle decoration, however particles are observed to move and rearrange the substrate at a higher speed than previously observed at 500°C. The electron beam effect was estimated by varying the electron dose. High electron doses severely affect the dynamic behaviour of particles, which appear more mobile under an intense beam. After inspection at high temperature the sample was brought to room temperature and the microscope was evacuated to a pressure of $\sim 10^{-6}$mbar. HRTEM images were acquired in these conditions (Figure 5.4).

Approximately 50% of the Pt particles were decorated with some form of amorphous

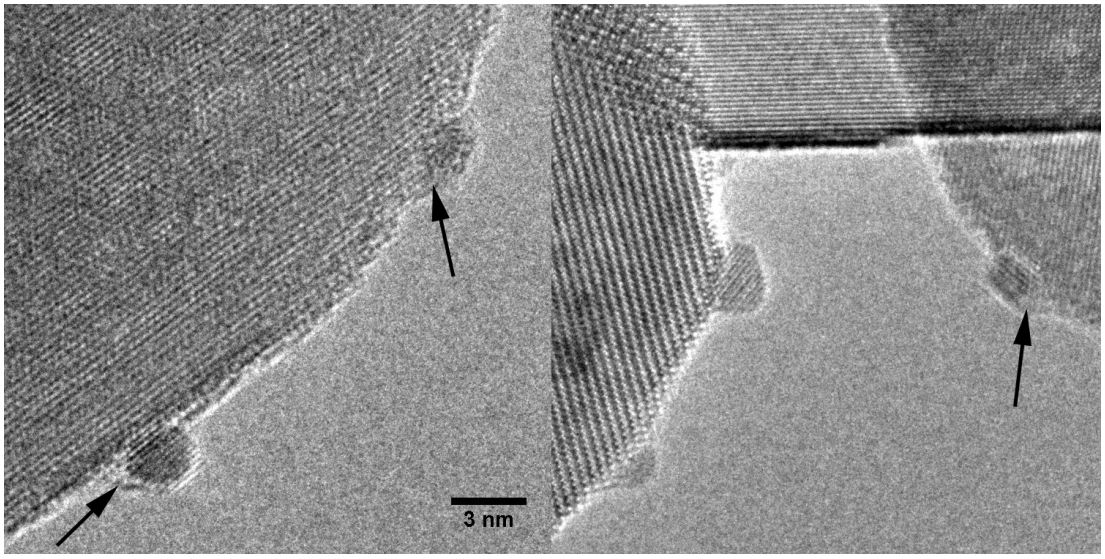

Figure 5.4: *In situ* H_2 reduction - TEM bright field images of Pt particles formed after *in situ* treatment in 1.3mbar H_2 at 700°C. Amorphous deposits are indicated by black arrows.

phase, of which ∼30% was only partly encapsulated (Figure 5.4). The partial encapsulation is particularly noticeable on larger particles, probably owing to the larger diffusion length needed for the substrate species to encompass large crystallites.
The effect of SMSI reversibility [116] was investigated *in situ* by reoxidation of the reduced sample in O_2 at 500°C. The same sample reduced at 700°C was brought to 500°C in 3mbar O_2 and stabilized for 1 hour. Imaging at high temperature showed that particles were mostly uncovered, in a similar state than that observed at 500°C in 1.3mbar H_2. However, the beam effect in O_2 atmosphere was noticeable, as particles seemed uncovering rapidly after being illuminated with the beam. Etching can be caused by the formation of oxygen radicals in the beam. Direct observation of the local SMSI state in this condition was therefore deemed unreliable. Analysis was performed after cooldown to room temperature. All particles in the sample were found evenly covered with a 0.5-1nm thick amorphous layer that appeared covering the entire specimen (see Figure 5.5). Pt crystallites that were partly or not homogeneously covered after reduction in H_2 were found evenly covered. This behaviour could not be clarified until the same result could be reproduced *ex situ*, tested, and a more detailed investigation could be performed. Interestingly, a sample treated directly in O_2 at 500°C did not present Pt particle formation and therefore no encapsulation effect was identified. This

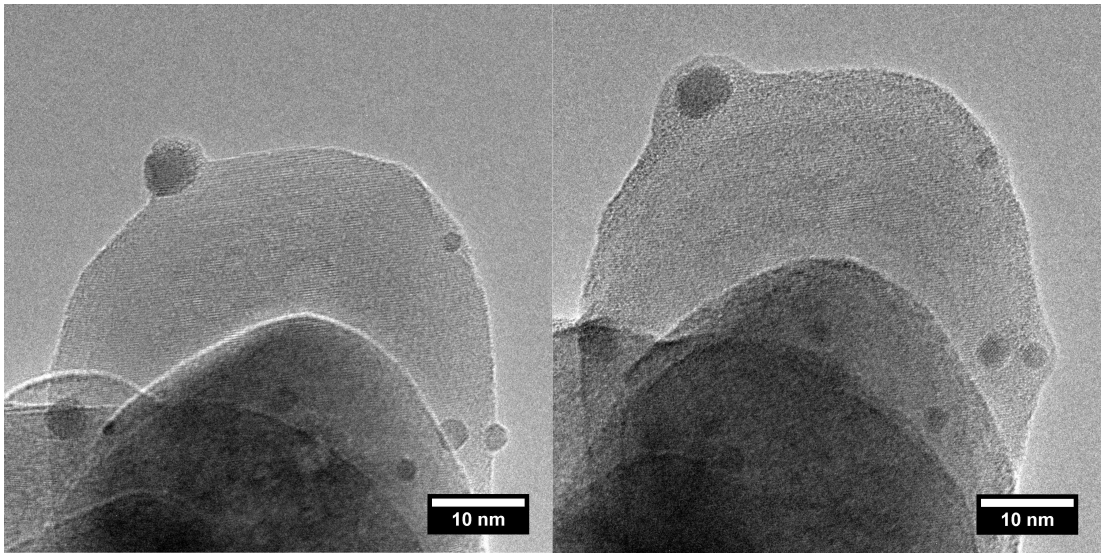

Figure 5.5: *In situ* encapsulation - TEM bright field images of $SrTiO_3$-supported Pt nanoparticles before and after *in situ* treatment in 1.3mbar H_2 at 700°C and subsequent treatment in 3mbar O_2 at 500°C

suggests that the sample needs a reduction phase in order for the SMSI effect to take place.

The Pt-loaded STO powder was reduced in H_2 at 700°C in an oven, then it was brought to room temperature and calcined at 500°C in air. The produced sample was tested in µ-reactors for the back reaction and for the overall water splitting reaction. A second sample was treated *in situ* in the µ-reactor in order to rule out the effect of air on the *ex situ* treated samples. µ-reactors are made of Si and pyrex glass, therefore operating temperatures must be kept below temperatures at which pyrex starts softening (approx 400°C). For this reason, the relevant temperatures for the treatment could not be reached and the sample was reduced only at 400°C in H_2 followed by a calcination in O_2 at 400°C. Results are summarized in Figure 5.6.

For the first 2 hours in flowing H_2 and O_2, no significant water signal was detected and the H_2 and O_2 signals remained roughly steady. This indicates that little consumption of H_2 and O_2 was taking place, i.e. in this phase the back reaction activity was very low. When the UV lamp was turned on after 2 hours of testing, a high CO_2 signal was detected, corresponding to a decrease in the H_2 and O_2 signal and an increase in the water signal. The CO_2 production is interpreted as oxidative self-cleaning of residual hydrocarbons that are always present from air contamination. Although back reactions

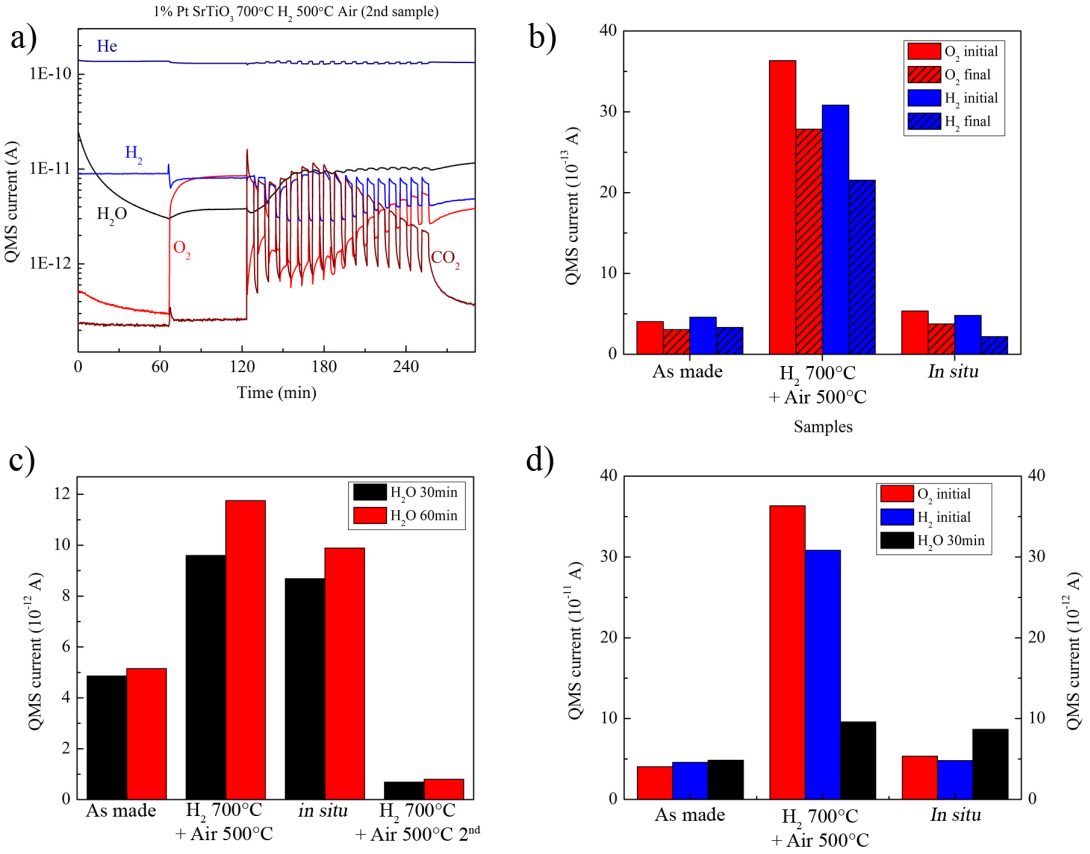

Figure 5.6: Mass spectrometer data - Quadrupole mass spectrometer (QMS) data comparing back and forward reaction performance of samples after different treatments. a) Raw QMS data of the back reaction test. b) Quantification of overall water splitting reaction. c) Quantification of back reaction performance. d) Summarized net activity and back reaction activity of all samples.

are restored after light is shone on the sample, Figure 5.6d shows that the net activity is greatly improved from the as-made sample. A significant reduction of the back reaction performance was successfully obtained before light illumination. This proves that the encapsulation has a beneficial effect, but is unstable under light illumination. Sample characterization was performed in order to elucidate the composition of the shell.

The *ex situ* calcined sample was investigated in a probe-corrected Titan 80-300 operated at 120kV accelerating voltage in STEM mode. The use of a lower acceleration voltage than that used for the ETEM experiments helped minimizing the beam damage during analysis. STEM-EELS was performed at dispersions of 0.2 or 0.1eV/channel. EELS is sensitive to the oxidation state of Ti [127, 128] (see Figure 5.7) and was used

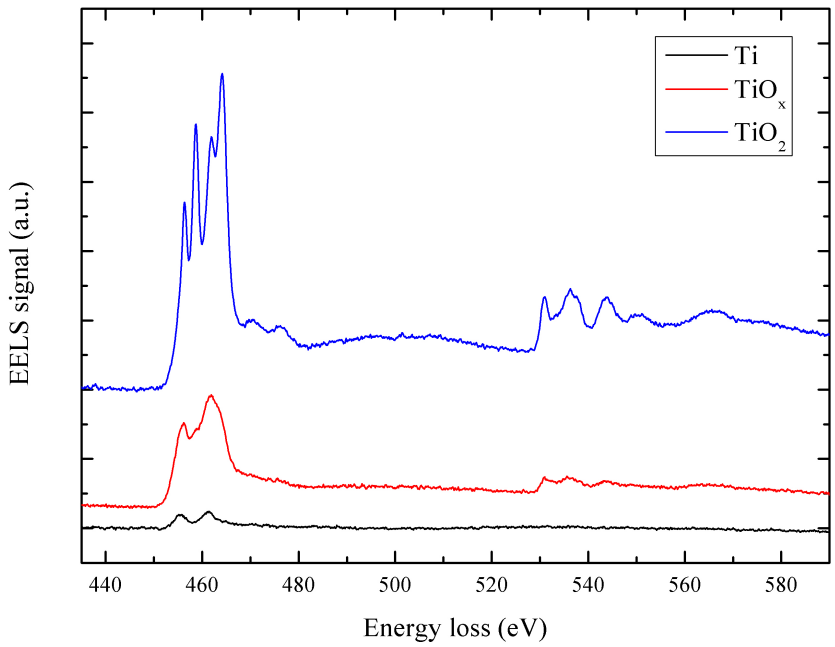

Figure 5.7: Ti-L and O-K EELS edges - The oxidation state-dependent Ti-L edge shape is shown for 3 representative conditions acquired on the Pt/STO sample. Ti^{4+} in TiO_2 (red curve) presents 4 characteristic sub-peaks due to the crystal field splitting (see text), as opposed to metallic Ti^0, which presents only the two Ti-$L_{2,3}$ major peaks. Intermediate phases (indicated generically as TiO_x) can be identified from the shape of the Ti-L edge together with intensity and shape of the O-K edge to support the observations.

to investigate the composition of the shells. Furthermore, Ti vs. O content can be calculated using integral quantification methods (see section 2.2.2).

A STEM-EELS line scan was performed as indicated by the red arrow in Figure 5.8c. Analysis of the Ti-$L_{2,3}$ edge allows determination of the Ti oxidation state. Metallic Ti has a double peak (Ti-L_3 and Ti-L_2) at 464eV and 469eV, respectively, due to the spin-orbit splitting into $2p_{3/2}$ (L_3) and $2p_{1/2}$ (L_2) levels, with a separation of 5.4eV. The degree of crystallinity and of oxidation is reflected by the further splitting of the L_2 and L_3 peaks into four sub-peaks due to the crystal-field interaction [127,129]. Figure 5.8a shows how the Ti edge changes appearance from fully oxidized Ti^{4+}-like to metallic Ti-like. In the shell region Ti appears more metallic, which is confirmed by the absence of the O-K edge. Quantification of Ti and O is shown in Figure 5.8b. The

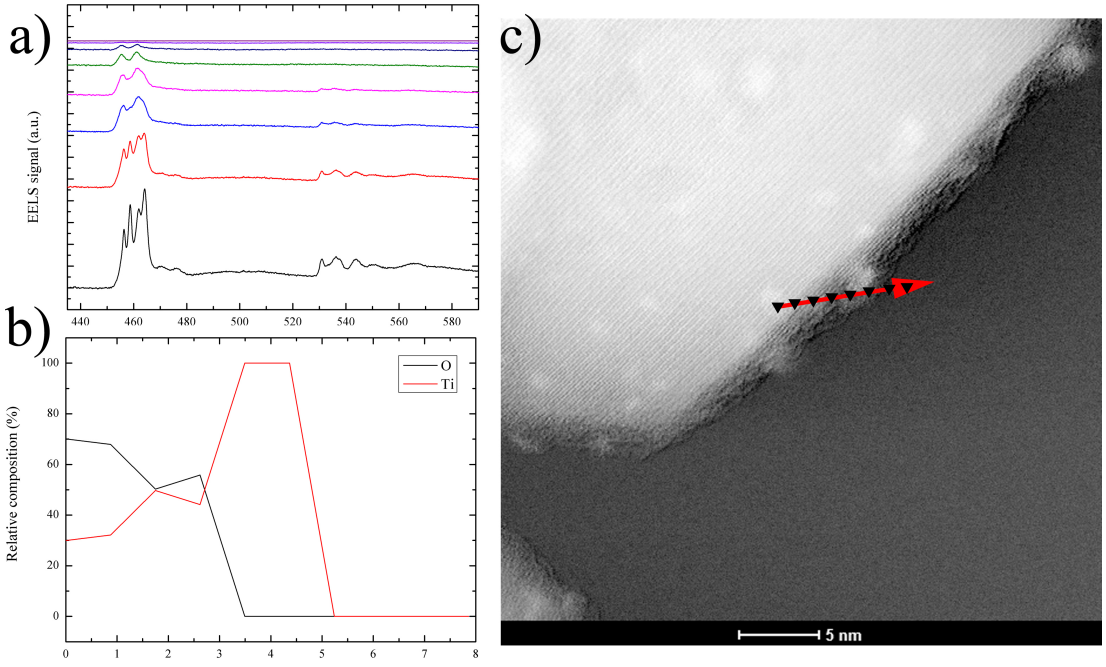

Figure 5.8: STEM-EELS line scan on an encapsulated Pt particle - a) Background-subtracted EELS spectra from the line scan indicated in (c). As the beam moves towards vacuum, the EELS signal gets lower because of the decreasing sample thickness. b) Quantification results showing the relative Ti vs O content along the line scan. The relative concentration accounts for the total signal decrease.

Ti:O ratio in the bulk is ∼3:7, whereas in the shell area it is ∼1:0.

This study provides evidence that homogeneous shells are formed on STO-supported Pt particles after reduction and calcination. Shells are metallic, even if it is surprising that calcination in air does not oxidize the reduced superficial phase formed during reduction. On one hand the formation of a bimetallic phase such as Pt/Ti cannot be excluded, given the high temperatures involved in the treatment. On the other hand, reduction in H_2 at 700°C is likely to produce a highly O-depleted STO surface, which is rearranged during calcination in air and forms segregated metallic volumes around Pt particles. When the system is illuminated, the shell is removed. This must be because the Ti-depleted region around the Pt particle is not stable ($SrTi_{(1-x)}O_3$) and the Ti moves back into the bulk where the lattice energy difference will pay for the higher surface energy of Pt. Further work on this is in progress. XPS studies of the surface oxidation state as well as the Pt oxidation state are planned.

6

Joint LSPR and TEM

Electron beam effects are often not negligible (see section 2.3) and complicate acquisition and interpretation of data. As a result, the sample behaviour within the imaged area in the microscope might be different than that away from the electron beam. In addition, if a reaction has to be followed *in situ* in the ETEM, the information is often recorded on a limited portion of the sample. Tackling these limitations, the implementation of an indirect nanoplasmonic sensing (INPS) setup (see section 2.4) in an ETEM was realized using a unique platform that allows simultaneous TEM imaging and optical spectroscopy. TEM and INPS work in a complementary way since TEM is able to probe matter on a local scale and INPS is a spectroscopic technique that collects and integrates the LSPR signal coming from the whole specimen, providing information complementary to the TEM analysis. Being able to probe the sample with INPS and ETEM at the same time allows parallel investigation at the local and global scale, as well as aiding the assessment of beam effects.

LSPR spectroscopy can probe catalytic reactions (see section 2.4) monitoring changes in adsorbate coverage with a sensitivity corresponding to less than 0.1 monolayer. However, data interpretation is often not straightforward since plasmonic shifts can be attributed to a variety of factors such as temperature, dielectric environment and other temperature-dependent optical parameters. Assessment of the major contribution to a plasmonic shift requires an *ex situ* calibration and a detailed model of reaction. For example, in the LSPR detection of size-dependent glass transition in polystyrene nanospheres [61] the glass temperature transition is correlated with the temperature at which a change in slope of the LSPR response occurs. This association corresponds

very well with external experimental data [130], but it does not provide direct evidence of what is happening. Simultaneous observation of the phase transformation with TEM would enable direct correlation of the LSPR response with the sample behaviour. Moreover, the electron beam effect is limited to a very small area (typically 20nm×20nm to 1µm×1µm), much smaller than that probed by LSPR (ideally the entire sample surface, i.e. ∼1mm×1mm in the case of a TEM sample). This means that the beam effect on the LSPR response can be neglected.
A dedicated custom TEM specimen holder containing two optical fibers, four electrical contacts, a fixed miniaturized optical bench for light handling and a heating element (see Section 3.2) has been designed. Here, the first results obtained using the combined INPS-TEM system are shown and compared to reference experiments acquired in *ex situ* INPS reactors.

6.1 *Ex situ* reflection INPS measurements

Typically, INPS is performed in transmission (see Section 2.4). Since the INPS-TEM setup is designed for reflection measurements (see Section 3.2), experiments with a reflection INPS platform were conducted in order to obtain benchmark data and understand the LSPR signal in this different geometry (see Figure 6.1). Although the setup does not allow heating to temperatures higher than 250°C, it provides essential feedback on the feasibility of reflection-mode experiments.
Since the standard Insplorion® acquisition software cannot handle reflection spectra, a Mathematica® code was written for analyzing data (see Appendix B). The code processes reflection spectra and runs the same polynomial curve fitting procedure and peak analysis that the Insplorion® software does.
A set of experiments that is relatively easy to perform both in the ETEM and in the reflection reactor was outlined as proof-of-concept. First, nanoparticle sintering can be studied *in situ* in the ETEM [35] and by INPS [131]. Gold nanoparticles can readily be prepared by sputtering a thin Au film on a support, therefore the study of such system was considered as a first option. Furthermore, the plasmonic properties of metallic Cu nanoparticles [132] are likely to change if oxidation occurs, especially if a behaviour similar to that of Pd clusters during oxidation and reduction has to be expected [63]. Since the effect of reduction and oxidation of supported Cu particles has been observed

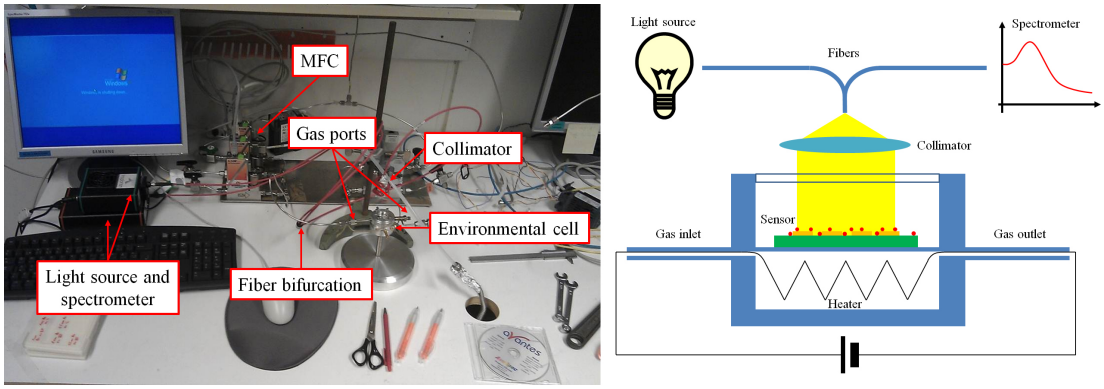

Figure 6.1: Reflection INPS setup - Setup for reflection INPS experiments and its schematic representation. A cylindrical windowed environmental cell is connected to a set of mass flow controllers via a single gas inlet channel, while a single gas outlet is dedicated to exhaust gas. The double end of a bifurcated fiber is connected to a light source and a spectrometer, the single end being connected to a fiber collimator. The sample — illuminated through a quartz window— is heated by resistive heating in the environmental cell.

in the ETEM [133], this experiment was identified as a second candidate for simultaneous TEM and INPS observation.

Gold nanoparticle sintering in air was the first experiment performed. Supported Au nanoparticles are used as a catalyst for CO oxidation [134], and sintering is one of the most common catalyst deactivation mechanisms. A Si-supported nanoplasmonic sensor was prepared with 50nm Au disks covered by 10nm SiO_2. 0.5nm Au was evaporated on top of the sensor. The chip was placed in the environmental cell under a collimator, without the windowed lid (see Figure 6.1). A heating ramp was programmed with 50°C temperature steps every 2 hours, starting from 100°C up to 250°C. A spectrum was recorded every second as the average of 5 spectra acquired with 50ms acquisition time each. Figure 6.2a shows the results. A plasmonic peak shift towards shorter wavelengths was recorded after each temperature increase until 200°C. When a temperature of 250°C was reached, the peak started to gradually red-shift, interrupted when the sample was brought back to room temperature. The initial blue shift could be due to changes in the refractive index of the material upon heating, while the transient behaviour during the 250°C step is attributed to something actually happening on the sensor surface, possibly gold sintering. The necessity for direct observation becomes clear in this case.

A second experiment was conducted on a sensor coated with 0.5nm copper. The chip

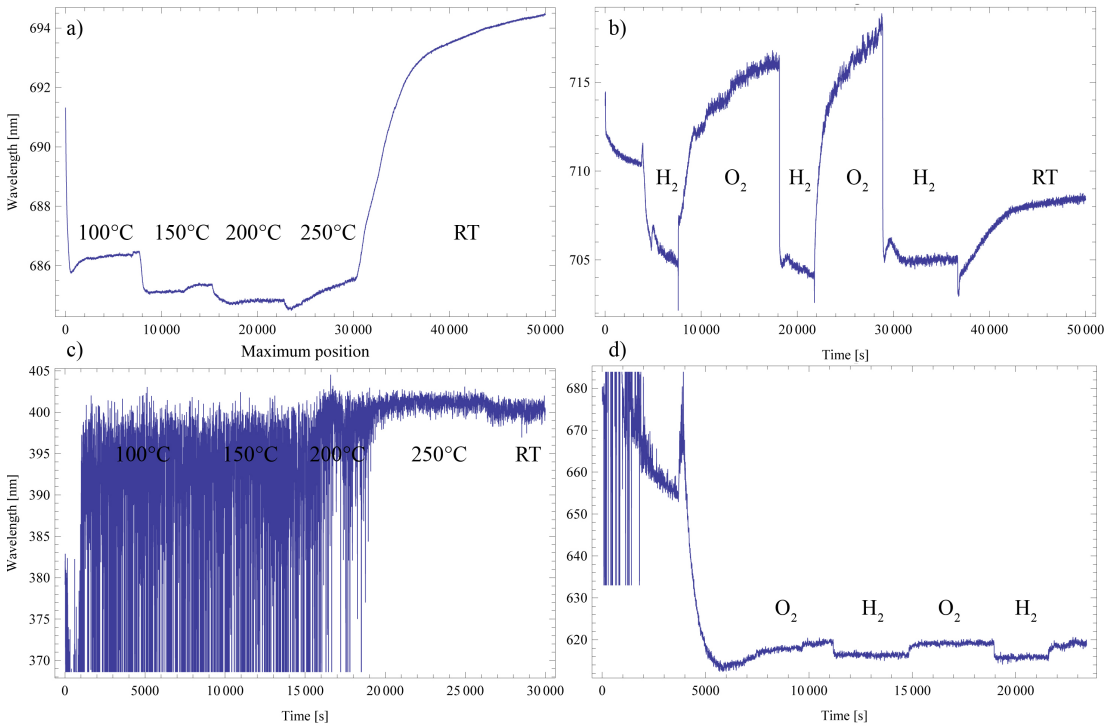

Figure 6.2: Reflection INPS data - Indirect (a-b) and direct (c-d) plasmonic sensing experiments. a) A 0.5nm thick Au layer was evaporated on top of a Si-based INPS sensor. The system was heated in air with 50°C temperature steps. b)A 1nm thick Cu layer was evaporated on top of a Si-based INPS sensor, then the system was heated at 250°C and an alternating H_2/O_2 atmosphere was cycled in the chamber. c) A thin Au layer was evaporated on a Si chip and heated in air to 100, 150, 200 and 250°C. d) A thin Cu layer was evaporated on a Si chip, heated to 250°C and exposed to an alternating H_2/O_2 atmosphere. The plots represent the plasmonic peak position as a function of time.

was placed in the environmental cell and heated to 250°C in Ar atmosphere at 1bar pressure, then mixtures of 99:1 Ar:H_2 and 99:1 Ar:O_2 were alternately introduced at intervals of ∼1-3 hours. A plasmonic peak shift is observed after each gas mixture is introduced. A red shift during oxygen exposure proceeds for a long time, probably indicating that Cu is being gradually oxidized. During hydrogen exposure a steady-state peak position is rapidly restored, consistently with an expected stable and defined plasmonic response of metallic particles. This data is consistent with that reported in literature for Pd redox cycles [63].

An even simpler experimental plasmonic system consists of a Si wafer coated with a thin Au layer. Au nanoparticles formed upon dewetting are plasmonically active and effectively act as plasmonic sensors. Since the LSPR is dependent on particle size and shape, such a system exhibits a clear LSPR response upon particle sintering. This constitutes a direct nanoplasmonic sensing setup and is arguably one of the most straightforward experiments to try in the INPS-TEM system. Results from reflection direct nanoplasmonic sensing carried out on such sample are shown in Figure 6.2c and 6.2d.

The direct plasmonic sensing experiments were carried out on bare Si chips. First, a 0.5nm thick Au layer was evaporated, than the chip was placed in the environmental cell without the windowed lid, and the system was heated in air to a temperature of 100°C, 150°C and 250°C, respectively. Unfortunately, in this case the optical response of the system (shown in Figure 6.2c) is very noisy and difficult to interpret. This is attributed to a failure in the fitting procedure, probably due to an ill-defined plasmonic resonance peak. In fact, a peak is formed only after the temperature reaches 250°C. The peak persists when the sample is brought back to room temperature, thus the peak position can be actually identified by the software. This can be an indication that Au particles have sintered and formed larger clusters with a well-defined LSPR.

As a second direct sensing experiment, a 0.5nm thick Cu film was evaporated onto a Si wafer which was placed in the environmental chamber. The temperature was raised to 250°C in 100% Ar at atmospheric pressure, then mixtures of 99:1 Ar:H_2 and 99:1 Ar:O_2 were alternately introduced with intervals of ∼1 hour. In this case, a clear shift in the LSPR peak position is measured (see Figure 6.2d). The behaviour corresponds well with that observed in Figure 6.2b, which suggests that the oxidation and reduction of Cu particles on the Si wafer is inducing a change in the plasmonic response.

These preliminary experiments are not meant to be conclusive on the gold and copper behaviour under the described conditions, but should provide a reference dataset for experimental reproducibility and data interpretation of INPS experiments *in situ* in the ETEM (Section 6.3).

6.2 *Ex situ* testing of the INPS-TEM holder

Preliminary tests of the INPS-TEM holder were conducted in the VAC-01 (see Section 3.3). Whereas extinction spectra are typically calculated by subtraction of a blank reference signal to the signal from a plasmonic sensor (see Section 2.4), this procedure is more challenging in the INPS-TEM. After a reference spectrum was acquired on a blank S-MH, the chip was substituted with a new S-MH coated with a 0.5nm-thick sputtered Au layer. The acquired reflectance profile is shown in Figure 6.3a. Similar patterns are obtained when removing and re-inserting the same blank chip. An oscillatory extinction profile is observed, suggesting an interference phenomenon probably due to misalignment. The referencing procedure is hampered by small misalignments in the chip position —a problem for INPS experiments which will be treated in Section 6.3. Reproducible chip placement is a key factor that has to be addressed. However, experiments were performed recording a reference spectrum on the same chip hosting the sample and monitoring changes in its reflectance upon heating.

An S-MH was sputter-coated with a thin layer of gold to generate Au nanoparticles by dewetting. The chip was placed in the recess of the INPS-TEM holder, fixed in place with the lid, inserted in the VAC-01 and pumped down to a pressure of $\sim$5x10^{-5}mbar. The holder was connected to the Insplorion® optical unit and to the power supply in the configuration shown in Figure 3.7. The reference spectrum was recorded on the chip, then spectra were acquired with an integration time of 5 seconds, recorded and analyzed in real time with a new version of the Insplorion® software capable of handling reflection spectra. Since the referencing is done on the sample itself, a flat extinction profile is generated. Given the absence of an LSPR feature, the intensity at a given wavelength λ_x corresponding to a change in reflectance, was monitored over time. The chosen wavelength was λ_x=600nm, i.e. the approximate position of the gold resonance. The current was ramped from 1mA to 18mA in 1mA steps, and was then brought down to 13mA in 1mA steps and finally the current supply was turned off.

Results are shown in Figure 6.3b-c.
A decrease in extinction intensity corresponds to an increase in reflectance, as noticed for the first ∼3000s. This continuous change in reflectance is attributed to a gradual change in the chip position, probably due to the relaxation of spring contacts. Whereas up to 3000s no step in extinction is noticeable upon current changes, step-like changes start occurring after a current of 11mA is reached. The temperature achieved at this point might be critical for the onset of membrane buckling, which can cause light to follow a different path. Nevertheless, a slope in the steady-state signal (after each step) is still noticeable until red heat emission is reached (18mA current, at 4190s). After this point the steady-state reflectivity after each step levels off, which can be explained by membrane stress relaxation.

6.3 *In situ* INPS-TEM of Au nanoparticle heating in O_2

A similar experiment to that described in section 6.2 was carried out in the ETEM. A gold-sputtered S-MH was placed in the INPS-TEM holder and a reference spectrum was recorded on it after insertion in the microscope. The sample was inspected in vacuum, then it was heated in vacuum until red heat emission was reached in order to anneal the sample and finally it was brought back to room temperature. Thermal glow can readily be detected by a dramatic change in the IR reflectance (see Figure 6.3). As described in Section 6.2, the reflectance levelled off when current was kept at a steady value after annealing at red heat conditions. No visible change in the sample was identified after this procedure.
A 3mbar O_2 atmosphere was introduced in the microscope and the sample was heated following the same current ramp described in Section 6.2. The effect on the sample is shown in Figure 6.4. After annealing, the particles have a broad size distribution and a variety of shapes. At a current value of ∼10mA, faceting and diffraction contrast indicate that particles are in the solid state. Sintering was observed at this temperature. At red heat condition, no faceting was observed and all particles appeared equally black, indicating that a liquid phase transition occurred. In this condition, particles were observed evaporating until the SiN_x membrane was empty. When all particles in the imaged area disappeared (Figure 6.4d-f), particles in distant areas took a longer

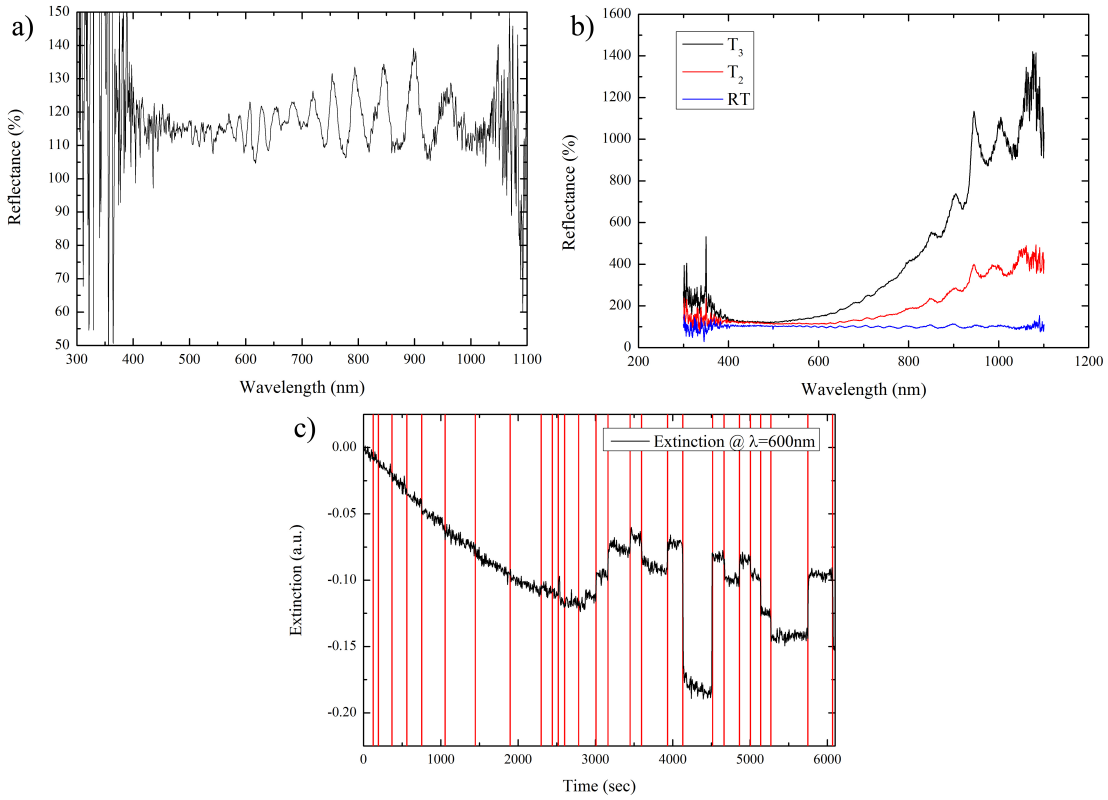

Figure 6.3: Reflectance spectra - a)The reflectance exhibits an oscillatory behaviour when a new chip is inserted after acquisition of a reference spectrum on a blank chip. The same behaviour is observed if the reference chip itself is removed and inserted again. This is interpreted as the effect of reciprocal chip misalignment. b) A gold nanoparticle-coated S-MH chip was heated in vacuum until red heat emission was achieved. The three reflectance spectra are taken at different temperatures and calculated using the same chip as a reference. The intensity of spectral oscillations —present in all spectra— grows with increasing temperature. As soon as the membrane starts glowing, the IR spectrum tail is visibly affected. However, the IR-induced reflectance change is below 300% for plasmonic-relevant wavelengths below 700nm. The IR contribution can be accounted for by acquisition and subtraction of dark spectra at each temperature step. c) Extinction of the reflectance spectrum at λ_x=600nm is plotted over time (black curve). Each current step is indicated by a red line.

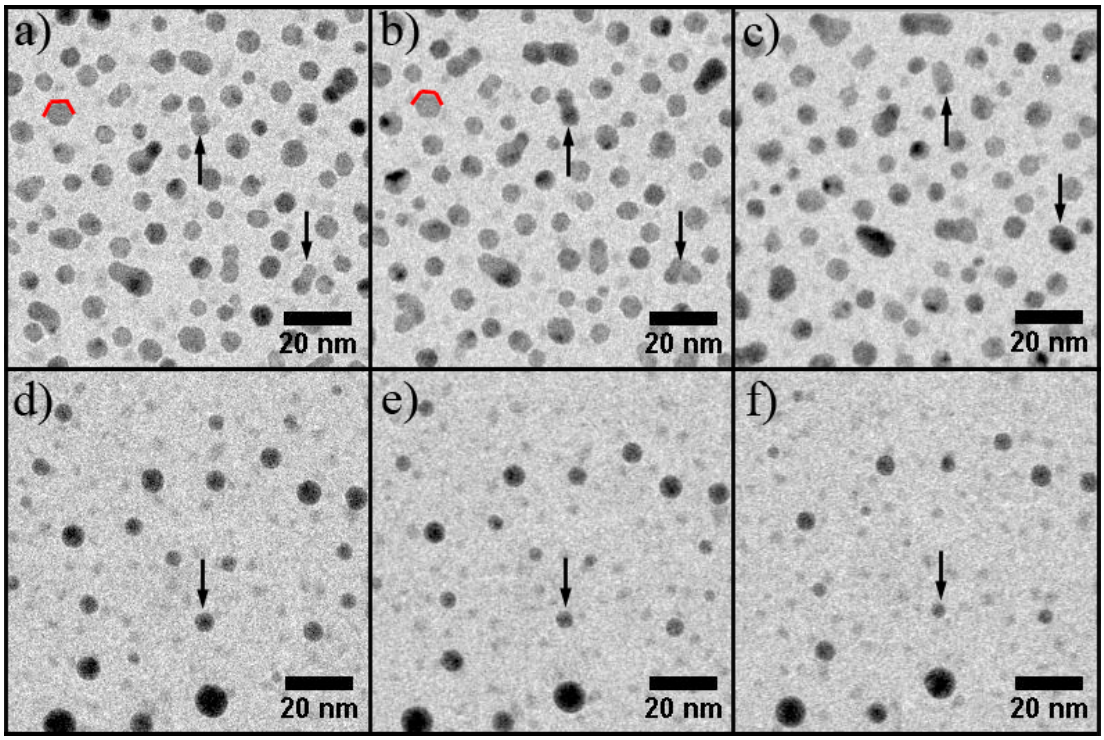

Figure 6.4: Heating Au particles in O_2 - a-c) Sintering regime. Particles are still crystalline, showing well defined facets and diffraction contrast. d-f) Evaporation regime. Particles are all round and dark, indicating that they are now in liquid phase.

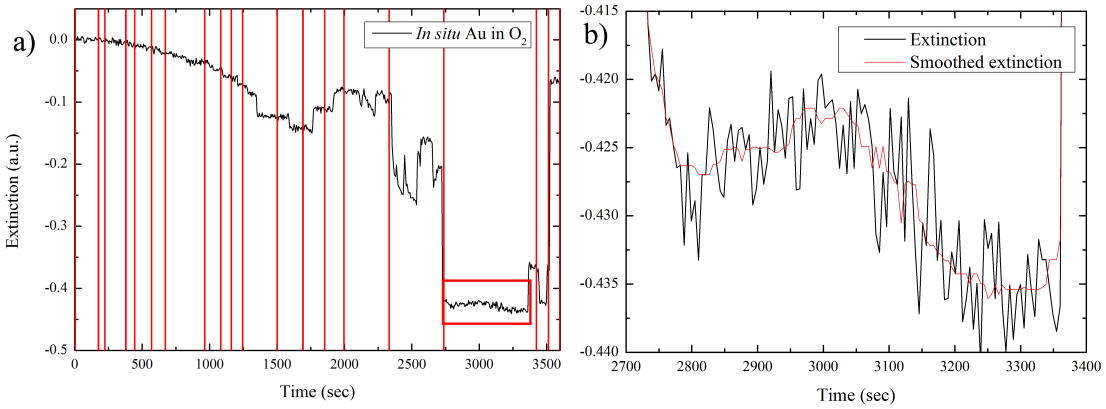

Figure 6.5: INPS signal - a) Intensity at λ_x=600nm plotted over time during *in situ* Au nanoparticle heating in 3mbar O_2. b) Magnification of the red square area in (a), corresponding to the evaporation of Au particles. The slight extinction decrease might be due to a change in the sample. The faint spots are due to faulty image gain reference.

time to evaporate completely. Therefore, the effect of the electron beam on the speed of evaporation is not negligible.

The extinction spectrum at λ_x=600nm is plotted over time in Figure 6.5. A change in reflectance is observed at each current step as in the *ex situ* experiment (Figure 6.3c), while extinction jumps recorded between current steps are directly correlated to sudden drifts along the z axis in the TEM, due to thermal structure instability. The dependence of extinction on the membrane deflection is indicating that the extinction signal is coming at least partly from the membrane. In light of this, oscillations observed in the extinction signal (Figure 6.3a) can be interpreted as interference effects, as explained in Figure 6.6.

Sample drift caused temporary imaging issues, however the duration of such drift was limited to less than 30 seconds, after which the sample was stable again. After red heat emission was reached, the system became stable and imaging of the evaporation process was possible. A slope in the extinction signal during evaporation phase is observed (Figure 6.5b), probably due to the change in the sample. Since the membrane was stable, it is more likely that such change in reflectance could be induced by the evaporation of the Au nanoparticles.

Despite interpretation of the signal remains challenging, the concept of simultaneous acquisition of TEM images and INPS data was shown. Optimization of heater stability and reproducibility of chip insertion appear to be challenges that must be tackled in

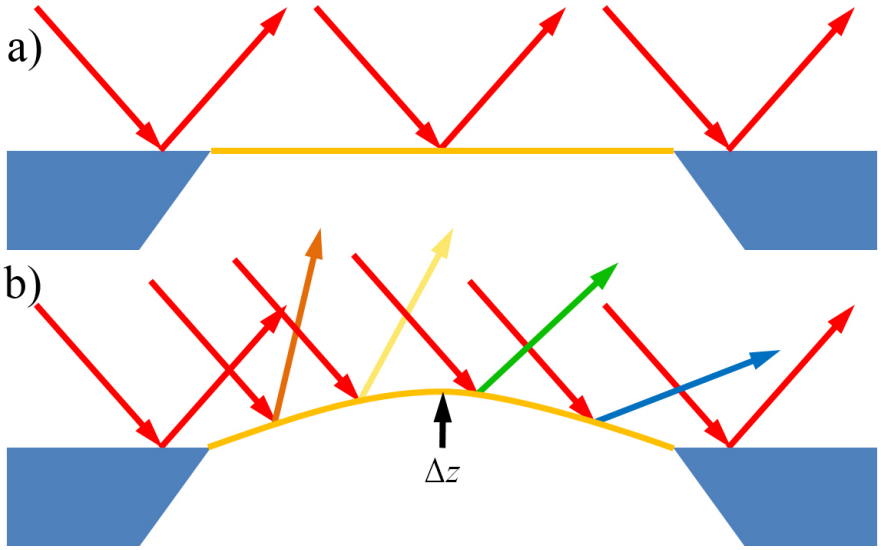

Figure 6.6: Buckling effect - Schematic model of the buckling effect on extinction signals. a) Assuming the membrane is flat at the beginning of the experiment, all incoming light will be scattered with the same angular distribution. b) Upon buckling, rays hitting the membrane will be scattered at different angles than those bouncing off the bulk, thus causing interference. An interference phenomenon could cause an oscillatory intensity in the integrated signal.

the future.

7

Conclusions and outlook

In this project, photocatalysts and photoactivated reactions were studied by means of ETEM through the design, implementation and use of customized TEM specimen holders. This work shows that a significant basic insight in chemical and physical behaviour of photocatalysts, catalysts and other materials can be given using novel specimen holders and ETEM techniques when some of the practical challenges (buckling, heating and beam effects, etc.) can be overcome. The work with novel specimen holders presented in this thesis lays the foundation for further investigations and development. There is great promise in continuing the work along the described guidelines.
In this chapter, some of the remaining open challenges are discussed and an outlook for future work is presented.

7.1 Prospects for the FB-TEM and LD-TEM holders

Two versions of the specimen holder for light illumination were constructed and tested (see Sections 3.1 and 3.2). Light activation was successfully used for studying photocatalytic phenomena as shown in Section 4.
Designing light-stimulated experiments on photocatalysts is not trivial because of the inherent difficulty of distinguishing the effects of light from those of electrons. Furthermore, what is observed in the ETEM is the *effect* of reactions —not the reactions themselves—, which in this case means that the effect of light must be detectable in the microscope. Since by definition a catalyst is a substance which is not consumed and does not change during reaction, visible reaction effects typically include catalyst

activation or deactivation. Design of experiments requires finding reactions that lead to detectable changes in the sample.

The use of EELS for direct investigation of catalytic activity in the ETEM has only been shown recently [135] and would be a novel application in the field of photocatalysis. Using EELS to detect gas products in photocatalytic reactions with and without light illumination would be an example of such technique obtainable with *in situ* light illumination in the ETEM, provided that a high catalytic conversion is achieved (an active photocatalyst and a high light intensity are required). A more sophisticated analysis would involve the use of glancing angle STEM-EELS in the proximity of the photocatalyst surface (*aloof* mode) [136] to analyze gas concentration. Aloof EELS investigation of a semiconductor photocatalyst under illumination could also give insight on the electronic state on different facets or in the vicinity of a co-catalyst particle.

Electron holography [137] has recently been used for visualization of the fringing field response of a sample to light illumination [43]. The study of solid state semiconductor devices such as p-n junctions or solar cells with *in situ* illumination is an interesting field for future work.

With the current design, the LD-TEM can deliver the highest power density on the sample through the lens system. High intensities are desirable for e.g. heating purposes. A special application of laser-induced heating is plasmon assisted chemical vapor deposition (PACVD) [138], where a laser beam is used to selectively heat metallic nanoparticles in a precursor gas. If the laser beam matches the plasmonic resonance of the particles, the particles heat up much more than the bare substrate due to plasmonic field enhancement and are able to crack the precursor, thereby starting local material deposition. However, power densities on the order of $\sim 10^{10} \mathrm{W/m^2}$ are necessary for achieving the temperatures needed for deposition [138]. Such high power densities can be reached by focusing a 1W laser source into a $\sim 5\mu$m-wide spot. This condition can be obtained in the ETEM by modification of the LD-TEM with appropriate optics and a 1W laser diode, however heat dissipation from the laser casing becomes a serious issue. Restructuring the bottom feedthrough as a heat sink would probably solve the problem, provided that the heat is not transferred to the entire holder shaft. Another solution would be that of equipping the FB-TEM model with a collimator and a focusing lens in proximity of the sample. This would avoid the heat sinking issue and allow a greater choice of laser sources, including for example powerful frequency-multiplied

Nd:YAG lasers. However, the implementation of a system for high power density delivery entails that the laser spot size is very limited with respect to the dimension of the sample. Therefore, a means of localizing the laser spot on the sample would need to be implemented as well. Such system could consist of a small CCD sensor near the sample or a sacrificial material that undergoes phase transition upon illumination (for example low-melting point materials such as Ga nanoparticles or eutectic alloys). However, having a powerful confined light spot brings up the necessity of moving the laser beam across the sample during the experiment. This can be obtained either by moving the optics or by moving the sample with micrometers or piezoelectric actuators. Other fundamental studies could be performed using light illumination in the TEM. The diffraction of electrons from standing light waves, known as the Kapitza-Dirac effect [139], might be investigated by implementing a simple cavity resonator inside the holder tip. Injecting polarized light between two parabolic mirrors facing each other, one with 99% reflectivity, would produce a standing wave that could act as a diffraction grating for the electron beam. Direct observation of this effect in the TEM would be novel.

7.2 Prospects for the INPS-TEM holder

The INPS-TEM holder offers the unique chance of performing simultaneous LSPR spectroscopy and ETEM investigation.

Reproducibility of the INPS acquisition conditions is a priority in order to perform referencing (see Section 6). An anti-reflective coating (e.g. an amorphous carbon layer) covering the chip surface excluding the membrane could limit the amount of light that is reflected away from the plasmonic sensor. Implementation of such layer could be performed by shadow mask lithography as a last step in the heater fabrication or by spin coating of a carbon-based polymer (e.g. SU-8 photoresist) followed by patterning and pyrolysis at an early stage in the fabrication process, i.e. when the membrane is not suspended yet. Moreover, the light path can be adjusted by fiber cleaving in order to compensate for mirror or fiber placement irregularities and direct the beam primarily on the membrane.

Experiments with actual patterned sensors are of primary importance. Furthermore,

experiments at room temperature should be designed to rule out the contribution of the heater to the plasmonic signal, e.g. Pd hydride formation [65, 70, 71].
The INPS-TEM can also be used in combination with other kinds of optical spectroscopy that use a light reflection geometry, for example surface enhanced Raman spectroscopy (SERS) [140]. The combination of ETEM with other spectroscopic techniques further increases the versatility of the system and the range of complementary information achievable during one experiment.
The two fibers can be used in combination for light acquisition, thereby maximizing the collection angle. The holder in this configuration could be used for cathodoluminescence experiments [75].
Finally, both fibers could be used for illumination. In this configuration the holder is an advanced version of the FB-TEM in that a heater is implemented. For example, *in situ* illumination of reduced/oxidized STO (see Chapter 5) could be performed to directly investigate the effect of light on the shells.
The room for development and creative utilization of this novel platform motivates future work.

7.3 Prospects for the VAC-01

The vacuum chamber can be connected to an environmental gas inlet system that provides a controlled atmosphere at atmospheric pressure. Experiments that need pressures higher than those achievable in the ETEM (<10mbar) could be performed in combination with the VAC-01. Using a vacuum-transfer TEM holder, the sample can be transferred from the ETEM to the VAC-01 under controlled atmosphere and the experiment can be run at higher pressures while monitoring the sample by light spectroscopy (see Section 3.3).

7.4 Experimental follow-up

7.4.1 Photocatalyst deactivation

In Section 4.1 the photocorrosion of Cu_2O nanocubes was induced and studied *in situ* in the ETEM. Other light-induced photocatalyst deactivation mechanisms could be

studied using *in situ* light activation, giving insight in the reaction mechanisms and ideally providing routes for reducing the deactivation processes.

7.4.2 Photodeposition

Photodeposition of different materials onto a GaN:ZnO semiconductor photocatalyst was successfully reproduced in the ETEM using the FB-TEM holder (see Sections 4.2, 4.3 and 4.4). *In situ* investigation helped towards the optimization of MoS_2 deposition and in the understanding of selective Ru deposition using carrier scavengers. Photodeposition is a common photocatalyst preparation technique that can be characterized using light illumination in the ETEM, in principle on any semiconductor photocatalyst and with any precursor. Photocatalytic test on the Ru/GaN:ZnO and MoS_2/GaN:ZnO systems is underway.

7.4.3 Pt nanoparticle encapsulation on STO

As seen in Chapter 5, the effect of SMSI affects the activity and selectivity of a photocatalyst. An overall improvement of the net activity of STO-supported Pt nanoparticles was achieved by reduction and oxidation of the system and the effect of this treatment was investigated using ETEM and µ-reactor tests. The suppression of back reactions was successfully achieved but was deemed unstable after visible light irradiation. Shell stability test and optimization must be performed.
A multi-layer Ti-enriched system was prepared on the basis of these assumptions, consisting of a STO substrate covered with a 5nm-thick Ti layer and the Pt particulate. The idea is to produce a more stable Ti substrate for the Pt/shell structures. The Ti base-layer should provide the Ti species for Pt decoration, but the depletion of Ti atoms from it would not induce a change in the local oxidation state in the vicinity of the particle. Therefore, less driving force for Ti species to migrate back in the support should be felt.

Appendix A

Technical drawings

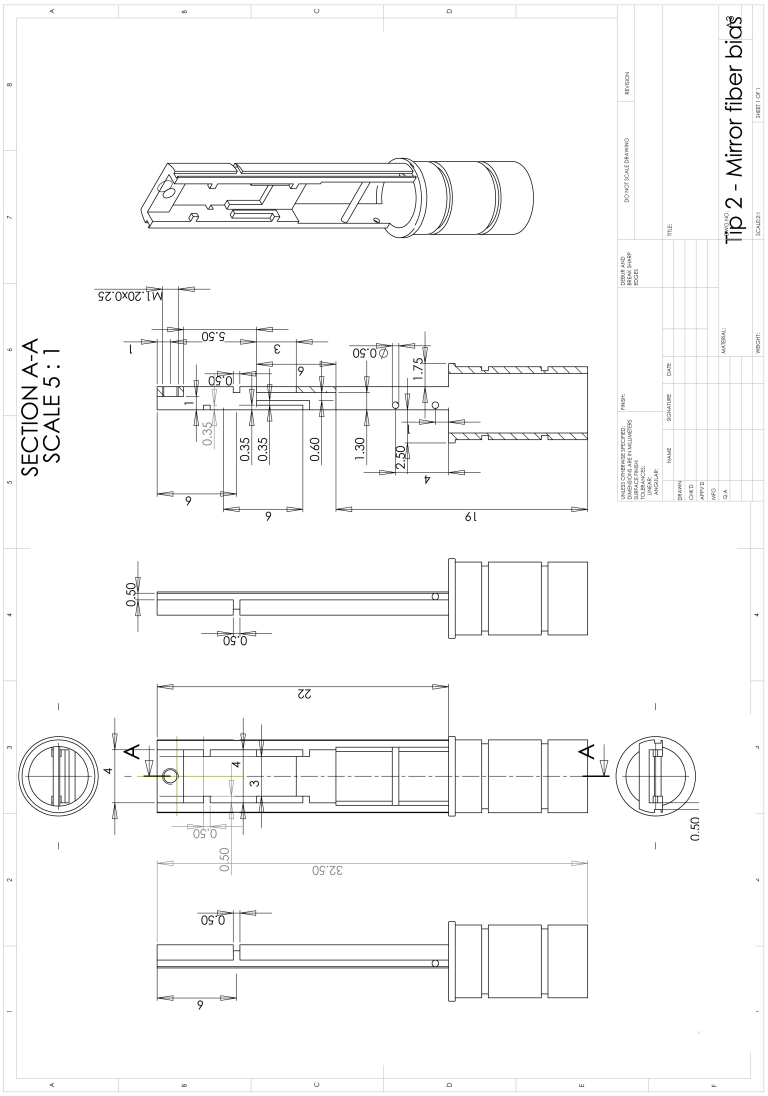

Figure A.1: INPS-TEM tip - Technical drawing with dimensions of the latest model of INPS-TEM.

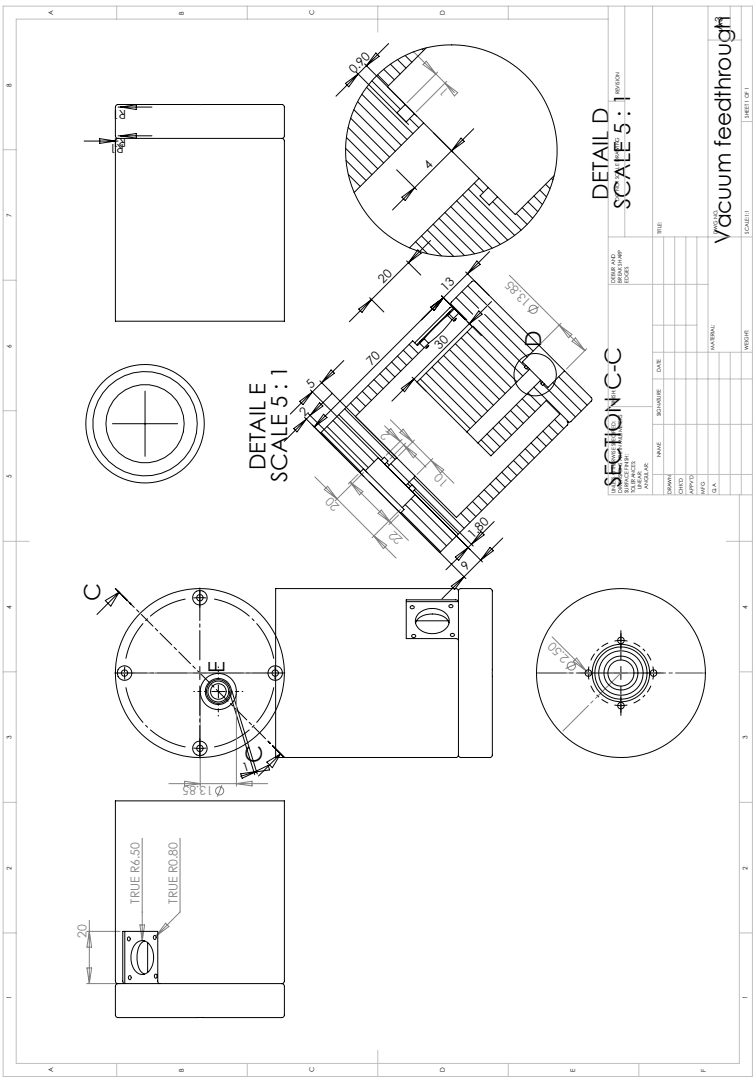

Figure A.2: Vacuum Feedthrough - Technical drawing with dimensions of the vacuum feedthrough.

Appendix B

Mathematica code for processing of reflection INPS spectra

Data acquisition

(*Select files to analyze*)

{FileNameSetter[Dynamic[f], "OpenList"], Dynamic[f]}

(*Definition of a matrix "a" where the spectra will be put and initialization with generic $m_{i,j}$ values*)

a = Table [$m_{i,j}$, {i, Length[f] + 1}, {j, 5}] //MatrixForm;

(*Initialization of the first column of "a" with the wavelength vector*)

mat = Import[f[[1]], "Table", "FieldSeparators"->{";"}];
M = mat[[8;;, 1;;All]];
M1 = M[[All, 1]];
a[[All, 1]] = M1;

B. MATHEMATICA CODE FOR PROCESSING OF REFLECTION INPS SPECTRA

(*Cycle that imports each file selected, extracts the spectra and assigns it to a column in a matrix “a”*)

ProgressIndicator[Dynamic[i], {1, Length[f]}]

For[$i = 1, i$<=Length[f], i++,

mat = Import[f[[i]], “Table”, “FieldSeparators”->{“;”}];

M = mat[[8;;, 1;;All]];

M5 = M[[All, 5]];

a[[All, $i + 1$]] = M5;

]

$s = 0$;

$n = 0$;

$l = 0$;

$m = 0$;

$k = 2$;

{“Define min wavelength: ”Slider[Dynamic[n], {IntegerPart[a[[1, 1]][[1]]], IntegerPart[Max[a[[1, 1]]]], 1}],

Style[“n =”, FontColor → Blue]Style[Dynamic[n], Blue]}

{“Define max wavelength: ”Slider[Dynamic[l], {IntegerPart[a[[1, 1]][[1]]], IntegerPart[Max[a[[1, 1]]]], 1}],

Style[“l =”, FontColor → Black]Style[Dynamic[l], Black]}

{“Define span: ”Slider[Dynamic[s], {0, IntegerPart[Max[a[[1, 1]]]/2, 1}], Dynamic[s]}

{“Define single wavelength: ”

Slider[Dynamic[m], {IntegerPart[a[[1, 1]][[1]]], IntegerPart[Max[a[[1, 1]]]], 1}],

Style[“m =”, FontColor → Red]Style[Dynamic[m], Red]}

{Slider[Dynamic[k], {2, Length[f], 1}], Style[“Spectrum number ”, FontColor → Green]Style[Dynamic[k],

Green],

Dynamic[Show[ListLinePlot[Transpose[{a[[1, 1]], a[[1, k]]}], Frame → True, Axes → False,

FrameLabel → {"Wavelenght", "a.u."}, AxesOrigin → {Min[a[[1, 1]]], Automatic}],
Graphics[{Red, Line[{{m, 0}, {m, Max[a[[1, 2]]]}}]}], Graphics[{Blue, Line
[{{n, 0},{n, Max[a[[1, 2]]]}}]}],
Graphics[Line[{{l, 0}, {l, Max[a[[1, 2]]]}}]]]}

Data processing

(*Definition of variables*)

data = Transpose[{a[[1, 1]], a[[1, 2]]}];
npos = First[Position[IntegerPart[data], n]][[1]];
mpos = First[Position[IntegerPart[data], m]][[1]];
lpos = First[Position[IntegerPart[data], l]][[1]];

datasel = data[[npos;;lpos, 1;;All]];

dataset = Table [$m_{i,j}$, {i, Length[f]}, {j, 6}] ; (*Definition of the dataset matrix*)
dataset[[All, 1]] = 5Range[Length[f]];

(*Initialization of the first column of dataset with the time vector.
Set time per acquisition as scaling factor*)

{ProgressIndicator[Dynamic[i], {1, Length[f]}], Length[f]/Dynamic[i]}

(*Cycle that fits data in a given range for each column of "a"*)

For[i = 1, i ≤ Length[f], i++,

```
data = Transpose[{a[[1, 1]], a[[1, i + 1]]}];
npos = First[Position[IntegerPart[data], n]][[1]]; (*retrieve the position containing the value n*)
mpos = First[Position[IntegerPart[data], m]][[1]]; (*retrieve the position containing the value m*)
lpos = First[Position[IntegerPart[data], l]][[1]]; (*retrieve the position containing the value l*)
datasel = data[[npos;;lpos, 1;;All]];
nbasis[z_Integer][x_]:=Table[x^k, {k, 0, z}]; (*Definition of polynomial of nth order in x*)
fit = Fit[datasel, nbasis[20][x], x]; (*Data fitting algorithm*)
ymax = FindMaximum[{fit, npos < x < lpos}, {x, mpos}, MaxIterations → 300];
(*Finds local maximum of fit between npos and lpos starting from mpos*)
xmax = x/.Last[FindMaximum[{fit, npos < x < lpos}, {x, mpos}, MaxIterations → 300]];
(*Picks the x of the maximum*)
wav = fit/.x → mpos; (*Picksthevalueoffitatmpos(redmarker)*)
extdiff = (fit/.x → (spanpos1)) − (fit/.x → (spanpos2));
(*Calculates extinction curve skewness as the height difference between the value of fit at npos and lpos*)
centroid = NIntegrate[xSqrt[(D[fit, x])^2 + 1], {x, npos, lpos}]/
NIntegrate[Sqrt[(D[fit, x])^2 + 1], {x, npos, lpos}]; (*Calculates the centroid from the*)
dataset[[i, 2]] = First[ymax];
dataset[[i, 3]] = xmax;
dataset[[i, 4]] = wav;
dataset[[i, 5]] = extdiff;
dataset[[i, 6]] = centroid;
]
```

Plot

```
{ListLinePlot[Transpose[{dataset[[All, 1]], dataset[[All, 2]]}], Frame → True, Axes → False,
PlotLabel → "Intensity at maximum",
```

```
FrameLabel → {"Time [s]", "Reflectivity [%]"}],
ListLinePlot[Transpose[{dataset[[All, 1]], dataset[[All, 3]]}], Frame → True, Axes → False,
PlotLabel → "Maximum position",
FrameLabel → {"Time [s]", "Wavelength [nm]"}],
ListLinePlot[Transpose[{dataset[[All, 1]], dataset[[All, 4]]}], Frame → True, Axes → False,
PlotLabel → "Intensity at wavelength", FrameLabel → {"Time [s]", "Reflectivity [%]"}],
ListLinePlot[Transpose[{dataset[[All, 1]], dataset[[All, 5]]}], Frame → True, Axes → False,
PlotLabel → "Extinction difference", FrameLabel → {"Time [s]", "a.u."}],
ListLinePlot[Transpose[{dataset[[All, 1]], dataset[[All, 6]]}], Frame → True, Axes → False,
PlotLabel → "Centroid",
FrameLabel → {"Time [s]", "Wavelength [nm]"}]}
```

Save

```
Export["Intensity at maximum.pdf", ListLinePlot[Transpose[{dataset[[All, 1]],
dataset[[All, 2]]}], Frame → True, Axes → False, PlotLabel → "Intensity at maximum",
FrameLabel → {"Time [s]", "Reflectivity [%]"}]];
Export["Maximum position.pdf", ListLinePlot[Transpose[{dataset[[All, 1]],
dataset[[All, 3]]}], Frame → True, Axes → False, PlotLabel → "Maximum position",
FrameLabel → {"Time [s]", "Wavelength [nm]"}]];
Export["Intensity at wavelength.pdf", ListLinePlot[Transpose[{dataset[[All, 1]],
dataset[[All, 4]]}], Frame → True, Axes → False, PlotLabel → "Intensity at wavelength",
FrameLabel → {"Time [s]", "Reflectivity [%]"}]];
Export["Extinction difference.pdf", ListLinePlot[Transpose[{dataset[[All, 1]],
dataset[[All, 5]]}], Frame → True, Axes → False, PlotLabel → "Extinction difference",
FrameLabel → {"Time [s]", "a.u."}]];
Export["Centroid.pdf", ListLinePlot[Transpose[{dataset[[All, 1]],
```

```
dataset[[All, 6]]}], Frame → True, Axes → False, PlotLabel → "Centroid",
FrameLabel → {"Time [s]", "Wavelength [nm]"}]];
Export["Data.dat", dataset];
```

References

[1] Cavalca, F., Laursen, a. B., Kardynal, B. E., Dunin-Borkowski, R. E., Dahl, S., Wagner, J. B., and Hansen, T. W. *Nanotechnology* **23**(7), 075705 January (2012). iv, 40, 57

[2] Wagner, J. B., Cavalca, F., Damsgaard, C. D., Duchstein, L. D. L., and Hansen, T. W. *Micron (Oxford, England : 1993)* March (2012). iv, 23, 26

[3] He, M., Liu, B., Chernov, A. I., Obraztsova, E. D., Kauppi, I., Jiang, H., Anoshkin, I., Cavalca, F., Hansen, T. W., Wagner, J. B., Nasibulin, A. G., Kauppinen, E. I., Linnekoski, J., Niemelä, M., and Lehtonen, J. *Chemistry of Materials* **24**(10), 1796–1801 May (2012). iv

[4] Kleiman-Shwarsctein, A., Laursen, A. B., Cavalca, F., Tang, W., Dahl, S. r., and Chorkendorff, I. *Chemical communications (Cambridge, England)* **48**(7), 967–9 January (2012). iv

[5] Laursen, A. B., Gorbanev, Y. Y., Cavalca, F., Malacrida, P., Kleiman-Schwarsctein, A., Kegnæ s, S. r., Riisager, A., Chorkendorff, I., and Dahl, S. r. *Applied Catalysis A: General* **433-434**, 243–250 August (2012). iv

[6] Lewis, N. S. and Nocera, D. G. *Proceedings of the National Academy of Sciences* **103**(43), 15729–15735 October (2006). 1

[7] Lewis, N. S. and Crabtree, G. W. *US Department of Energy Office of Basic Energy Sciences* (2005). 2

[8] Boyes, E. D. and Gai, P. L. *Ultramicroscopy* **67**(14), 219–232 June (1997). 3, 23

[9] Thomas, J. M. and Thomas, W. J. *Principles and practice of heterogeneous catalysis*, volume 171. Wiley-VCH, (1997). 5, 9

[10] Chorkendorff, I. and Niemantsverdriet, J. W. *Concepts of Modern Catalysis and Kinetics*, volume 44. Wiley-VCH, (2003). 6, 7

[11] Somorjai, G. A. *Introduction to Surface Chemistry and Catalysis*, volume 13. Wiley, (1994). 8

[12] Haruta, M., Kobayashi, T., Sano, H., and Yamada, N. *Chemistry Letters* **16**(2), 405–408 (1987). 8

[13] Forzatti, P. and Lietti, L. *Catalysis today* **52**(2-3), 165–181 (1999). 9

[14] HEIDT, L. J. *PROC AMER ACAD ARTS AND SCI* **79**((4)), 228–235 (1951). 9

[15] Fujishima, A. and Honda, K. *Bull. Chem. Soc. Jpn.* **44**(4), 1148 (1971). 9, 74

[16] Fujishima, A. and Honda, K. *Nature* **238**, 37 (1972). 9, 74

[17] Paleocrassas, S. N. *Solar Energy* **16**, 45–51 (1974). 9

[18] Gibson, T. and Kelly, N. *International Journal of Hydrogen Energy* **33**(21), 5931–5940 November (2008). 10

[19] Kelly, N., Gibson, T., and Ouwerkerk, D. *International Journal of Hydrogen Energy* **33**(11), 2747–2764 June (2008). 10

[20] Cortright, R., Davda, R., and Dumesic, J. *Nature* **418**(August), 54–57 (2002). 10

[21] Walter, M. G., Warren, E. L., McKone, J. R., Boettcher, S. W., Mi, Q., Santori, E. a., and Lewis, N. S. *Chemical reviews* **110**(11), 6446–73 November (2010). 10

[22] Kudo, A. and Miseki, Y. *Chemical Society reviews* **38**(1), 253–78 January (2009). 10, 77

[23] Ramette, R. *Journal of Chemical Education* **64**(10), 55057 (1987). 10

[24] Weber, M. and Dignam, M. *International journal of hydrogen energy* **11**(4), 225–232 (1986). 10

[25] Joo, J. B., Zhang, Q., Dahl, M., Lee, I., Goebl, J., Zaera, F., and Yin, Y. *Energy & Environmental Science* **5**(4), 6321 (2012). 11

[26] Takanabe, K. and Domen, K. *Green* **1**(4), 313–322 January (2011). 11

[27] Scaife, D. *Solar Energy* **25**, 41–54 (1980). 12

[28] James, B., Baum, G., and Perez, J. *U.S. Department of Energy* **22201**(December) (2009). 12

[29] Maeda, K. and Domen, K. *The Journal of Physical Chemistry Letters* **1**(18), 2655–2661 September (2010). 12

[30] Nano.gov. 13

[31] Egerton, R. *Electron Energy-Loss Spectroscopy in the Electron Microscope*. Springer US, Boston, MA, (2011). 16, 61, 64

[32] Williams, D. B. and Carter, C. B. *Transmission Electron Microscopy*. Springer, (2009). 16

[33] Zaluzec, N. *Ultramicroscopy* **9**, 2–6 (1982). 18

[34] Johnson, D. and Spence, J. *Journal of Physics D: Applied physics* **7**(6), 771 –780 (1974). 19

[35] Hansen, T. W., Wagner, J. B., and Dunin-Borkowski, R. E. *Materials Science and Technology* **26**(11), 1338–1344 November (2010). 23, 26, 88

[36] Liu, J. J. *ChemCatChem* **3**(6), 934–948 June (2011). 23, 77, 78

REFERENCES

[37] Hansen, T. W., Wagner, J. B., Hansen, P. L., Dahl, S. r., Topsø e, H., and Jacobsen, C. J. H. *Science* **294**(November), 1508–1510 (2001). 23

[38] Creemer, J. F., Helveg, S., Hoveling, G. H., Ullmann, S., Molenbroek, a. M., Sarro, P. M., and Zandbergen, H. W. *Ultramicroscopy* **108**(9), 993–8 August (2008). 23, 25, 44

[39] Klein, K. L., Anderson, I. M., and de Jonge, N. *Journal of microscopy* **242**(2), 117–23 May (2011). 25, 68

[40] Yaguchi, T., Suzuki, M., Watabe, A., Nagakubo, Y., Ueda, K., and Kamino, T. *Journal of electron microscopy* **60**(3), 217–25 January (2011). 25

[41] Milas, M., Zhu, Y., and Rameau, J. *US Patent 8,143,593* (2012). 25, 40

[42] Tanabe, T., Muto, S., and Tohtake, S. *Journal of electron microscopy* **51**(5), 311–3 January (2002). 25, 40

[43] Shindo, D., Takahashi, K., Murakami, Y., Yamazaki, K., Deguchi, S., Suga, H., and Kondo, Y. *Journal of electron microscopy* **58**(4), 245–9 August (2009). 25, 40, 100

[44] Lau, J. W., Schofield, M. a., and Zhu, Y. *Ultramicroscopy* **107**(4-5), 396–400 (2007). 25

[45] Uhlig, T., Heumann, M., and Zweck, J. *Ultramicroscopy* **94**(3-4), 193–6 April (2003). 25

[46] Egerton, R. F., Li, P., and Malac, M. *Micron (Oxford, England : 1993)* **35**(6), 399–409 January (2004). 26

[47] Egerton, R. F., Wang, F., and Crozier, P. a. *Microscopy and microanalysis : the official journal of Microscopy Society of America, Microbeam Analysis Society, Microscopical Society of Canada* **12**(1), 65–71 February (2006). 26

[48] Ashcroft, N. W. and Mermin, N. D. *Solid State Physics*, volume 2 of *Holt-Saunders International Editions: Science : Physics*. Brooks Cole, (1976). 27

[49] Park, Q.-H. *Contemporary Physics* **50**(2), 407–423 March (2009). 27

[50] Jung, L., Campbell, C., and Chinowsky, T. *Langmuir* **7463**(17), 5636–5648 (1998). 27

[51] Willets, K. a. and Van Duyne, R. P. *Annual review of physical chemistry* **58**, 267–97 January (2007). 27, 29

[52] Bohren, C. F. and Huffman, D. R. *Absorption and Scattering of Light by Small Particles*. (2007). 27

[53] Fleischmann, M., Hendra, P., and McQuillan, A. *Chemical Physics Letters* **26**(2), 2–5 (1974). 27

[54] Jeanmaire, D. L. and Van Duyne, R. P. *Journal of Electroanalytical Chemistry and Interfacial Electrochemistry* **84**(1), 1–20 November (1977). 27

[55] Anker, J. N., Hall, W. P., Lyandres, O., Shah, N. C., Zhao, J., and Van Duyne, R. P. *Nature materials* **7**(6), 442–53 June (2008). 27, 28, 29

[56] Atwater, H. a. and Polman, A. *Nature materials* **9**(3), 205–13 March (2010). 27

[57] Giannini, V., Fernandez-Dominguez, A. I., Heck, S. C., and Maier, S. a. *Chemical reviews* **111**(6), 3888–3912 June (2011). 28

[58] Jensen, T. R., Malinsky, M. D., Haynes, C. L., and Van Duyne, R. P. *The Journal of Physical Chemistry B* **104**(45), 10549–10556 November (2000). 28

[59] Haynes, C. L. and Van Duyne, R. P. *The Journal of Physical Chemistry B* **105**(24), 5599–5611 June (2001). 29

[60] Novo, C., Funston, A. M., and Mulvaney, P. *Nature nanotechnology* **3**(10), 598–602 October (2008). 29

[61] Langhammer, C., Larsson, E. M., Kasemo, B., and Zoric, I. *Nano Letters* , 100818084441061 August (2010). 29, 30, 40, 87

[62] Larsson, E. M., Langhammer, C., Zorić, I., and Kasemo, B. *Science (New York, N.Y.)* **326**(5956), 1091–4 November (2009). 31, 40

[63] Langhammer, C. and Larsson, E. M. *ACS Catalysis* **2**(9), 2036–2045 September (2012). 31, 88, 91

[64] Gusak, V., Heiniger, L.-P., Graetzel, M., Langhammer, C., and Kasemo, B. *Nano letters* **12**(5), 2397–403 May (2012). 31

[65] Langhammer, C., Zhdanov, V. P., Zorić, I., and Kasemo, B. *Chemical Physics Letters* **488**(1-3), 62–66 March (2010). 31, 40, 102

[66] Miller, B. and Crozier, P. *Microscopy and Microanalysis* **17**(S2), 472–473 October (2011). 34, 40

[67] Miller, B. and Crozier, P. *Microscopy and Microanalysis* **18**(Suppl 2), 1074–1075 (2012). 34, 40

[68] Yoshida, K., Yamasaki, J., and Tanaka, N. *Applied Physics Letters* **84**(14), 2542 (2004). 34

[69] Yoshida, K., Nozaki, T., Hirayama, T., and Tanaka, N. *Journal of electron microscopy* **56**(5), 177–80 October (2007). 34, 40

[70] Langhammer, C., Zhdanov, V. P., Zorić, I., and Kasemo, B. *Physical Review Letters* **104**(13), 2–5 March (2010). 40, 102

[71] Zorić, I., Larsson, E. M., Kasemo, B., and Langhammer, C. *Advanced Materials* **22**(41), 4628–33 November (2010). 40, 102

[72] Yoshida, K., Nanbara, T., Yamasaki, J., and Tanaka, N. *Microscopy and Microanalysis* **11**(S02), 214–215 August (2005). 40, 74

[73] Yoshida, K., Yamasaki, J., and Tanaka, N. *Nanotechnology* **15**(6), S349–S354 June (2004). 40, 74

[74] Ohno, Y. and Takeda, S. *Review of Scientific Instruments* **66**(10), 4866 (1995). 40

[75] Zagonel, L. F., Mazzucco, S., Tencé, M., March, K., Bernard, R., Laslier, B., Jacopin, G., Tchernycheva, M., Rigutti, L., Julien, F. H., Songmuang, R., and Kociak, M. *Nano letters* **11**(2), 568–73 February (2011). 40, 102

[76] Mahan, J. R. *Radiation Heat Transfer: A Statistical Approach*. John Wiley & Sons, (2002). 49

[77] Gou, L. and Murphy, C. J. *Nano Letters* **3**(2), 231–234 February (2003). 55, 57

[78] Paracchino, A., Mathews, N., Hisatomi, T., Stefik, M., Tilley, S. D., and Grätzel, M. *Energy & Environmental Science* **5**(9), 8673 (2012). 56

[79] Vanysek, P. In *CRC Handbook of Chemistry and Physics*, 80–89. (1998). 56

[80] Bak, T., Nowotny, J., Rekas, M., and Sorrell, C. *International Journal of Hydrogen Energy* **27**(2002), 991–1022 (2002). 56

[81] Laursen, A. B., Kegnæ s, S. r., Dahl, S. r., and Chorkendorff, I. *Energy & Environmental Science* **5**(2), 5577 (2012). 56

[82] Xu, Y. and Schoonen, M. A. *American Mineralogist* **85**(3-4), 543–556 March (2000). 56, 64

[83] Nagasubramanian, G. *Journal of The Electrochemical Society* **128**(5), 1055 (1981). 57

[84] Fleisch, T. and Mains, G. *Applications of Surface Science* **10**(1), 51–62 (1982). 57

[85] Sharma, R. and Crozier, P. In *Handbook of Microscopy for Nanotechnology*, 531–565. (2005). 61

[86] Atzmon, Z., Sharma, R., Mayer, J., and Hong, S. *MRS Proceedings* **317** January (1993). 61

[87] Powell, C. J. and Jablonski, a. *Journal of Physical and Chemical Reference Data* **28**(1), 19 (1999). 61

[88] Cheng, S. and Egerton, R. *Micron* **24**(3), 251–256 (1993). 61

[89] Su, D., Wang, H., and Zeitler, E. *Ultramicroscopy* **59**(1-4), 181–190 July (1995). 61

[90] Leapman, R. D., Grunes, L. A., and Fejes, P. L. *Physical Review B* **26**(2), 614 July (1982). 63

[91] Laffont, L., Wu, M. Y., Chevallier, F., Poizot, P., Morcrette, M., and Tarascon, J. M. *Micron (Oxford, England : 1993)* **37**(5), 459–64 January (2006). 63

[92] Wagner, J. B., Hansen, P. L., Molenbroek, A. M., Topsø e, H., Clausen, B. S., and Helveg, S. *The Journal of Physical Chemistry B* **107**(31), 7753–7758 August (2003). 63

[93] Keast, V. J., Scott, a. J., Brydson, R., Williams, D. B., and Bruley, J. *Journal of microscopy* **203**(Pt 2), 135–75 August (2001). 63

[94] Dionigi, F., Vesborg, P. C. K., Pedersen, T., Hansen, O., Dahl, S. S. r., Xiong, A., Maeda, K., Domen, K., and Chorkendorff, I. *Energy & Environmental Science* **4**(8), 2937–2942 (2011). 66

[95] Maeda, K., Teramura, K., Lu, D., Takata, T., Saito, N., Inoue, Y., and Domen, K. *Nature* **440**(7082), 295 March (2006). 66

[96] Maeda, K., Sakamoto, N., Ikeda, T., Ohtsuka, H., Xiong, A., Lu, D., Kanehara, M., Teranishi, T., and Domen, K. *Chemistry (Weinheim an der Bergstrasse, Germany)* **16**(26), 7750–9 July (2010). 66, 69, 78

[97] Silva, A. M. T., Machado, B. F., Gomes, H. T., Figueiredo, J. L., Dražić, G., and Faria, J. L. *Journal of Nanoparticle Research* **12**(1), 121–133 February (2009). 66

[98] Vesborg, P. C. K. and Jaramillo, T. F. *RSC Advances* **2**(21), 7933 (2012). 69

[99] Jaramillo, T., Jø rgensen, K., and Bonde, J. *Science* **317**(July), 100–102 (2007). 69

[100] Jaramillo, T., Bonde, J., and Zhang, J. *The Journal of Physical Chemistry C* **112**, 17492–17498 (2008). 69

[101] Seger, B., Laursen, A. B., Vesborg, P. C. K., Pedersen, T., Hansen, O., Dahl, S. r., and Chorkendorff, I. *Angewandte Chemie (International ed. in English)* **51**(36), 9128–31 September (2012). 70

[102] Vesborg, P. C., Olsen, J. L., Henriksen, T. R., Chorkendorff, I., and Hansen, O. *Chemical Engineering Journal* **160**(2), 738–741 June (2010). 70

[103] Inoue, H., Wang, J., Sasaki, K., and Adzic, R. *Journal of Electroanalytical Chemistry* **554-555**, 77–85 September (2003). 71

[104] Inoue, Y. *Energy & Environmental Science* **2**(4), 364 (2009). 71

[105] Lin, G. H., Kapur, M., Kainthla, R. C., and Bockris, J. O. *Applied Physics Letters* **55**(4), 386 (1989). 71

[106] Foster, N. S., Lancaster, A. N., Noble, R. D., and Koval, C. a. *Industrial & Engineering Chemistry Research* **34**(11), 3865–3871 November (1995). 72

[107] Reddy, K. M. *Materials Chemistry and Physics* **78**, 239–245 (2003). 74

[108] Amtout, A. and Leonelli, R. *Physical Review B* **51**(11), 6842–6851 (1995). 74

[109] NREL. 74

[110] Paz, Y., Luo, Z., Rabenberg, L., and Heller, a. *Journal of Materials Research* **10**(11), 2842–2848 March (2011). 74

[111] Konta, R., Ishii, T., Kato, H., and Kudo, A. *The Journal of Physical Chemistry B* **108**(26), 8992–8995 July (2004). 77

[112] Domen, K., Naito, S., Soma, M., Onishi, T., and Tamaru, K. *Journal of the Chemical Society, Chemical Communications* (12), 543 (1980). 77

[113] Puangpetch, T., Sreethawong, T., Yoshikawa, S., and Chavadej, S. *Journal of Molecular Catalysis A: Chemical* **312**(1-2), 97–106 October (2009). 77

[114] Osterloh, F. E. *Chemistry of Materials* **20**(1), 35–54 January (2008). 77

REFERENCES

[115] Chen, H.-C., Huang, C.-W., Wu, J. C. S., and Lin, S.-T. *The Journal of Physical Chemistry C* **116**(14), 7897–7903 April (2012). 77

[116] Braunschweig, E., Logan, A., Datye, A., and Smith, D. *Journal of Catalysis* **237**, 227–237 (1989). 77, 82

[117] Huang, Y., Wang, a., Li, L., Wang, X., Su, D., and Zhang, T. *Journal of Catalysis* **255**(2), 144–152 April (2008). 77

[118] Maeda, K., Teramura, K., Lu, D., Saito, N., Inoue, Y., and Domen, K. *Journal of Physical Chemistry C* **111**(20), 7554–7560 May (2007). 77

[119] Bernal, S., Calvino, J., and Gatica, J. *Journal of Catalysis* **169**, 510–515 (1997). 78

[120] Bernal, S., Blanco, G., and Calvino, J. *V. Cortés Corberán and S. Vic Bellón, Editor(s), Studies in Surface Science and Catalysis* **82**, 507–514 (1994). 78

[121] Bernal, S., Calvino, J., Cauqui, M., Cifredo, G., Jobacho, A., and Rodrìguez-Izquierdo, J. *Applied Catalysis A: General* **99**, 1–8 (1993). 78

[122] Bernal, S., Botana, F., Calvino, J., Cifredo, G., Pérez-Omil, J., and Pintado, J. M. *Catalysis today* **23**, 219–250 (1995). 78

[123] Liu, J. *Microscopy and Microanalysis* **10**(1), 55–76 February (2004). 78, 79

[124] Bernal, S., Botana, F. J., Calvino, J. J., Lòpez, C., Pérez-Omil, J. A., and Rodrguez-Izquierdo, J. M. *Journal of the Chemical Society, Faraday Transactions* **92**, 2799–2809 (1996). 78, 79

[125] Bernal, S., Botana, F. J., Calvino, J. J., Lòpez-Cartes, C., Pérez-Omil, J. A., and Rodriguez-lzquierdo, J. M. *Ultramicroscopy* **72**, 135–164 (1998). 79

[126] Baker, R. *Journal of Catalysis* **79**(2), 348–358 February (1983). 81

[127] Okada, M., Jin, P., Yamada, Y., Tazawa, M., and Yoshimura, K. *Surface Science* **566-568**, 1030–1034 September (2004). 84, 85

[128] Bertoni, G., Beyers, E., Verbeeck, J., Mertens, M., Cool, P., Vansant, E., and Van Tendeloo, G. *Ultramicroscopy* **106**(7), 630–635 May (2006). 84

[129] Fischer, D. W. *Journal of Applied Physics* **41**(9), 3561 (1970). 85

[130] Rharbi, Y. *Physical Review E* **77**(3), 031806 March (2008). 88

[131] Larsson, E. M., Millet, J., Gustafsson, S., Skoglundh, M., Zhdanov, V. P., and Langhammer, C. *ACS Catalysis* **2**(2), 238–245 February (2012). 88

[132] Chan, G. H., Zhao, J., Hicks, E. M., Schatz, G. C., and Van Duyne, R. P. *Nano Letters* **7**(7), 1947–1952 July (2007). 88

[133] Hansen, P. L., Wagner, J. B., Helveg, S., Rostrupnielsen, J. R., Clausen, B. S., and Topsø e, H. *Science* **295**(March), 2053–2055 (2002). 89

[134] Lin, S. D., Bollinger, M., and Vannice, M. a. *Catalysis Letters* **17**(3-4), 245–262 September (1993). 89

[135] Crozier, P. a. and Chenna, S. *Ultramicroscopy* **111**(3), 177–85 February (2011). 100

[136] Howie, A. *Ultramicroscopy* **11**, 141–148 (1983). 100

[137] Gabor, D. *Nature* **161**(4098), 777–778 May (1948). 100

[138] Boyd, D. a., Greengard, L., Brongersma, M., El-Naggar, M. Y., and Goodwin, D. G. *Nano letters* **6**(11), 2592–7 November (2006). 100

[139] Kapitza, P. and Dirac, P. *Proceedings Of The Cambridge Philosophical Society* **29**, 297–300 (1933). 101

[140] Blackie, E. J., Le Ru, E. C., and Etchegoin, P. G. *Journal of the American Chemical Society* **131**(40), 14466–72 October (2009). 102